

Experiments on passive scalar mixing in turbulent flows with different velocity- and scalar-field boundary conditions

Jason LEPORE

Doctor of Philosophy

Department of Mechanical Engineering

McGill University

Montréal, Québec

August 2013

A thesis submitted to McGill University in partial fulfillment of the
requirements of the degree of Doctor of Philosophy.

©Jason Lepore, 2013.

DEDICATION

To my wife Tina, for her never-ending love, guidance and support, all of which has made this work possible.

*In theory there is no difference between
theory and practice. In practice there is.*

Yoggi Berra

ACKNOWLEDGEMENTS

First, I would like to extend my gratitude to Professor Laurent Mydlarski for his continued support throughout the course of my studies. He has been a role model, a mentor and a friend, and I am eternally grateful for his guidance and dedication over the last five years.

I am grateful to the Natural Sciences and Engineering Research Council of Canada for their financial support, both during my undergraduate and graduate studies at McGill. I am equally grateful to the Faculty of Engineering for their support by means of a McGill Engineering Doctoral Award.

I would like to thank George Tewfik, Mario Iacobaccio and Tony Micozzi for their superior technical assistance. I am grateful to my colleagues Arpi Berajeklian, Emmanuel Germaine and Babak Khorsandi for their assistance throughout my studies.

Finally, I would like to thank my wife Tina, my parents and my sister, along with all of my family and friends, for their love and support throughout this journey.

ABSTRACT

An experimental investigation of the influence of the large-scale features of turbulent flows on the mixing of a passive scalar (viz. temperature) therein is presented. Given the direct relationship between the large scales of turbulent flows and the geometrical configuration of the flow, two distinct sets of experiments are conducted in which the dependence of the scalar mixing on the (i) scalar- and (ii) velocity-field boundary conditions is studied. In this work, hot-wire anemometry and cold-wire thermometry are used to measure the fluctuating velocity and temperature fields, respectively.

The first set of experiments is conducted in the plane wake downstream of a circular cylinder. To vary the scalar-field boundary conditions, while maintaining a hydrodynamically identical flow field, two different heat injection mechanisms are employed. First, a heating element is embedded within the cylinder that generates the hydrodynamic wake. When the element is energized, the wake is therefore heated by means of a “heated cylinder.” Second, an array of fine, Nichrome wires is installed downstream of, and oriented parallel to, the cylinder. This configuration, known as a “mandoline,” has been demonstrated to have a negligible influence on the velocity field, due to the small diameter of the wires. Consequently, either configuration can be energized to heat the wake without altering the underlying velocity field. Using this apparatus, multiple velocity and passive-scalar statistics are examined. The measurements suggest that certain small-scale statistics (such as the inertial-convective-range scaling exponents of the passive scalar structure functions) may be contaminated by the large-scale features of the scalar field. Consequently, it is of interest to determine why such statistics

exhibit these dependencies. In particular, the passive scalar structure functions, and their inertial-convective-range scaling exponents, along with the mixed velocity-temperature structure functions and the (non-centered) autocorrelations of the dissipation rate of scalar variance are employed to obtain quantitative estimates of the internal intermittency of the passive scalar field. It is revealed that the high-order passive scalar structure function scaling exponents display a significant difference when comparing the results generated using different heat injection mechanisms. While this result suggests that the two passive scalar fields exhibit different levels of internal intermittency, the mixed structure functions and autocorrelations of the dissipation rate of scalar variance indicate that both temperature fields possess similar levels of intermittency. Upon examination of the kurtosis structure functions of the temperature difference (i.e. the high-order structure functions normalized using the second-order structure function), the present work suggests that passive scalar structure function scaling exponents exhibit a dependence on the scalar-field boundary conditions due to the finite (and different) Péclet numbers of the flows under consideration — an effect that is significantly less prominent in the measurements of the mixed velocity-temperature structure functions and the (non-centered) autocorrelations of the dissipation rate of scalar variance.

The second set of experiments consists of a study of the scalar field downstream of a concentrated line source within a fully-developed, high-aspect-ratio channel flow. However, unlike previous dispersion measurements employing concentrated sources, the current research employs a line source oriented in the direction of the inhomogeneity of the velocity field. Consequently, the resulting wake downstream of the line source is statistically three-dimensional. The dispersion is measured in planes parallel to the channel walls, and lateral dispersion data can therefore be obtained for a variety of wall-normal

distances. In such an arrangement, the velocity field at each wall-normal position is different, since the velocity field in the current configuration is solely a function of the wall-normal distance. The resultant mixing is studied using a variety of statistics, including the mean and root-mean-square temperature distributions, probability density functions of the temperature fluctuations, as well as the (turbulent) intensity of the scalar fluctuations. These results are contrasted with prior transverse dispersion measurements in which the scalar dispersion remains statistically two-dimensional, in an attempt to elucidate the effect of the velocity-field boundary conditions. The findings suggest that both the mean flow shear and turbulence intensity of the velocity field play an important role in determining the mixedness of the scalar field.

RÉSUMÉ

Une étude expérimentale de l'effet des caractéristiques à grandes-échelles des écoulements turbulents sur le mélange d'un scalaire passif (température) y est présentée. Étant donné la relation directe entre les grandes échelles des écoulements turbulents et la configuration géométrique de l'écoulement, deux ensembles d'expériences distincts sont menés dans lesquels la dépendance du mélange d'un scalaire sur les conditions limites du (i) champ scalaire et (ii) champ de vitesse est étudiée. Dans ce mémoire, l'anémométrie à fil chaud et la thermométrie à fil froid sont utilisées pour mesurer le champ de vitesse et le champ scalaire, respectivement.

Le premier ensemble d'expériences est réalisé dans le sillage d'un cylindre circulaire. Pour varier les conditions limites du champ scalaire, tout en gardant le même écoulement hydrodynamique, deux mécanismes d'injection de chaleur différents sont utilisés. Premièrement, un élément chauffant est incorporé dans le cylindre qui génère le sillage hydrodynamique. Lorsque l'élément est mis sous tension, le sillage est donc chauffé au moyen d'un "cylindre chauffé". Deuxièmement, un ensemble de fils fins est installé en aval du, et orienté parallèlement au, cylindre. Cette configuration, connue sous le nom de "mandoline," s'est avérée d'avoir une influence négligeable sur le champ de vitesse, en raison du faible diamètre des fils. Par conséquent, l'une des deux configurations peut être utilisée pour chauffer le sillage, sans modifier le champ de vitesse, et de nombreuses statistiques du champ scalaire et du champ de vitesse sont examinées. Les mesures suggèrent que certaines statistiques à petites-échelles (comme les exposants d'échelle de la zone inertielle-convective des fonctions de structure du champ scalaire) peuvent être contaminées par les caractéristiques à grandes-échelles du champ scalaire. Par conséquent, il est

intéressant de déterminer la raison pour laquelle ces statistiques présentent de telles dépendances. En particulier, les fonctions de structure du champ scalaire (et leurs exposants d'échelle), ainsi que les fonctions de structure mixte vitesse-température et les autocorrélations (non-centrées) du taux de dissipation de la variance scalaire, sont utilisées pour obtenir des estimations quantitatives de l'intermittence interne du champ scalaire. Il est conclu que les exposants d'échelle des fonctions de structure du champ scalaire passif présentent une différence importante lorsque l'on compare les résultats obtenus en utilisant de différents mécanismes d'injection de chaleur. Bien que ce résultat suggère que les deux champs scalaires passifs aient de différents niveaux d'intermittence, les fonctions de structure mixte et les autocorrélations du taux de dissipation de la variance scalaire indiquent que les deux champs de température possèdent des niveaux d'intermittence similaires. Lorsque l'on examine les fonctions de structure du coefficient d'aplatissement (les fonctions de structure d'ordre quatre normalisées par la fonction de structure de deuxième ordre) de la différence de température, ce mémoire suggère que les exposants d'échelle des fonctions de structure démontrent une dépendance aux conditions limites du champ scalaire en raison des nombres de Péclet finis (et différents) des écoulements étudiés — un effet qui est nettement moins important dans les fonctions de structure mixte vitesse-température et les autocorrélations (non centrées) du taux de dissipation de la variance scalaire.

Le deuxième ensemble d'expériences consiste d'une étude du champ scalaire en aval d'une source concentrée linéaire dans un écoulement de canal pleinement développé, ayant un rapport hauteur-largeur élevé. Contrairement à des mesures de dispersion précédentes utilisant des sources concentrées, ce travail emploie une source linéaire orientée dans la direction de l'inhomogénéité du champ de vitesse. Par conséquent, le panache thermique créé par la source

linéaire est (statistiquement) tridimensionnel. La dispersion est mesurée dans des plans parallèles aux parois du canal, et des données de dispersion latérale peuvent donc être obtenues pour de différentes distances perpendiculaires au mur. Dans une telle configuration, le champ de vitesse à chaque distance du mur est différent, puisque le champ de vitesse dans la configuration actuelle est uniquement une fonction de la distance du mur. Le mélange du scalaire passif est étudié en utilisant une variété de statistiques, incluant la moyenne et la moyenne quadratique du champ de température, des fonctions de densité de probabilité des fluctuations de température, ainsi que l'intensité (turbulent) des fluctuations scalaires. Ces résultats (i) exposent les différences entre ces mesures et celles de dispersion transverse, dans lesquelles la dispersion du scalaire reste statistiquement bidimensionnel, et (ii) facilitent l'élucidation des effets des conditions limites du champ de vitesse sur le mélange d'un scalaire passif. Les résultats suggèrent que le cisaillement de l'écoulement moyen et l'intensité turbulent du champ de vitesse jouent un rôle important dans la détermination du niveau de mélange du champ scalaire.

TABLE OF CONTENTS

DEDICATION	iii
ACKNOWLEDGEMENTS	v
ABSTRACT	vii
RÉSUMÉ	xi
LIST OF TABLES	xvii
LIST OF FIGURES	xix
1	Introduction	1
	1.1 Motivation and Objectives	1
	1.2 Literature Review	8
	1.2.1 Kolmogorov Theory of Turbulence	9
	1.2.2 Velocity and Passive-Scalar Structure Functions	17
	1.2.3 Dispersion from Concentrated Sources	27
	1.3 Structure of Thesis	32
2	Experimental Apparatus	35
	2.1 Wind Tunnel Facility	35
	2.2 Channel Flow Facility	39
	2.3 Instrumentation	44
	2.3.1 Hot-Wire Anemometry	44
	2.3.2 Cold-Wire Thermometry	47
	2.4 Data Acquisition	50
3	Experimental Conditions and Flow Validation	53
	3.1 Internal Intermittency Measurements	53
	3.2 Lateral Dispersion Measurements	59
4	Results	67
	4.1 Internal Intermittency Measurements	67
	4.1.1 Measures of Internal Intermittency	69
	4.1.2 Finite-Péclet-Number Effects	81
	4.1.3 Compensation of Kurtosis Structure Functions	89
	4.2 Lateral Dispersion Measurements	92

4.2.1	The mean temperature field	95
4.2.2	The fluctuating temperature field	108
4.2.3	Temperature PDFs	127
5	Conclusions	133
5.1	Internal Intermittency Experiment	133
5.2	Lateral Dispersion Experiment	137
5.3	Contributions of the Present Study	141
5.4	Extensions of the Present Work	144
A	Error and Uncertainty Analysis	147
A.1	Uncertainty of the Temperature Measurements	148
A.2	Uncertainty of the Velocity Measurements	151
A.3	Uncertainty of the Turbulent Statistics	153
A.4	Probe Spatial and Temporal Resolution Errors	155

LIST OF TABLES

<u>Table</u>	<u>page</u>
4.1 Flow parameters for the internal intermittency experiment.	68
4.2 Inertial-range scaling exponents of the structure functions of the velocity and passive scalar fields.	75
4.3 Flow parameters for the lateral dispersion experiment.	94
4.4 Parameters corresponding to the power law evolution of the normalized peaks and half-widths of the mean temperature excess profiles.	101
4.5 Parameters corresponding to the power law evolution of the normalized centreline values and half-widths of the root- mean-square temperature profiles.	115
4.6 Comparison of previous and present flows in which scalar dispersion from a concentrated source has been studied.	117
A.1 Summary of the various sources of error for the absolute tem- perature measurements.	150
A.2 Summary of the various sources of error for the absolute velocity measurements.	152

LIST OF FIGURES

<u>Figure</u>	<u>page</u>
1.1 The inertial(-convective) range scaling exponents of the velocity and passive scalar fields, obtained from the published literature.	25
2.1 Schematic illustrating the experimental configuration of the internal intermittency experiment.	37
2.2 Picture of the open-circuit wind tunnel test section with the current experimental apparatus installed.	38
2.3 Schematic illustrating the transverse and lateral dispersion problems studied in Lavertu & Mydlarski (2005) and the current work.	41
2.4 Picture of the modified channel test section with a sliding access port for the hot- and cold-wire sensors.	42
2.5 Typical calibration curves for a hot-wire sensor at different free-stream temperatures.	46
2.6 Typical calibration curves for a cold-wire sensor.	48
3.1 Comparison of the PDFs of the velocity fluctuation, sixth-order velocity structure functions and power spectra of the velocity fluctuations for both the unheated and heated wakes (for both scalar field boundary conditions).	54
3.2 Comparison of the PDFs of the velocity fluctuation, sixth-order velocity structure functions and power spectra of the velocity fluctuations for the different scalar field boundary conditions.	57
3.3 Comparison of the power spectrum of the temperature fluctuations and PDFs of the temperature fluctuation computed from the heated cylinder and mandoline experiments.	60
3.4 Probability density functions for the temperature increment, multiplied by the increment raised to the eighth power.	61
3.5 Transverse profiles of the longitudinal velocity at three different spanwise positions.	63
3.6 One-dimensional longitudinal spectra of the velocity fluctuations at two wall-normal elevations.	64

4.1	The n^{th} -order structure functions of the temperature increment, normalized using Kolmogorov variables.	70
4.2	The second- and mixed third-order structure functions of the temperature fluctuation, subject to varying scalar-field boundary conditions.	72
4.3	The mixed, sixth-order structure function plotted as a function of the non-dimensional separation, obtained using the different scalar-field boundary conditions.	78
4.4	The non-centered autocorrelation of the dissipation rate of scalar variance plotted as a function of the non-dimensional separation, obtained using the different scalar-field boundary conditions.	79
4.5	The high-order moments of the passive scalar increments plotted as a function of the separation.	83
4.6	The kurtosis structure functions plotted as a function of the Péclet-number-compensated separation.	86
4.7	The mixed (velocity-temperature) “super-kurtosis” (sixth-order) structure function, plotted as a function of the separation, for the scalar fields generated by the heated cylinder and mandoline.	88
4.8	The offset and normalized kurtosis structure functions of the passive scalar increment plotted as a function of the separation.	90
4.9	Downstream evolution of the lateral profiles of the mean temperature excess, non-dimensionalized by their peak value, for six wall-normal distances.	96
4.10	Transverse evolution of the lateral profiles of the mean temperature excess, non-dimensionalized by their peak value, for six downstream positions.	97
4.11	The downstream and transverse evolution of the centreline mean temperature excess non-dimensionalized using the reference temperature rise.	100
4.12	The downstream and transverse evolution of the half-width of the mean temperature excess profiles non-dimensionalized using the channel half-width.	104
4.13	The downstream evolution of the centreline value and half-width of the mean temperature excess profiles, using a Lagrangian non-dimensionalization.	107

4.14	Downstream evolution of the lateral profiles of the non-dimensionalized root-mean-square temperature for six wall-normal elevations.	110
4.15	Transverse evolution of the lateral profiles of the non-dimensionalized root-mean-square temperature for six downstream positions.	111
4.16	The downstream and transverse evolution of the centreline root-mean-square temperature fluctuation non-dimensionalized using the reference temperature rise.	114
4.17	The downstream and transverse evolution of the half-width of the root-mean-square temperature profiles non-dimensionalized using the channel half-width.	119
4.18	The downstream evolution of the centreline value and half-width of the root-mean-square temperature profiles, using a Lagrangian non-dimensionalization.	121
4.19	The downstream development of the ratio of the centreline root-mean-square temperature fluctuation to the peak (i.e. centreline) mean temperature excess for six different wall-normal positions.	123
4.20	Comparison of the one-dimensional spectra of the temperature fluctuations measured herein to those obtained by Lavertu & Mydlarski (2005), non-dimensionalized using Kolmogorov variables.	126
4.21	Non-dimensionalized probability density functions of the temperature fluctuations at different downstream positions for the six wall-normal elevations.	128
4.22	Comparison of the non-dimensional probability density functions measured herein with those obtained in Lavertu & Mydlarski (2005) for three of the downstream positions.	131

CHAPTER 1

Introduction

1.1 Motivation and Objectives

In engineering practice, as well as the study of geophysical phenomena, fluid flow is often encountered. Its analysis is essential to the prediction of many engineering phenomena (e.g. the flow of air around an airfoil; the pumping of oil through a pipeline) and environmental applications (e.g. weather forecasting; dispersion of a pollutant in the atmosphere). However, fluid flow is governed by non-linear, coupled, partial differential equations. Consequently, analytical solutions to most practical fluid flow problems are limited to a selection of simplified, special cases.

Fluid flows are broadly designated as either “laminar” or “turbulent.” Laminar flows are those in which the bulk motion of the fluid is structured in “laminae” or layers. Consequently, there is (relatively) little exchange of fluid particles between adjacent fluid layers, because transfers of mass, momentum and energy occur by molecular interactions/diffusion. On the other hand, the vast majority of both engineering and naturally-occurring flows are turbulent.

Given that it is difficult to formulate a precise definition of turbulence, a common approach is to list its characteristics. Tennekes & Lumley (1972) define turbulent flows as those possessing the properties that follow. First and foremost, turbulence is chaotic, and, unlike structured laminar flows, turbulent flows exhibit irregular, three-dimensional fluctuations in both their velocity and vorticity fields. Moreover, turbulent flows are organized as a multitude of “eddies” (i.e. coherent, rotational structures) of varying sizes. Due to these

characteristics, turbulent flow problems are generally analytically intractable. One common approach to their analysis relies on statistical methods.

Given the above-described nature of turbulent flows, they readily mix mass, momentum and energy, due to advection by their three-dimensional, fluctuating velocity fields. The enhanced mixing that occurs within turbulent flows is one of its most striking features. One can readily identify numerous phenomena in the fields of combustion, meteorology, heat transfer, oceanic science and environmental pollutant dispersion that rely on this said property.

Since turbulent flows arise due to instabilities in laminar flows, turbulence is found to occur at large Reynolds numbers, i.e. $Re_L = UL/\nu$, where U and L are characteristic velocity and length scales, respectively, of the flow, and ν is the kinematic viscosity of the fluid. The Reynolds number is frequently interpreted as the ratio of the non-linear inertial (or advection) term in the governing equations to the viscous (diffusion) term. Therefore, a large-Reynolds-number flow is one in which the viscosity of the fluid is unable to damp out the instabilities that arise from the inertial term. These flow instabilities grow and coalesce, and are responsible for the transition to turbulent flow.

Finally, turbulent flows are highly dissipative in nature. They readily extract energy from the mean flow that is eventually converted into internal energy by molecular (i.e. viscous) interactions. Turbulence therefore requires a continuous source of energy to be sustained.

Given the ubiquitous nature of turbulent flows, an understanding of turbulence, and the mixing that occurs therein, is crucial to multiple disciplines. However, as stated above, many, if not most, practical turbulent flow problems remain unsolved. A principal difficulty associated with the analysis of these problems lies predominantly in the treatment of the continuum of eddies of

different sizes that characterize turbulence. Consequently, this feature of turbulent flows has been the subject of extensive study by numerous investigators.

The largest of these eddies scale with the geometry of the flow and, as such, are usually anisotropic (and always flow-dependent). Their characteristic size, commonly referred to as the “integral length scale,” is denoted by ℓ . At large Reynolds numbers, the action of viscosity is negligible on these large eddies that engender smaller eddies in a process known as the “turbulent cascade.” Such a process generates smaller and smaller eddies, until the effect of viscosity dominates over the inertial effects. In this limit, a “local Reynolds number,” defined using scales characteristic of the size and velocity of the smallest eddies, approaches unity. One can also define a length scale representative of these smallest (dissipative) eddies in the flow: the Kolmogorov microscale of length (typically denoted by η). Its magnitude depends on the kinematic viscosity of the fluid (ν) and the dissipation rate of turbulent kinetic energy per unit mass (ϵ), where:

$$\epsilon \equiv 2\nu \langle s_{ij}s_{ij} \rangle \equiv \frac{\nu}{2} \left\langle \left(\frac{\partial u_i}{\partial x_j} + \frac{\partial u_j}{\partial x_i} \right) \left(\frac{\partial u_i}{\partial x_j} + \frac{\partial u_j}{\partial x_i} \right) \right\rangle,$$

and the angular brackets denote averaging. The Kolmogorov microscale is then defined as:

$$\eta \equiv \left(\frac{\nu^3}{\epsilon} \right)^{1/4}.$$

The elucidation of the turbulent cascade has proven to be an important discovery in the study of turbulence. It not only underlies the predominant theory of turbulence — put forth in the seminal works of Kolmogorov (Kolmogorov, 1941*a,b,c*) — but it also bolstered the study of a second, significant problem — the mixing of scalar contaminants within turbulent flows, which is relevant to a multitude of both environmental and engineering processes.

A scalar field can be considered “passive” if its presence in the flow does not alter the advecting velocity field. (This is a more fundamental case than that of “active” scalars, which modify the underlying velocity field.) One common example is temperature (denoted herein using θ), which can be considered passive provided the density changes associated with the temperature differences are small enough so as not to induce buoyancy effects. In recent years, there have been significant advances in the understanding of passive scalar mixing within turbulent flows. Most notably, it has been concluded that certain aspects of the scaling and structure of a turbulent passive scalar field arise from the mixing process itself, rather than from the nature of the velocity field that performs the mixing (Shraiman & Siggia, 2000; Warhaft, 2000). Consequently, the study of turbulent passive scalars, once considered “a footnote to the turbulence problem” (Warhaft, 2000), has evolved into a field of study in its own right.

Analogously with hydrodynamic turbulence, passive scalar turbulence also exhibits a turbulent cascade. Once again, the largest scalar eddies scale with the geometry of the flow — their characteristic length scale is known as the “scalar integral length scale” and is commonly denoted by ℓ_θ . There also exists an analogous length scale for the smallest scalar eddies within the flows (η_θ), which characterize the eddies responsible for smearing out the fluctuations in the scalar field by molecular (diffusive) processes. For fluids with a Schmidt number (or, in the case of the temperature field, Prandtl number) much larger than 1 (i.e. $Sc \gg 1$, where $Sc \equiv \nu/\alpha$ and α is the scalar diffusivity), the smallest scalar eddies are smaller than the Kolomogorov microscale, and are therefore exposed to the entire range of hydrodynamic eddies, thus yielding the following expression for the “Batchelor microscale of length” or “Batchelor scale:”

$$\eta_\theta \equiv \left(\frac{\nu\alpha^2}{\epsilon} \right)^{1/4} \equiv \eta Sc^{1/2}, \quad Sc \gg 1.$$

For fluids with a Schmidt number that is much less than 1 ($Sc \ll 1$), the smallest scalar eddies are larger than the Kolmogorov microscale. The ‘‘Corrsin microscale’’ is defined as:

$$\eta_\theta \equiv \left(\frac{\alpha^3}{\epsilon} \right)^{1/4} \equiv \eta Sc^{-3/4}, \quad Sc \ll 1.$$

(In the limit of $Sc \rightarrow 1$, both the Batchelor and Corrsin scales asymptote to the Kolmogorov scale, η).

The phenomenology of both the hydrodynamic and passive scalar cascade has received significant consideration from numerous investigators — see, for example, the review papers by Sreenivasan (1991) or Sreenivasan & Antonia (1997). More precisely, many researchers examined the interactions that occur among the eddies of varying sizes to elucidate the structure of the turbulent cascade. While some recent studies suggest that the turbulence cascade may not be a continuous process — see, for example, Villermaux *et al.* (2001) — the evidence presented in the literature clearly establishes the relationship between both the large- and small-scale flow structures. The mixing process relies on both the large- and small-scale features of a turbulent flow. While the former is responsible for the entrainment and initial mixing of the scalar contaminant, the latter smoothes out the resultant scalar field.

The objective of the present work is to examine the influence of boundary conditions on the scalar mixing that occurs within turbulent flows. This is accomplished by examining the relationship between the large- and small-scale

features of a turbulent flow and the resultant mixing. Herein, two particular cases will be studied.

Firstly, the effect of the scalar-field boundary conditions on the intermediate- and small-scale structure of a turbulent passive scalar field will be examined. It has been well-documented in the literature that the dynamics of the small-scale structures are vastly different from the large-scale flow features (see, for example, Sreenivasan (1991), Sreenivasan & Antonia (1997), Shraiman & Siggia (2000) and Warhaft (2000)). While the large-scale structure of a turbulent flow often exhibits quasi-Gaussian behaviour, the small-scale statistics deviate significantly from Gaussianity. This observation of scale-dependent statistics is inconsistent with the postulate of local isotropy put forth by Kolmogorov, since the latter requires that the probability density functions of the small-scale statistics be universal functions of the dissipation rate of turbulent kinetic energy and the kinematic viscosity of the fluid. As outlined above, it is hypothesized that the large-scale flow may bypass the cascade entirely and interact directly with the smallest eddies within a turbulent flow. For example, the skewness of the passive scalar derivative:

$$S_{\partial\theta/\partial x} = \frac{\langle(\partial\theta/\partial x)^3\rangle}{\langle(\partial\theta/\partial x)^2\rangle^{3/2}},$$

typically has the same sign as the mean scalar gradient, $\partial\langle T\rangle/\partial x$, due to this phenomena (Freymuth, 1976; Sreenivasan & Antonia, 1977). Therefore, it is not unreasonable to assume that the large-scale flow features may influence the small-scale statistics through these interactions. Moreover, these interactions will no doubt influence the mixing that occurs within turbulent flows as well. Consequently, a thorough understanding of the mixing that arises due to these interactions is critical to our understanding of turbulent flows. To this end, one objective of the current research is to determine whether variations in

the boundary conditions (i.e. the large-scale flow features) can alter the small-scale structure of the scalar field (and hence be responsible for the observed behaviour of such quantities). This is accomplished by examining a variety of statistics in a flow that remains hydrodynamically unchanged, albeit with different scalar injection mechanisms. Thus, any observed differences in the small-scale structure arise solely due to the scalar-field boundary conditions.

Secondly, the effect of the boundary conditions of the underlying velocity field on the mixing of a passive scalar emitted from a concentrated line source will be studied. (In this context, a “concentrated source” is defined as one that injects a scalar into a turbulent flow at a length scale much smaller than that which characterizes the velocity field.) This problem is relevant to many environmental and industrial applications in which scalars are released at small scales into flows that have varying degrees of inhomogeneity in different directions. Consider, for example, the downstream dispersion of the plume emitted from a smokestack. The pollutant concentration is injected into the turbulent atmospheric boundary layer, where it is mixed with the ambient air. As the plume is transported downstream, it grows not only in the vertical direction, but horizontally as well. Given that atmospheric turbulence is neither homogeneous nor isotropic, there is no *a priori* reason to expect the vertical and horizontal evolutions of the plume to be the same. For example, the Pasquill–Gifford curves (Gifford, 1961; Pasquill, 1961) provide estimates of the evolution of the mean plume widths in both the vertical and horizontal directions (subject to different atmospheric stability conditions). Furthermore, changing the height of the smokestack, in this example, will also have differing effects on the vertical and horizontal dispersion. In this (realistic) case, the boundary conditions of the underlying velocity field play a crucial role in the mixing of passive contaminants within turbulent flows. Moreover, given the inhomogeneity of

practical fluid flows, passive scalar mixing is a statistically three-dimensional problem. Nevertheless, the majority of the research to date on the subject of scalar dispersion from concentrated sources has focussed on two-dimensional (i.e. transverse dispersion) problems within homogeneous flows — see, for example, Warhaft (1984), Nakamura *et al.* (1986), Sakai *et al.* (1986) and Karnik & Tavoularis (1989). Consequently, it is crucial to understand the mixing that occurs in both the transverse and lateral directions to obtain a complete picture of the mixing phenomenon. To this end, experiments are performed in which the lateral dispersion of the passive scalar field is analyzed and compared to similar problems pertaining to the transverse dispersion to identify the influence of the different velocity-field boundary conditions.

1.2 Literature Review

The following section is divided into three sub-sections. Section 1.2.1 examines some of the implications of the predominant theory of turbulence, i.e. the seminal works of Kolmogorov (Kolmogorov, 1941*a,b,c*) (abbreviated herein as “K41”). Next, the literature pertaining to the two sets of experiments presented herein is discussed. The influence of the passive scalar boundary conditions is examined by means of the structure functions (and their respective, inertial-range scaling exponents), whereas the effect of the velocity field boundary conditions is studied by a comparison of the lateral and transverse dispersion downstream of a concentrated line source. Consequently, section 1.2.2 summarizes the literature pertaining to the (velocity and) passive scalar structure functions obtained from a variety of laboratory experiments, numerical simulations and atmospheric measurements, whereas a review of the various (lateral and transverse) dispersion experiments described in the literature is presented in section 1.2.3. For a general introduction to turbulent flows, and the passive scalar mixing that occurs therein, the reader is referred

to the books by Monin & Yaglom (1971), Tennekes & Lumley (1972), Frisch (1995) and Pope (2000), as well as the review articles of Sreenivasan (1991), Sreenivasan & Antonia (1997), Shraiman & Siggia (2000), Warhaft (2000) and Dimotakis (2005).

1.2.1 Kolmogorov Theory of Turbulence

The notion of the turbulent cascade was first put forth by Richardson (1922), who recognized that the structure of turbulence consisted of a large number of eddies of varying sizes. Building upon Richardson’s idea, Kolmogorov (1941*b*) proposed that the smallest eddies within turbulent flows are many orders of magnitude smaller than the largest eddies because energetic (i.e. high-Reynolds-number) flows can sustain many steps in the turbulent cascade. Using scaling arguments, it can be shown that:

$$\frac{\ell}{\eta} \sim Re_\ell^{3/4},$$

where Re_ℓ is a turbulent Reynolds number ($Re_\ell \equiv u'\ell/\nu$, where u' is the root-mean-square velocity fluctuation). Provided the separation of scales is large enough (i.e. $\ell \gg \eta$), one can argue that the small eddies, having undergone many steps in the cascade, will have lost all “recollection” of the large-scale features of the flow. In this instance, it seems plausible that the small eddies could be homogeneous, isotropic and independent of the large scales. This notion, called “local isotropy,” forms the basis of Kolmogorov theory. Kolmogorov further supposed that the smallest scales of the velocity field should be universal functions of the kinematic viscosity of the fluid (ν) and the dissipation rate of turbulent kinetic energy (ϵ). Moreover, if the separation of scales is large enough to define an intermediate range of scales (r) such that $\ell \gg r \gg \eta$, the set of scales r may be independent of both the geometry of the flow as well as the fluid viscosity (and solely determined by the dynamics

of the turbulence). Kolmogorov referred to this intermediate range of scales as the “inertial subrange,” which is characterized by universal statistics that are solely dependent on ϵ .

The practical considerations listed in the introduction also prompted many investigators to study turbulent passive scalar fields. Consequently, Kolmogorov’s postulate of local isotropy was extended to passive scalars by Oboukhov (1949) and Corrsin (1951), independently. (The theory is commonly referred to as the Kolmogorov-Oboukhov-Corrsin theory, abbreviated herein as “KOC.”) KOC theory states that, in the limit of infinite Reynolds and Péclet numbers ($Pe_{\ell_\theta} \equiv u'\ell_\theta/\alpha$), the separation between the large, integral scales (ℓ , and its passive scalar analogue, ℓ_θ) and the small, viscous and diffusive scales (the Kolmogorov and Batchelor/Corrsin microscales, η and η_θ , respectively) results in small-scale passive scalar statistics that are independent of the large-scale features of the flow. Given an intermediate range of scales, r , such that $\ell, \ell_\theta \gg r \gg \eta, \eta_\theta$, the set of scales r would be solely a universal function of the dissipation rate of turbulent kinetic energy (ϵ) and its passive scalar analogue, the dissipation rate of scalar variance, χ :

$$\chi \equiv \alpha \left\langle \frac{\partial \theta}{\partial x_j} \frac{\partial \theta}{\partial x_j} \right\rangle.$$

In analogy with its hydrodynamic counterpart, this range of scales is commonly referred to as the “inertial-convective subrange.”

Perhaps the most well-known consequence of Kolmogorov theory is the predicted inertial-range scaling of the power spectrum of turbulent kinetic energy, $E(\kappa)$. For such a range of scales, the statistics are independent of both the large-scale flow geometry and the fluid viscosity, and solely dependent on the dissipation rate of turbulent kinetic energy. Dimensional analysis dictates

that:

$$E(\kappa) = C\epsilon^{2/3}\kappa^{-5/3},$$

where κ is the magnitude of the wavenumber vector and C is a universal constant. The above-mentioned result can also be extended to the power spectrum of scalar variance, $E_\theta(\kappa)$, using similar dimensional arguments:

$$E_\theta(\kappa) = C_\theta\epsilon^{-1/3}\chi\kappa^{-5/3},$$

where C_θ is a second universal constant. Consequently, attempts to validate Kolmogorov theory focused on determining the inertial-range scaling of the turbulent kinetic energy and scalar variance spectra in the hopes of revealing a $-5/3$ scaling region. Early experimental results, in atmospheric, oceanic and wind tunnel flows, revealed the presence of the Kolmogorov scaling, thus providing the first validations of Kolmogorov theory (Laufer, 1952; Grant *et al.*, 1962; Gibson, 1963; Kistler & Vrebalovich, 1966).

In the years since 1941, Kolmogorov theory has been shown to be generally valid. In particular, low-order statistics (e.g. the turbulent kinetic energy and scalar variance spectra) agree well with Kolmogorov theory — a fact of notable significance given that their form was put forth from purely theoretical arguments without any *a priori* supporting evidence. Nevertheless, the theory has its limitations, which will now be addressed.

Shortcomings of K41/KOC theory have been reported in the literature. A prediction stemming from KOC theory is that the skewness of the passive scalar derivative:

$$S_{\partial\theta/\partial x} = \frac{\langle(\partial\theta/\partial x)^3\rangle}{\langle(\partial\theta/\partial x)^2\rangle^{3/2}},$$

must be zero, to satisfy the hypothesis of local isotropy. However, numerous investigators (Thoroddsen & Van Atta, 1992; Holzer & Siggia, 1994; Tong &

Warhaft, 1994; Mydlarski & Warhaft, 1998) have determined that the derivative skewness is in fact on the order of one in a variety of laboratory, numerical and atmospheric flows. Moreover, this violation of small-scale anisotropy persists in high-Reynolds- and high-Péclet-number flows. In addition, this result is also observed in numerical simulations using a Gaussian velocity field (Holzer & Siggia, 1994). Warhaft (2000) concludes that “only a multiplicity of scales, acting against an imposed mean temperature gradient, is all that is required to obtain the persistent anisotropy.” The observed violation of small-scale anisotropy is a result of “ramp-cliff” structures present within the flow, which form at the intersection of two, large-scale, counter-rotating velocity structures. This large-scale interaction creates a converging and diverging separatrix, which, in turn, leads to the creation of a scalar “front” (or “cliff”) structure at the diverging separatrix, due to entrainment of hot and cold fluid by the large, counter-rotating eddies (Antonia *et al.*, 1986).

Another noteworthy example of the shortcomings of Kolmogorov theory is the anomalous scaling of high-order structure functions in the inertial subrange. Using longitudinal velocity fluctuations (u) as an example, the n^{th} -order (longitudinal) structure function is defined as:

$$\langle (\Delta_r u)^n \rangle = \langle [u(x+r) - u(x)]^n \rangle,$$

where r is a (longitudinal) spatial separation. (Note that the second-order structure function (i.e. $n = 2$) is a real-space statistic that is directly related to turbulent kinetic energy spectrum.) At high Reynolds numbers, structure functions exhibit a power-law scaling of the type $\langle (\Delta_r u)^n \rangle \sim r^{\zeta_n}$ in the inertial subrange. According to K41 theory, the scaling exponents of the velocity structure functions (ζ_n) should equal $n/3$. However, the scaling exponents observed in the literature deviate from the predicted value of $n/3$, with the

magnitude of the difference increasing with structure function order. Such anomalous scaling is also observed in the study of turbulent passive scalar structure functions. Moreover, the passive scalar exponents (ξ_n) deviate even further from the $n/3$ prediction than do the velocity exponents.

The observed departures from K41/KOC theory stem from a phenomenon known as “internal intermittency.” The latter is characterized by intense fluctuations in the dissipation rates of turbulent kinetic energy (ϵ) and scalar variance (χ), which are not accounted for in K41/KOC theory. Furthermore, these events occur with greater frequency and intensity in the scalar field, as compared to the velocity field. The underlying causes of the stronger intermittency in the passive scalar field remains a topic of active research. As with passive scalar anisotropy, an important discovery is the realization that the intermittency of passive scalars can arise in a non-intermittent velocity field (Holzer & Siggia, 1994; Kraichnan, 1994). This “decoupling” of the passive scalar and velocity fields seems to suggest that the intermittency of passive scalars is a result of the mixing process, and not a reflection of the intermittency in the velocity field (Warhaft, 2000).

Despite the shortcomings of K41/KOC theory, the issue of small-scale universality remains unclear. In complex phenomena such as turbulence, universality is desirable as it simplifies the analysis and prediction of the phenomenon. Returning to the example of structure functions, many investigators continue to study the inertial-range scaling exponents of (velocity and passive scalar) structure functions in the hopes that the exponents are in fact universal, despite their deviations from K41/KOC theory.

To account for the effect of internal intermittency, Kolmogorov (1962) developed a refinement to his original similarity hypotheses. (This later theory is

commonly known as the “refined similarity hypothesis” and frequently abbreviated as “K62.”) The motivation for such a refinement stems from an objection put forth by Landau (see, for example Landau & Lifshitz, 1987), who noted that the dissipation rate of turbulent kinetic energy should increase without bound as the separation of scales (i.e. ℓ/r) increases. To resolve this situation, Kolmogorov (1962) proposed that the variance of the volume-averaged dissipation rate of turbulent kinetic energy¹ (denoted herein using ϵ_r) obeys a log-normal distribution, such that:

$$\sigma_{\ln \epsilon_r} = A + \mu \ln(\ell/r),$$

where A is a flow-dependent parameter and μ is a universal coefficient called the “intermittency exponent.” Consequently, the proper expression for the scaling of the velocity structure functions in the inertial range becomes:

$$\langle (\Delta u)^n \rangle = C_n r^{n/3} \langle \epsilon_r^{n/3} \rangle.$$

While the expression above may seem similar to the result derived using K41 theory, note that the use of the volume-averaged dissipation complicates the analysis. More precisely, one must take into account the fact that the volume-averaged dissipation is log-normally distributed. Consequently, the above expression becomes:

$$\langle (\Delta u)^n \rangle = C_n (r\epsilon)^{n/3} (\ell/r)^{\mu n(n-3)/18},$$

¹ Oboukhov (1962) first proposed to average the dissipation rate of turbulent kinetic energy over a sphere of radius r (where r is an inertial-range separation) since such an average takes into account the local fluctuations of the dissipation rate of turbulent kinetic energy, thereby providing a “pure ensemble average.”

where C_n is no longer a universal constant (as it was using K41 theory) but a flow-dependent parameter. Alternately stated, the inertial-range scaling of the velocity structure functions becomes:

$$\zeta_n = \frac{n}{3} - \frac{\mu n}{18} (n - 3),$$

where μ is the same intermittency exponent defined above.

Analogous refinements to the Kolmogorov-Oboukhov-Corrsin theory for the passive scalar field were put forth by Korchashkin (1970) and Van Atta (1971). More precisely, Van Atta (1971) proposed that, for a fluid with a Schmidt number of the order one, in analogy with the volume-averaged dissipation rate of turbulent kinetic energy, the volume-averaged dissipation rate of scalar variance, χ_r , also exhibits a log-normal distribution:

$$\sigma_{\ln \chi_r} = A_\theta + \mu_\theta \ln(\ell/r).$$

Once again, A_θ is a flow-dependent parameter and μ_θ is the intermittency exponent of the passive scalar field. Consequently, the analogous expression for the inertial-convective range scaling of the passive scalar structure functions becomes:

$$\langle (\Delta\theta)^n \rangle = K_n r^{n/3} \langle \chi_r^{n/2} \epsilon_r^{-n/6} \rangle.$$

Once again, K_n is a flow-dependent parameter (as opposed to a universal constant). Since the passive scalar structure functions are a function of the dissipation rates of both the turbulent kinetic energy and scalar variance, the expression above includes the correlation between χ_r and ϵ_r (which was not required for the KOC prediction). This consideration complicates the analysis, since one must know (or assume) the form of the joint probability distribution of χ_r and ϵ_r (to obtain an estimate of their correlation coefficient, denoted

herein by ρ). Assuming that the joint probability distribution of the dissipation rates is a bivariate log-normal distribution (with a constant correlation coefficient), Van Atta (1971) derived the following expression for the inertial-convective-range scaling exponents of the passive scalar field:

$$\langle (\Delta\theta)^n \rangle = K_n r^{n/3} \chi^{n/2} \epsilon^{-n/6} (\ell/r)^{\mu n(n(5-3\rho)-6)/36},$$

assuming that $A_\theta = A$ and $\mu_\theta = \mu$. The above expression can be re-arranged to isolate the scaling exponent for r , such that:

$$\xi_n = \frac{n}{3} - \frac{\mu n}{36} [n(5-3\rho) - 6].$$

Upon examination of the expressions above for the velocity and passive scalar structure function scaling exponents, one observes that the two expressions are similar. Both expressions include the K41/KOC $n/3$ prediction, in addition to a correction, which is a function of the intermittency exponent. Given this observation, one of the most commonly encountered measures of internal intermittency are the inertial-range scaling exponents of the high-order (velocity and passive scalar) structure functions, or, more precisely, their departure from the K41/KOC theoretical prediction of $n/3$. Moreover, the expressions derived above suggest that the structure function scaling exponents (for both the velocity and passive scalar fields) exhibit a parabolic variation with structure function order. Frisch (1995) demonstrated that the structure function scaling exponents must be a concave-down, non-decreasing function of the structure function order — a condition that is clearly violated by the K62 prediction. A second discrepancy also arises from the fact there exists numerous methods to quantify the intermittency of both the velocity and passive scalar fields. Sreenivasan & Kailasnath (1993) described multiple techniques to determine the intermittency exponent, each yielding somewhat different

values. Consequently, the “correct” values of both intermittency exponents remains a topic for debate. (However, Sreenivasan & Kailasnath (1993) propose that the respective values for the internal intermittency of the velocity and passive scalar fields are $\mu = 0.25 \pm 0.05$ and $\mu_\theta = 0.35$.) Nevertheless, numerous investigators continue to make use of the structure function scaling exponents as a measure of the internal intermittency, since their departure from the Kolmogorov prediction arises due to the effects of internal intermittency.

Given the widespread use of the velocity (and passive scalar) structure function scaling exponents as measures of the internal intermittency, the first set of experiments in the present work (from here on in referred to as the “internal intermittency experiments”) examines whether such statistics exhibit a dependence on the scalar-field boundary conditions. Consequently, the following section summarizes the literature pertaining to measured structure functions in a variety of laboratory, atmospheric and simulated flows.

1.2.2 Velocity and Passive-Scalar Structure Functions

Velocity structure functions have been measured in a variety of laboratory and atmospheric flows, as well as in numerical simulations. Frenkiel & Klebanoff (1967) were among the first to examine the higher-order statistics of the turbulent velocity field. In particular, they examined the high-order correlation coefficients of the velocity increments (up to the eighth order) as a function of the (temporal) separation. (One may easily demonstrate that the n^{th} -order correlation examined therein is simply the n^{th} -order structure function normalized by the second-order structure function.) Their results revealed that the high-order moments depart from Gaussianity at small separations. Unfortunately, given the low Reynolds number of the flow ($Re_\lambda = 55$),

they did not observe an inertial subrange and, therefore, could not compute the scaling exponents.

Van Atta & Chen (1970) examined the structure functions of the turbulent velocity field (up to fourth-order) in the atmospheric boundary layer above the ocean to study the inertial-range scaling. The scaling exponents measured therein were in agreement with the K41 prediction at low orders. However, at fourth-order, they observed a discrepancy between the measured exponent and the value predicted using Kolmogorov theory. In this case, Kolmogorov's modified theory yielded more accurate predictions. Van Atta & Park (1972) extended the previous work of Van Atta & Chen (1970) to examine the inertial-range exponents up to ninth-order. The refined Kolmogorov theory accurately predicted the scaling exponents up to seventh-order. (However, the authors conceded that their data may suffer from convergence issues for $n \geq 5$.)

Antonia, Satyaprakash & Chambers (1982) examined the influence of the Reynolds number on the high-order structure functions by considering a variety of laboratory shear flows (i.e. a circular jet with $379 \leq Re_\lambda \leq 966$ and a plane jet with $531 \leq Re_\lambda \leq 728$) as well as measurements made in the atmospheric surface layer (with a Reynolds number range of $7353 \leq Re_\lambda \leq 8995$). They found that K62 theory successfully predicted the evolution of the structure functions with Reynolds number.

Anselmet *et al.* (1984) studied the high-order structure functions (up to order $n = 18$) for the velocity fields within a turbulent jet (up to Reynolds number $Re_\lambda = 852$) and in a turbulent duct flow (for $Re_\lambda = 515$). The authors examined the log-normal model proposed in Kolmogorov (1962) in the context of its ability to accurately predict the scaling exponents of the high-order velocity structure functions. They determined that the log-normal model was accurate up to the twelfth order. However, beyond the twelfth

order, the measured exponents continued to increase in magnitude, whereas the K62 prediction decreases with increasing structure function order (since the expression for the scaling exponent is quadratic with structure function order).

Maurer, Tabeling & Zocchi (1994) examined the structure functions in a turbulent flow generated by means of two counter-rotating disks in low-temperature helium. While the resulting flow is highly complex, it nevertheless provides a relatively large Reynolds number (as compared to other laboratory flows). The authors presented scaling exponents for a Reynolds number of $Re_\lambda \approx 1200$, which, the authors concluded, were comparable to the values previously presented in the literature. Belin, Tabeling & Willaime (1996) later expanded upon the previous experiment by examining the variation of the scaling exponents with Reynolds number. Their observations revealed very little variability in the measured exponents (for the fourth-, sixth- and eighth-order moments) over the range of Reynolds numbers examined therein (i.e. $150 \leq Re_\lambda \leq 5040$).

Vincent & Meneguzzi (1991) were among the first to examine the higher-order scaling exponents using direct numerical simulation of statistically stationary, homogeneous, isotropic turbulence at $Re_\lambda \approx 150$. The authors presented the scaling exponents for $n < 30$ and determined that their results were consistent with those of Anselmet *et al.* (1984) — i.e. the scaling exponents measured therein agreed well with the log-normal prediction of Kolmogorov (1962) at low orders. However, the scaling exponents increased monotonically with the structure function order (and, therefore, did not exhibit the decrease predicted by the log-normal model).

Boratav & Pelz (1997) examined the inertial-range scaling exponents of decaying turbulence at $Re_\lambda \sim 100$ using direct numerical simulation. The scaling exponents were determined using a number of different techniques and compared to numerous theoretical predictions. They determined that the model proposed by She & Leveque (1994) provided the most accurate estimates of the longitudinal velocity structure function scaling exponents. Moreover, the authors expanded upon the previous model to include additional free parameters and determined that the new model was equally capable of providing accurate estimates of the exponents.

Gotoh *et al.* (2002) examined a variety of velocity statistics, including the scaling exponents of both the longitudinal and transverse structure functions (up to tenth order), using a high-resolution (1024^3 grid points) simulation. They reported distinct differences in the longitudinal and transverse structure functions, notably that (i) the transverse velocity structure function presents a wider inertial scaling range than the longitudinal velocity structure function and (ii) the “cross-over scale” (i.e. from the viscous-dominated regime to the inertial region) for the longitudinal structure function is larger than the analogous value for the transverse structure function. (However, both values are on the order of the Taylor microscale of the flow.)

Along with the experimental and numerical experiments described above, the evolution of the structure function scaling exponents with structure function order has received significant theoretical consideration from numerous investigators. Frisch, Sulem & Nelkin (1978) proposed a phenomenological intermittency model known as the “ β model,” which assumes that as the large eddies break up into smaller eddies, they become less “space-filling.” The implication of such a model is that the smallest eddies, which are responsible for the dissipation of turbulent kinetic energy into internal energy, occupy a much

smaller volume than the largest eddies. This yields tiny regions over which the bulk of the dissipation occurs, a phenomenon that is reminiscent of that observed due to internal intermittency. Using this model, Frisch *et al.* (1978) derived the following expression for the velocity structure function scaling exponent:

$$\zeta_n = \frac{1}{3}(3 - D)(3 - n),$$

where D is the fractal dimension, which is related to the intermittency exponent, μ , such that $D = 3 - \mu$. On the other hand, She & Leveque (1994) proposed a hierarchical model using the ratio of the moments of the dissipation rate of turbulent kinetic energy. Moreover, they suggested that the relationship between the successive moments of the dissipation rate of turbulent kinetic energy is universal. This assumption yields the following expression for the inertial-range scaling exponents:

$$\zeta_n = \frac{n}{9} + 2 \left[1 - \left(\frac{2}{3} \right)^{n/3} \right].$$

Chen & Cao (1995) developed an extension of the She & Leveque (1994) hierarchical model that incorporates the scaling exponents of the locally-averaged dissipation function (as proposed by Novikov, 1994). The authors demonstrated that the resulting expression:

$$\zeta_n = \frac{9}{2} \left[1 - \left(\frac{7}{9} \right)^{n/3} \right],$$

yields accurate predictions of the scaling exponents (when compared to both experimental data and previous theoretical predictions) up to the tenth order. Moreover, their model predicts that the scaling exponents eventually asymptote to a finite value, in the limit of infinite structure function order. Finally, Camussi & Verzicco (2000) employed the probability density functions of the

turbulent kinetic energy fluctuations to obtain a recursive formula for the velocity structure function scaling exponents (which depends solely on the scaling exponent of the first-order structure function). The motivation for this model stems from the notion that the coherent structures within a turbulent flow are solely responsible for the internal intermittency, which, in turn, yields exponential PDFs for the turbulence kinetic energy. Consequently, they derived the following expression for the structure function scaling exponents:

$$\zeta_n = \zeta_{n-1} + \frac{\log n}{\log 6} (1 - 3\zeta_1) + \zeta_1.$$

A similar analysis of the high-order passive scalar structure functions has also been presented in the literature. Antonia & Van Atta (1978) examined the structure functions of the temperature fluctuations in laboratory flows (i.e. a thermal boundary layer and a heated jet), as well as the atmospheric surface layer. They also examined the evolution of the structure functions with Reynolds number. (However, they did not compute the inertial-convective range scaling exponents.) Moreover, they also observed that the odd-order temperature structure functions exhibited a significant departure from the Kolmogorov prediction (i.e. the value of zero, as required to satisfy local isotropy.) The authors attributed this discrepancy to “ramp-like” structures within the fluctuating temperature field, which arise due to the anisotropic large-scale features of turbulent shear flows.

Antonia *et al.* (1984) measured the scaling exponents of the high-order temperature structure functions (up to $n = 12$) in a weakly-heated turbulent jet at $Re_\lambda \approx 850$. Their experiments revealed that the magnitude of temperature scaling exponents was smaller than the velocity scaling exponents for a comparable flow (i.e. Anselmet *et al.*, 1984), with the difference increasing

with structure function order. The authors concluded that differences may exist between hydrodynamic and passive scalar internal intermittency.

Meneveau *et al.* (1990) examined the intermittent velocity and scalar fields in the heated wake of a cylinder using a joint multifractal formalism. While the primary objective of this paper was to develop a multifractal formalism to describe intermittent fields, the authors demonstrated that the proposed technique could also be applied to practical turbulence problems. Moreover, using this technique, the authors computed the temperature structure function scaling exponents, which are smaller than those presented by Antonia *et al.* (1984) at higher orders.

Ruiz-Chavarria *et al.* (1996) also examined the heated wake downstream of a cylinder. In contrast to the work of Meneveau *et al.* (1990), the authors employed a “mandoline” (an array of fine, heated wires) to inject the scalar into the flow. (Note that the experimental configuration employed in Ruiz-Chavarria *et al.* (1996) is similar to the “mandoline experiment” described in the present work — see sections 3.1 and 4.1.) The authors examined the passive scalar structure function scaling exponents and proposed (and experimentally verified) a hierarchical model for the temperature structure functions, akin to that proposed by She & Leveque (1994).

Both Chen & Cao (1997) and Chen & Kraichnan (1998) employed direct numerical simulation of isotropic turbulence to examine the high-order structure functions of the passive scalar field, as well as the inertial-convective range scaling exponents. While the former examined the relationship between the structure of the internal intermittency and the structure function scaling exponent, the latter studied the conditional expectation of the dissipation rate

of scalar variance (along with its moments). In both cases, the authors demonstrated that direct numerical simulations of passive scalar turbulence can be successfully employed to determine the structure function scaling exponents.

Theoretical predictions of the evolution of the structure function scaling exponents with the structure function order have also been proposed. For example, Kraichnan (1994) examined the influence of the molecular diffusion term of the Navier-Stokes equations on the passive scalar structure functions and derived an expression for the structure function scaling exponents, such that:

$$\xi_{2n} = \frac{1}{2} \sqrt{4nd\xi_2 + (d - \xi_2)^2} - \frac{1}{2} (d - \xi_2),$$

where ξ_2 is the scaling exponent of the second-order structure functions and d is a general dimension of space. Cao & Chen (1997) proposed a phenomenological model for the inertial-range scaling exponents, which the authors derived using a bivariate log-Poisson model. Their expression:

$$\xi_n = 3 - \frac{n}{36} - 2 \left(\frac{3}{4} \right)^{n/6} - \left(\frac{1}{2} \right)^{n/2} + \gamma \left[1 - \left(\frac{3}{4} \right)^{n/6} - \left(\frac{1}{2} \right)^{n/2} + \left(\frac{3}{4} \right)^{n/6} \left(\frac{1}{2} \right)^{n/2} \right],$$

where γ is a free (i.e. modelling) parameter, exhibited a good agreement with the experimental data, provided $\gamma = 0$. The authors suggested that such a result is indicative of a weak correlation between the volume-averaged dissipation rates of turbulent kinetic energy and scalar dissipation. Meanwhile, L ev eque *et al.* (1999) built upon the previous model of She & Leveque (1994) to obtain an expression for the inertial-convective range scaling exponents, which reads:

$$\xi_n = \frac{n}{9} + \left(\frac{10}{9} \right) \left[1 - \left(\frac{2}{5} \right)^{n/3} \right].$$

Gylfason & Warhaft (2004) examined both the longitudinal and transverse temperature structure functions in grid-generated turbulence (for $150 \leq Re_\lambda \leq 700$) with a uniform mean temperature gradient. They determined

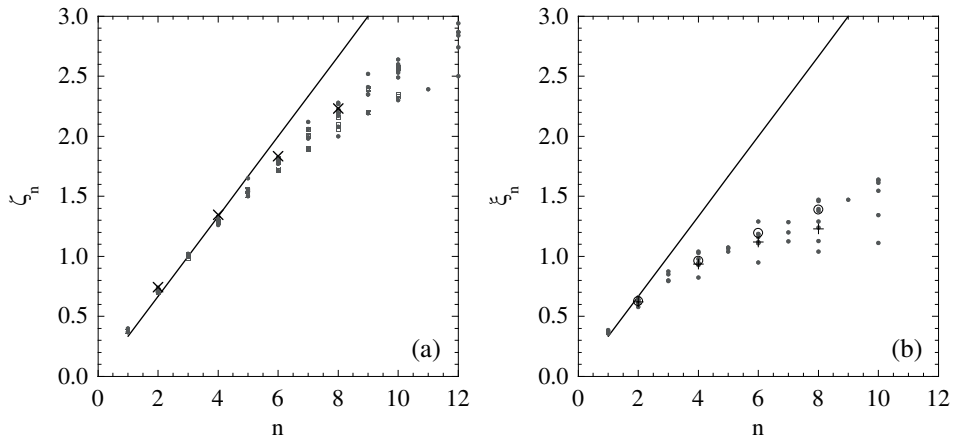


Figure 1.1: The inertial(-convective) range scaling exponents of the (a) velocity and (b) passive scalar fields, obtained from the published literature. In (a): \times : Present work. \bullet : Anselmet *et al.* (1984), Maurer *et al.* (1994), Belin *et al.* (1996), Vincent & Meneguzzi (1991), Boratav & Pelz (1997), Gotoh *et al.* (2002). Solid line: K41 ($n/3$). \square : ESS data of Arneodo *et al.* (1996). In (b): \circ : Present work, heated cylinder experiment. $+$: Present work, mandoline experiment. \bullet : Antonia *et al.* (1984), Meneveau *et al.* (1990), Ruiz-Chavarria *et al.* (1996), Gylfason & Warhaft (2004), Chen & Cao (1997), Chen & Kraichnan (1998), Watanabe & Gotoh (2006). Solid line: KOC ($n/3$).

that the passive scalar structure function scaling exponents (i) exhibited no dependence on the Reynolds number and (ii) were the same for both the longitudinal and transverse cases. In addition to their results, they presented a compilation of the passive scalar scaling exponents obtained from the literature, noting that there exists a considerable scatter in the experimentally determined data. Figure 1.1 presents a compilation of the (a) velocity and (b) temperature scaling exponents obtained from the literature. One notices that the velocity scaling exponents exhibit a reasonable collapse at all orders, excluding the data of Belin *et al.* (1996), whereas the passive scalar exponents reveal a considerable scatter in the data at high-orders. Gylfason & Warhaft (2004) remarked that such a variation could result from (i) convergence issues at high-orders, (ii) “clipping” of large fluctuations due to finite experimental (and computational) domains, and (iii) differences in the initial/boundary conditions of the flow.

Watanabe & Gotoh (2006) examined the high-order passive scalar structure function scaling exponents using high-resolution direct numerical simulations. In particular, their simulations examined an isotropic turbulent flow advecting two different passive scalar fields: (i) a random, Gaussian (white in time) source (at $Re_\lambda = 427$), and (ii) a uniform mean scalar gradient (at $Re_\lambda = 468$). Consistent with the work of Gylfason & Warhaft (2004), they observed that the inertial-range scaling exponents for the longitudinal and transverse structure functions were approximately equal (for the uniform mean scalar gradient experiment). Moreover, their results revealed a significant discrepancy between the scaling exponents generated by the two different scalar sources.

Having summarized the literature pertaining to the first set of experiments examined in this thesis, i.e. the influence of the scalar-field boundary

conditions on passive scalar mixing, the following section examines the literature pertaining to the second set of experiments presented herein, which treats the mixing that occurs downstream of concentrated sources within turbulent flows.

1.2.3 Dispersion from Concentrated Sources

A theoretical background for the diffusion of passive contaminants by turbulent flows was first provided by Taylor (1921), who examined the fundamental properties of a turbulent flow that are responsible for the dispersion that occurs due to the motion of the turbulent fluid particles.² Thereafter, the experiments of Taylor (1935), Uberoi & Corrsin (1953) and Townsend (1954) presented the development of the mean and fluctuating thermal fields downstream of a thermal line source in (homogeneous, isotropic) grid turbulence. These experiments revealed that the mean temperature profile is well represented by a Gaussian distribution. Subsequent work revealed that the evolution of the mean temperature field can be divided into three stages: (i) a molecular diffusive regime, (ii) a turbulent convective regime and (iii) a turbulent diffusive regime (Warhaft, 1984; Anand & Pope, 1985; Stapountzis *et al.*, 1986). In the molecular diffusive range ($t \ll \alpha / \langle v^2 \rangle$, where t is the “flight-time” from the source, α is the scalar diffusivity and $\langle v^2 \rangle$ is the mean-square transverse velocity fluctuation), the width of the plume (σ) grows as $\sigma \propto (\alpha t)^{1/2}$. The turbulent convective regime, $\alpha / \langle v^2 \rangle \ll t \ll t_L$, where t_L is the Lagrangian integral time scale of the flow, is characterized by a linear growth rate of the plume width with time (i.e. $\sigma \propto \langle v^2 \rangle^{1/2} t$). Finally, the

² More recently, Durbin (1980) extended Taylor’s seminal work to develop the two-particle dispersion model, which better predicts the fluctuating scalar field. Shortly thereafter, Sawford & Hunt (1986) extended the model of Durbin (1980) to include the effects of molecular diffusion.

turbulent diffusive range ($t \gg t_L$) is described by $d\sigma^2/dt \propto \alpha_T$, where α_T is the turbulent scalar (or eddy) diffusivity.

Warhaft (1984) studied the downstream evolution of a passive scalar released from a concentrated line source in homogeneous, isotropic grid turbulence. The results presented therein revealed that the root-mean-square temperature profiles exhibit a transition from double-peaked (near the source) to single-peaked (at intermediate distances) and back to double-peaked once again (far downstream). In addition to the single-line-source experiments, Warhaft (1984) also examined the interference of multiple thermal plumes by means of their correlation coefficient. It was concluded that the mixedness of the resultant thermal plume was a strong function of the separation between the line sources and that the thermal fields exhibited a “destructive interference,” similar to that which occurs within wave motion.

Anand & Pope (1985) carried out numerical simulations of grid turbulence using the flow conditions examined in Warhaft (1984). Using probability density function (PDF) methods, they calculated the evolution of the mean plume for all three stages. Moreover, their computations of the scalar variance were improved by the use of a joint PDF method conditioned on the transverse velocity at the source location. Viswanathan & Pope (2008) studied the scalar dispersion from one, two and multiple line sources in decaying grid turbulence. Their implementation of the interaction by exchange with the conditional mean (IECM) model, in conjunction with their PDF methods, yielded accurate results for a variety of scalar statistics.

Nakamura *et al.* (1986) and Sakai *et al.* (1986) studied the mean and fluctuating scalar fields (respectively) downstream of a concentrated point

source in uniformly sheared turbulence. Their results indicated that the decay rates of the centreline mean and root-mean-square (r.m.s.) scalar concentrations, as well as the lateral and transverse growth rates of the mean scalar profiles, all exhibited a dependence on the magnitude of the mean-flow shear. Karnik & Tavoularis (1989) examined the influence of anisotropy (shear) on the dispersion from a line source in homogeneous turbulent shear flow. They obtained mean temperature profiles that were initially Gaussian (i.e. close to the source); however, far downstream, the profiles become asymmetric with peaks shifting towards the lower velocity region. In addition, they also measured r.m.s. temperature profiles that evolved from double-peaked (close to the source), to single-peaked (at intermediate distances) and back to double-peaked once more (far downstream), consistent with the observations of Warhaft (1984). Their results also included various velocity–temperature statistics (e.g. joint PDFs, turbulent fluxes, etc.).

While the study of scalar dispersion in homogeneous turbulence provides invaluable insight into the underlying physical mechanisms responsible for the mixing of scalar contaminants, the majority of engineering and naturally occurring turbulent flows are inhomogeneous. In order to explicitly isolate the influence of the inhomogeneity, Lavertu & Mydlarski (2005) performed experiments that will be of particular relevance to the experiments described herein. They studied the (transverse) dispersion from a concentrated line source in fully developed, high-aspect-ratio turbulent channel flow — the most fundamental inhomogeneous flow, given that the inhomogeneity of the velocity field is confined to only one direction (the wall-normal direction). The line source was oriented parallel to the channel walls, thus creating a statistically two-dimensional temperature field, and transverse dispersion profiles were measured in the wall-normal direction for a variety of downstream positions and

wall-normal source locations. They presented mean and fluctuating temperature profiles, which were well approximated by truncated Gaussian distributions, in addition to presenting temperature probability density functions and various mixed velocity–temperature statistics.

In light of the practical considerations pertaining to atmospheric pollutant dispersion, the development of a plume released from elevated (as well as ground) sources in a turbulent boundary layer has also received significant attention. Shlien & Corrsin (1976) presented the mean temperature profiles for both a ground-level and elevated line source in a turbulent boundary layer. Their results indicated that the mean profiles approached an asymptotic form, regardless of the source elevation. Furthermore, they determined that a suitably defined turbulent Prandtl number was of the order of unity.

Fackrell & Robins (1982) examined both the lateral and transverse evolution of ground-level and elevated point sources issuing into a turbulent boundary layer. They presented statistics of the (mean and fluctuating) concentration field, along with measurements of various turbulent fluxes, for both the vertical (i.e. transverse) dispersion, and, to a lesser extent, the lateral dispersion. They determined that the lateral profiles of the temperature variance were slightly broader than a Gaussian distribution and exhibited very little changes with downstream position. Finally, they observed that these profiles displayed little variation for different source heights as well.

Paranthoën *et al.* (1988) studied the dispersion from a line source in both a turbulent boundary layer and a plane jet. Their results included the mean and fluctuating temperature fields, in addition to a re-scaling scheme, which makes use of the Lagrangian integral time scale of the transverse velocity fluctuation (see also Dupont, El Kabiri & Paranthoën, 1985), that provided a reasonable

collapse of the (mean) statistics from both flows. Unfortunately, the scheme was not as successful in collapsing the fluctuating statistics.

Direct numerical simulations of the dispersion of passive scalars within turbulent flows has also been presented by numerous investigators. For example, Brethouwer *et al.* (1999) examined fully developed pipe flow with a point source located at the pipe centreline by means of numerical simulations. They calculated the mean and fluctuating concentration profiles, turbulent fluxes, as well as PDFs of the concentration. Their results were in good agreement with the relevant experimental data, thereby confirming the validity of using direct numerical simulations in the study of turbulent mixing.

Vrieling & Nieuwstadt (2003), on the other hand, considered the mean and fluctuating scalar statistics for a single and multiple line sources in channel flow, in a manner analogous to the work of Warhaft (1984) — i.e. they examined profiles of the root-mean-square concentration fluctuation, as well as the downstream evolution of the plume half-width and, in the case of multiple line sources, the correlation coefficient. Finally, they proposed a new dispersion model, based predominantly on the fluctuating plume model proposed by Gifford (1959), which permitted the authors to extend the results of their numerical simulation to atmospheric flows.

Hanratty and his numerous collaborators — e.g. Lyons, Hanratty & McLaughlin (1991), Kontomaris & Hanratty (1994), Papavassiliou & Hanratty (1997), Iliopoulos & Hanratty (1999) and Na & Hanratty (2000) — performed multiple numerical simulations of scalar dispersion in turbulent channel flow (using a variety of scalar boundary conditions, including both heated walls and point sources). Their results demonstrated that direct numerical simulations of dispersion within channel flow could be used to obtain reliable estimates of numerous passive scalar statistics.

Bakosi *et al.* (2007) studied the dispersion from a concentrated line source in fully developed turbulent channel flow using PDF methods. They also examined the influence of different mixing models (more precisely, the interaction by exchange with the mean and the interaction by exchange with the conditional mean) on the resultant small-scale mixing of the passive scalar. They concluded that the interaction by exchange with the conditional mean model provided a better agreement with the experimental data of Lavertu & Mydlarski (2005). (Unfortunately, this comes at the expense of increased computational time.)

Finally, Boppana *et al.* (2012) performed large-eddy simulations of turbulent channel flow with dispersion from a concentrated source using the same experimental conditions as those presented in Lavertu & Mydlarski (2005). Their numerical results were in reasonable agreement with those determined by Lavertu & Mydlarski (2005), thereby illustrating the promise of using large-eddy simulations in practical flows.

1.3 Structure of Thesis

The remainder of this thesis is organized as follows. The experimental apparatuses are presented in Chapter 2. A description of the experimental conditions, as well as the corresponding flow validation, is discussed in Chapter 3. Results are presented and discussed in Chapter 4, which pertains to the influence of the (i) scalar-field (section 4.1) and (ii) velocity-field (section 4.2) boundary conditions on the structure of the turbulent passive scalar within inhomogeneous turbulent flows. The former examines different statistics that are commonly employed to characterize the internal intermittency of the passive scalar field and whether they exhibit a dependence on the large-scale features of the temperature field. The latter section presents statistics pertaining to the mixing of a passive scalar and attempts to identify the influential parameters,

with particular emphasis on the velocity-field boundary conditions. Finally, the conclusions are summarized in Chapter 5.

CHAPTER 2

Experimental Apparatus

The experiments described herein were conducted in the Aerodynamics Laboratory in the Department of Mechanical Engineering at McGill University. Two different experimental facilities were employed. The internal intermittency studies were conducted in the open-circuit, suction-type, low-background-turbulence wind tunnel (Beaulac & Mydlarski, 2004; Berajeklian & Mydlarski, 2011), whereas the lateral dispersion measurements were obtained using the channel flow facility (Lavertu & Mydlarski, 2005; Costa-Patry & Mydlarski, 2008). The details of each facility, the instrumentation, and the data acquisition processes, are described below.

2.1 Wind Tunnel Facility

The plenum of the open-circuit wind tunnel contains a flow-conditioning section, which consists of an aluminum honeycomb flow straightener, followed by a series of four stainless steel wire screens. It is connected to the test section by a contraction with a 9 to 1 area ratio. The profile of the contraction follows a fifth-order polynomial. The $85 \times 122 \times 274 \text{ cm}^3$ test section has beveled corners (that decrease in size with downstream distance, thus providing an increasing cross-sectional area) to ensure a constant velocity therein. Upon exiting the test section, the flow enters an 8.84 m-long shallow-angle diffuser, which connects to a 2.13 m-diameter axial fan powered by a 125 hp AC motor. To ensure a steady flow in the test section, a Unico controller maintains the rotational speed of the fan to within $\pm 0.5\%$ of the set point.

In the present work, the flow under consideration is the turbulent wake downstream of a circular cylinder. Since the objective of the current research

is to investigate the inertial-convective range scaling of a variety of turbulent statistics, the Reynolds number of the flow must be sufficiently large. However, the temporal resolution of the cold wire limits the maximum flow velocity. Consequently, the cylinder diameter was selected to be as large as possible, while taking into consideration the limited downstream extent of the experimental facility. (For downstream positions less than 30 diameters, the wake is not yet fully turbulent and still externally intermittent.) Therefore, to generate the hydrodynamic wake, a circular cylinder of diameter $D = 73.0$ mm was installed at the entrance of the tunnel test section, which yields a Taylor-microscale Reynolds number of 370. It was oriented vertically and spanned the entire extent of the test section. To inject the scalar (temperature) into the flow, a 1.5 kW electric heating element was installed within the cylinder. Energizing the heating element yields a “heated cylinder,” which was one of the two methods for injecting the scalar into the flow field. The other required a “mandoline” be installed 10 diameters downstream of, and oriented parallel to, the cylinder (see figures 2.1 and 2.2). The downstream position of the mandoline was selected by taking into consideration the data of Beaulac & Mydlarski (2004), who determined that the scalar field generated by a mandoline installed at this position would evolve in a manner similar to the scalar field downstream of the heated cylinder. (More precisely, Beaulac & Mydlarski (2004) determined that the scalar variance of the two fields decays at a similar rate.)

First introduced by Warhaft & Lumley (1978), the mandoline consists of an array of fine, Nichrome wires that are stretched across the wind tunnel test section. When energized (using a DC power supply capable of providing 1.2 kW), the individual plumes of the multiple wires grow and rapidly mix, thus providing a second method of heating the wake. To prevent the wires from

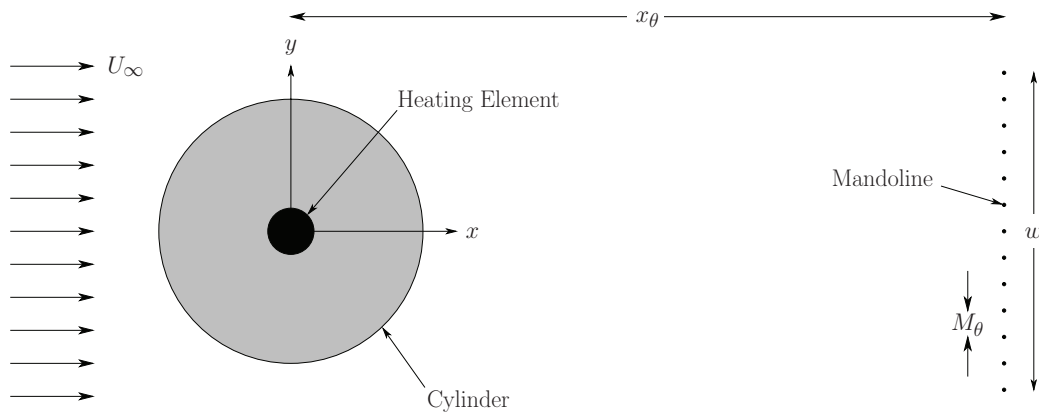


Figure 2.1: Schematic illustrating the experimental configuration of the internal intermittency experiment. A heating element is embedded within the cylinder that generates the hydrodynamic wake (thus creating a “heated cylinder”). In addition, a “mandoline” is installed downstream of the cylinder. The hot- and cold-wire sensors are located 30 diameters downstream of the cylinder and along its axis (corresponding to non-dimensional coordinates of $x/D = 30$ and $y/D = 0$). $x_\theta/D = 10$ in the current research. Not to scale.



Figure 2.2: Picture of the open-circuit wind tunnel test section with the current experimental apparatus installed. The hot- and cold-wire probes are mounted on a stepper-motor-controlled traversing mechanism, which enables the probes to travel in the transverse (i.e. y -) direction.

sagging when heated, small springs are attached to one end of each wire to keep them in tension. In the current configuration, thirteen 36 AWG (0.127 mm in diameter) wires were employed, evenly spaced 7.6 mm apart (yielding a total mandoline width of 91.4 mm). Moreover, given the small diameter of the individual wires, the presence of the mandoline does not disturb the hydrodynamic field (see section 3.1), and, consequently, the velocity field was the same when either scalar injection mechanism was used.

2.2 Channel Flow Facility

The airflow for the channel is provided by a Hudson Buffalo centrifugal blower, powered by a 7.5 hp AC motor. The motor speed is controlled using an ABB ACS 600 frequency converter. A filter box was installed at the blower intake (preventing particles larger than $3\ \mu\text{m}$ from entering the test section). A flow conditioning section was attached to the blower outlet using a flexible rubber coupling to minimize the transmission of any motor vibrations to the test section. The former consisted of a (i) wide-angle diffuser, (ii) settling chamber and (iii) contraction.

The wide-angle diffuser decelerates the flow prior to entering the settling chamber, thereby allowing the flow more time to settle. However, given the wide wall angle of the diffuser (approximately 45°), flow separation within the diffuser is possible, unless otherwise prevented. Consequently, four screens are located within the diffuser (with an appropriately chosen separation between them) such that the pressure drop across the screen balances the pressure rise due to the diffuser. This reduces the likelihood of flow separation. The settling chamber is a constant-area rectangular duct with a honeycomb section, followed by a series of six screens, which serves to straighten the flow and remove any undesirable fluctuations in the velocity field. Finally, the contraction located at the end of settling chamber is two-dimensional, with an area ratio

of approximately eight. Moreover, the shape of the contraction follows a fifth-order polynomial. Upon exiting the contraction (i.e. before entering the test section), the flow is (almost) uniform and has a turbulence intensity of 0.25%. (See McLeod (2000) for a thorough description of the design and construction of the flow conditioning section.) The channel test section measures 8 m long, 1.1 m high and 0.06 m wide. The boundary layer is tripped at the entrance of the test section by means of two rods (3.2 mm in diameter) located 60 mm downstream of the entrance and 3 mm from each wall. Due to the channel's large aspect ratio (≈ 18), the flow field may be considered two-dimensional at the centre of the channel. Experiments are conducted in the final metre of the test section, where the flow is fully developed (see section 3.2).

In Lavertu & Mydlarski (2005) and Costa-Patry & Mydlarski (2008), the channel test section was configured for two-dimensional transverse dispersion measurements. Consequently, the line source was oriented in the spanwise (vertical, z -) direction and measurements of the transverse (y -direction) profiles of the thermal plume were obtained at different downstream distances, and for a variety of wall-normal source locations. This should be contrasted with the present work, which studies three-dimensional lateral dispersion and therefore requires the measurement of spanwise (z -direction) profiles of the plume emitted from a line source oriented in the wall-normal (y -) direction. The two configurations are best described by a schematic (see figure 2.3).

The measurement of lateral profiles downstream of a wall-normal line source required modifications to the channel. To this end, a 12-mm-deep groove running the entire height of the channel (in the spanwise direction) was machined in the channel wall, 7.5 m from the channel entrance. Its width and depth were selected to receive an aluminium "slider" (through which probes were inserted and whose length exceeded the width of the channel), permitting

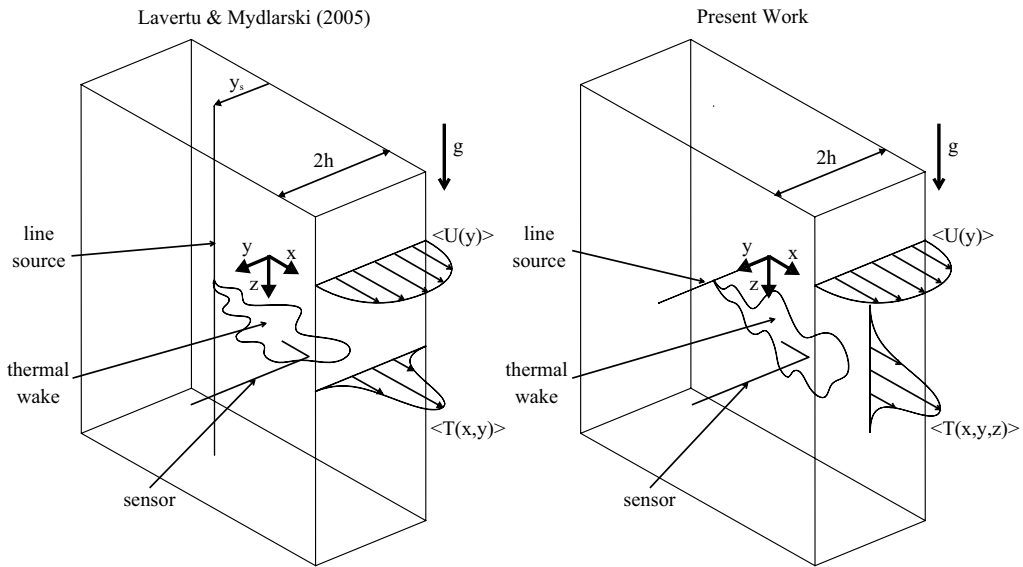


Figure 2.3: Schematic illustrating the transverse (left) and lateral (right) dispersion problems studied in Lavertu & Mydlarski (2005) and the current work, respectively. Note that the thermal plume is statistically two-dimensional in the former case, whereas it is three-dimensional in the latter (i.e. current) case. Also note the location and orientation of the line sources and the coordinate axes. (y is defined as the transverse direction and z is the lateral direction, herein.) Not to scale.



Figure 2.4: Picture of the modified channel test section with a sliding access port for the hot- and cold-wire sensors. The latter were positioned by a two-axis linear traversing mechanism, enabling movement in the y (transverse) and z (lateral) directions.

lateral profiles to be measured while preserving the hydrodynamic smoothness of the wall along its entire height. The slider thus served as an access port for the hot- and cold-wire sensors. Using this arrangement, the sensors could travel in both the wall-normal (y) and spanwise (z) directions. Given that the flow was fully-developed, it was possible (and much more convenient) to move the line source (rather than the sensor) to change the downstream distance. Therefore, six ports were added upstream of the slider on each of the two (major) channel walls. They served as access ports for the line source and were located such that the six downstream measurement positions studied in Lavertu & Mydlarski (2005) were reproduced in the present experiments. The modified channel test section is shown in figure 2.4.

The scalar (temperature) was injected via fine Nichrome wires (0.254 mm in diameter) that spanned the channel in the wall-normal direction. Outside the channel, small weights were hung from the ends of each wire to counteract the effects of thermal expansion, thus keeping the wire taut. The wire was heated using a DC power supply whose voltage and current output were continuously monitored to ensure the power supplied to the wire was constant (both during an experiment and from one experiment to the next). A power input of 76 W m^{-1} was selected, given the inherent competition between improving the signal-to-noise ratio and minimizing both buoyancy and contamination from heating of the ports.

Spanwise temperature profiles were obtained at six downstream positions ($x/h = 4.0, 7.4, 10.8, 15.2, 18.6$ and 22.0) and six wall-normal separations ($y/h = 0.10, 0.17, 0.33, 0.50, 0.67$ and 1.0) for a total of 36 different cases. (Note that the channel is $2h$ wide.) The positioning of the hot- and cold-wire

sensors, in both the wall-normal and spanwise directions, was accomplished using a two-axis Velmex BiSlide precision-stepper-motor-driven linear traversing mechanism capable of moving in increments of 0.01 mm.

2.3 Instrumentation

Hot-wire anemometry and cold-wire thermometry were used to measure the longitudinal velocity and temperature fields, respectively. The former is described in section 2.3.1 below, whereas the latter is presented in section 2.3.2.

2.3.1 Hot-Wire Anemometry

The hot-wire sensor consists of a fine tungsten wire ($3\ \mu\text{m}$ in diameter and $\sim 500\ \mu\text{m}$ in length) that forms one arm of a Wheatstone bridge circuit. Electronic instrumentation maintains that arm of the bridge at a constant resistance (such that the temperature of the sensor is greater than that of the flow). Hence, the “hot-wire” undergoes convective heat transfer with the flow. To maintain the constant resistance of the sensor, the instrumentation must adjust the power supplied to the wire to balance the energy lost by convection. Therefore, by measuring the power supplied to the wire, one can use convective heat transfer theory to infer the flow velocity (U) from the voltage applied to the sensor (E).

Calibration of the hot-wire sensors employed the semi-theoretical relationship known as “King’s Law” (see, for example Bruun, 1995), which states that:

$$E^2 = A + BU^n,$$

where A , B and n are constants determined via calibration. While the former expression is typically valid for isothermal flows, Lienhard & Helland (1989) proposed a modified version of the expression that incorporates temperature-dependent coefficients, to account for variations in the flow temperature. In

this case, A and B are no longer constants. Instead, the King's Law calibration is performed over a range of fixed temperatures, spanning the range of desired flow velocities. For each temperature setting, the value of n is held constant and the calibration constants A and B are determined. The A and B data are then curve fit to the following expressions:

$$A = \bar{A} \left(\frac{T_w + T_f}{2} \right)^{0.84} (T_w - T_f),$$

and:

$$B = \bar{B} (T_w - T_f),$$

where T_f is the flow temperature and \bar{A} , \bar{B} and T_w are calibration constants, the latter being representative of the hot-wire temperature. The curve fit coefficients obtained from this plot are then used in the expressions above to determine the temperature-dependent curve-fit coefficients. Using this technique, the measured velocity field is compensated for fluctuations in the flow temperature during post-processing of the sensor output voltage. (However, this requires simultaneous measurement of both the velocity and temperature fields, which is expounded upon below.) Figure 2.5 presents typical King's Law calibration curves, obtained for a variety of fixed temperature settings.

The hot-wire sensors were calibrated using a TSI 1127 laminar calibration jet, which was modified to include the addition of electric heating elements to heat the upstream air supply. The sensors were mounted on TSI 1210 single-normal probes and operated at an overheat of 1.8 using either a TSI IFA 300 or a DISA 56C01 constant-temperature anemometer. The length-to-diameter ratio of the hot wire was approximately 200, as recommended by Bruun (1995) (to minimize the conduction effects associated with short wires).

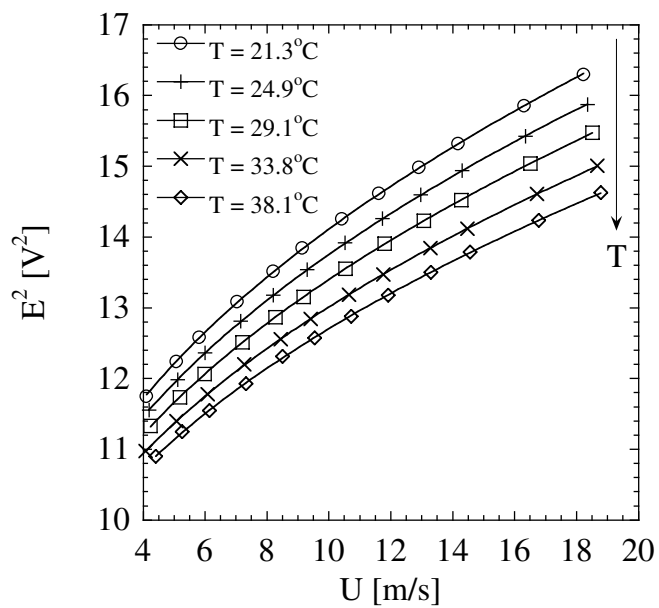


Figure 2.5: Typical calibration curves for a hot-wire sensor at different free-stream temperatures.

2.3.2 Cold-Wire Thermometry

Since the proposed research will employ temperature as the passive scalar, cold-wire thermometry is selected to measure the fluctuating temperature field, given its high spatial and temporal resolution. The cold-wire sensing element consists of a fine, platinum-alloy wire ($0.63\ \mu\text{m}$ in diameter and $\sim 500\ \mu\text{m}$ in length). The cold-wire thermometer is composed of a constant-current source that provides a small, constant-current to the sensor ($\sim 100\ \mu\text{A}$) — see, for example, Lemay & Benaïssa (2001). Therefore, the cold-wire is sensitive to changes in the flow’s temperature and consequently changes resistance as the fluid temperature changes. Since the current supplied to the sensor is constant, and given the linear relationship between temperature and resistance (over small enough ranges), one obtains a linear relationship between the flow’s temperature (T) and the voltage drop across the cold-wire sensor (E):

$$T = CE + D,$$

where C and D are calibration constants. See figure 2.6(a) for a typical temperature calibration curve.

The diameter of the cold-wire sensor plays an important role in determining the temporal resolution of the cold-wire thermometer, given that the sensor must heat up/cool down in response to changes in the flow temperature. Fine wires have a small thermal inertia and respond quickly to temperature changes, thus providing a larger frequency response. By contrast, the temporal resolution of the hot-wire sensor is principally limited by the response time of the electronic instrumentation. As such, hot-wire anemometers tend to have a much better frequency response than cold-wire thermometers. The frequency response of the cold-wire sensor is determined using the technique proposed by Lemay & Benaïssa (2001). A square-wave current signal is supplied to the

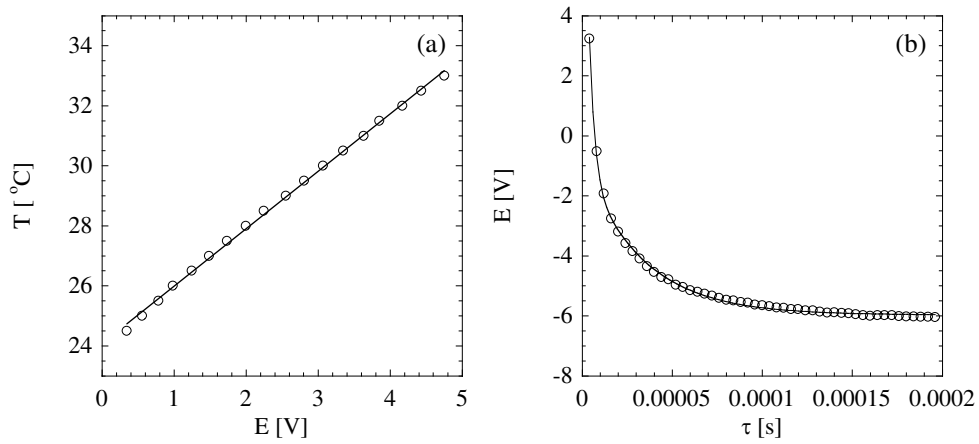


Figure 2.6: (a) Typical calibration curve for a cold-wire sensor. (b) Calculation of the frequency response of the cold-wire sensor using the method outlined in Lemay & Benaïssa (2001).

cold-wire sensor (as opposed to the constant current supplied during operation) to rapidly heat and cool the wire. During the cooling phase, a time series of the temperature signal, such as the one presented in figure 2.6(b), is obtained, and the frequency response of the cold wire is determined using an exponential curve fit. Typically, the time constant of the wire is approximately $2\text{--}3\ \mu\text{s}$, which in turn yields a frequency response on the order of 7 kHz.

Sensor length plays a crucial role in determining the spatial resolution of the sensor. One must select a sensor that is short enough to resolve the smallest features of the flow — at most 3–4 times the Kolmogorov microscale (Wynngaard, 1969, 1971) — while at the same time long enough to minimize finite-wire conduction effects — a length-to-diameter ratio 1500 is recommended for cold-wire sensors (Browne & Antonia, 1987). Given these competing effects, all of the cold-wire sensors were limited to 0.5 mm in length, to obtain the desired spatial resolution. This corresponds to a cold wire sensor with a length-to-diameter ratio of 800, which is appreciably smaller than the minimum value recommended by Browne & Antonia (1987). However, as discussed by Mydlarski & Warhaft (1998), spatial resolution errors dominate over the finite-wire conduction effects, especially when considering small-scale statistics. Consequently, the recommendation for the length-to-diameter ratio has been relaxed, to improve the spatial resolution of the sensor.

The cold-wire sensors were mounted on TSI 1210 single-normal probes. The sensors were operated by a cold-wire thermometer built at the Université Laval (Québec, Canada), consisting of the constant-current anemometry circuit described in Lemay & Benaïssa (2001), which provided a constant current of $100\ \mu\text{A}$. The modified TSI 1127 laminar jet described above was employed to calibrate the cold-wire sensors, using an electric heater to heat the air upstream of the calibration jet, while maintaining a constant flow velocity that

is similar to that observed during the experiments. LaRue, Deaton & Gibson (1975) determined that the -3 dB point of the frequency response of a $0.63\text{ }\mu\text{m}$ -diameter platinum cold wire is $\sim 5 - 6$ kHz (when operated in a flow of $5 - 10\text{ m s}^{-1}$). Given that the Kolmogorov frequencies of the flows studied herein are on the order of $4 - 7$ kHz, the temporal resolution of the cold-wire is satisfactory, and a correction, such as that proposed by Lemay & Benaïssa (2001), is not required (in addition to being found to distort some higher-order temperature statistics).

Some of the statistics examined herein required the simultaneous measurement of the turbulent velocity and temperature fields. These measurements required the use of a TSI 1244 parallel-sensor probe, upon which both a cold- and hot-wire sensor were mounted (0.5 mm apart). Both sensors were then calibrated using the techniques described above. To ensure that the wake from the hot-wire did not interfere with the cold-wire sensor mounted alongside of it, a second series of experiments were conducted in which only the cold-wire sensor was employed. The differences in the two sets of measurements was negligible (i.e. on the order of the repeatability of an experiment using one of the two sensor assemblies).

2.4 Data Acquisition

The output signals of the hot-wire anemometer and cold-wire thermometer were band-pass filtered using Krohn-Hite 3382 and 3384 filters to remove the mean component of the signal (i.e. high-pass filtered) as well as any high-frequency electronic noise (i.e. low-pass filtered). (Whenever necessary, the filtered signals were also amplified to minimize the discretization error.) The filtered signals were then digitized using a 16-bit National Instruments PCI 6143 or a PCI 6036E multifunction data acquisition card, controlled using

LabVIEW virtual instruments, and stored for future data reduction. Measurements were sampled at twice the low-pass filter frequency (in accordance with the Nyquist criterion) to obtain time series of the turbulent signals. Such data sets are necessary for power spectra, autocorrelation and structure function calculations. Statistical moments (such as the mean and root-mean-square fluctuation) on the other hand, are typically computed from data sets sampled at a frequency that roughly corresponds to the inverse of the integral time scale of the turbulence. This yields data points that are independent of each other, and are therefore better suited for the computation of statistical moments.

Since the internal intermittency experiments described herein required converged high-order moments, long data sets are required. However, the LabVIEW virtual instruments employed herein can only generate data files up to a maximum file size of 2 GB. Consequently, the number of samples was limited by this file size constraint (which is nevertheless quite large). In the present work, the simultaneous velocity-temperature data consisted of time series data set of 8.192×10^7 samples (for a total sampling duration of 58 minutes), whereas the individual temperature data sets consisted of 1.2288×10^8 data points, corresponding to a total sampling time of 87 minutes. (These data sets were also used to obtain the various low-order moments of the velocity and passive scalar fields.)

For the lateral dispersion experiments, the moments of the fluctuating velocity and temperature fields were determined using 2.048×10^4 data points recorded at 200 Hz for a total record length of 1.71 minutes. Time series of the fluctuating temperature field were also obtained using 4.096×10^5 data points, sampled at twice the low-pass filter frequency (which varied with wall-normal location in the flow). The PDFs of the temperature fluctuations were computed using 1.6384×10^5 samples recorded at 200 Hz, for a record duration

of 13.7 minutes. (Note that the number of samples for each type of data set was selected such that each statistic was converged. This was confirmed by comparing the statistics computed using fractions of the data set to those obtained using the full record.)

CHAPTER 3

Experimental Conditions and Flow Validation

The following section examines the experimental configurations of both the internal intermittency and lateral dispersion experiments described herein and, more precisely, serves to (i) characterize the hydrodynamic and thermal fields studied herein, and (ii) identify and discuss potential sources of error.

3.1 Internal Intermittency Measurements

The primary objective of this experiment is to examine the influence of the scalar-field boundary conditions on the small-scale statistics of the passive scalar field using the experimental configuration described in section 2.1. Therefore, the passive nature of the scalar (temperature) field must first be verified. Table 4.1 (see section 4.1) reveals that the r.m.s. temperature fluctuation obtained using either scalar-field boundary condition is considerably less than 1°C . Consequently, the change in fluid density associated with such a small temperature change will be negligible, thus providing the first indication of a passive scalar field. To further confirm the passive nature of the temperature field, numerous statistics of the velocity field, including the probability density functions (PDFs) of the velocity fluctuation (figures 3.1a and 3.1b), the sixth-order velocity structure functions (figures 3.1c and 3.1d), and the spectra of turbulent kinetic energy (figures 3.1e and 3.1f) were computed for both the “hot” (i.e. when the scalar source was energized) and “cold” scenarios. Each of these statistics exhibited a collapse when plotted dimensionally (which is a more rigorous test than plotting them non-dimensionally), thereby confirming that the temperature field is indeed passive. As a final note, Berajeklian & Mydlarski (2011) recently presented mixed velocity-temperature statistics

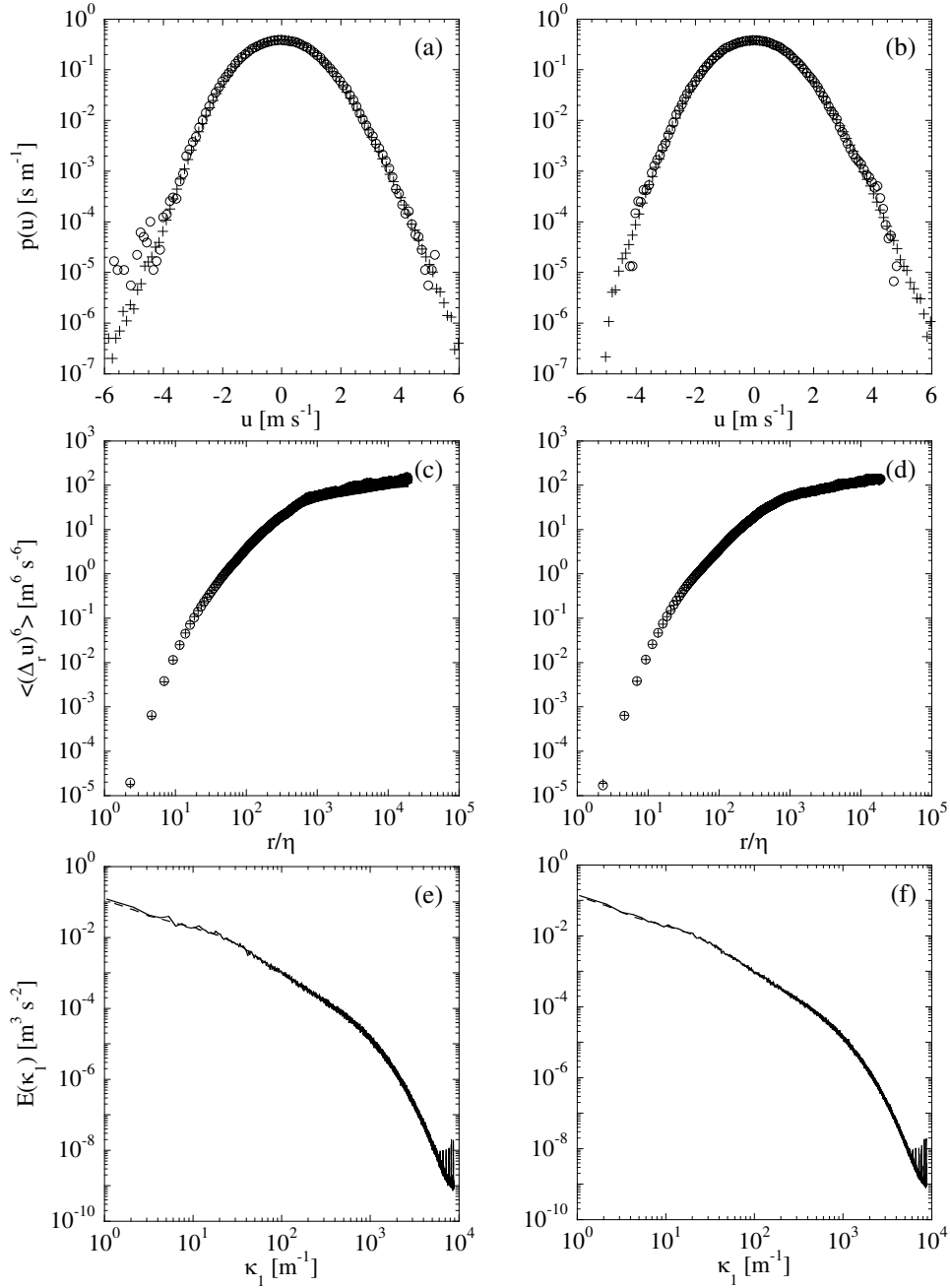


Figure 3.1: Comparison of the PDFs of the velocity fluctuation ($p(u)$), sixth-order velocity structure functions ($\langle\langle\Delta_r u\rangle\rangle^6$) and power spectra of the velocity fluctuations ($E(\kappa_1)$) for both the unheated and heated wakes (for both scalar field boundary conditions). Note that the data are presented dimensionally. (a), (b): PDFs of the velocity fluctuation. (c), (d): Sixth-order velocity structure functions. (e), (f): Power spectra of the velocity fluctuation. (a), (c), (e): Heated cylinder experiment. (b), (d), (f): Mandoline experiment. \circ , Solid line: Unheated wake. $+$, Dashed line: Heated wake.

obtained under similar experimental conditions. They computed the ratio of buoyant production to the dissipation rate of turbulent kinetic energy and noted that this ratio did not exceed 2% — another indication of the passive nature of the scalar field.

Given the objective stated above, it is also of utmost importance that the hydrodynamic flow field remains identical as the scalar injection mechanism is varied. One must therefore determine whether the presence of the mandoline adversely affects the velocity field generated by the cylinder. To this end, one may examine the Reynolds number of the flow past the individual wires of the mandoline to determine whether vortices are being shed from the wire. The former is defined as $Re_{source} \equiv Ud_s/\nu$, where U is a characteristic scale of the flow velocity, d_s is the source diameter (0.127 mm in the present experiment) and ν is the kinematic viscosity evaluated at the film temperature of the fluid:

$$T_{film} \equiv \frac{1}{2}(T_{source} + T_{\infty}) = T_{\infty} + \frac{1}{2}(T_{source} - T_{\infty}),$$

where T_{source} is the surface temperature of the line source, calculated using the convective heat transfer correlation of Zukauskas (1972), and T_{∞} is the free stream (“cold”) fluid temperature. Recently, the use of the film temperature to evaluate the kinematic viscosity of the fluid was studied by Lecordier *et al.* (2000), who alternatively proposed the use of an effective temperature, defined as:

$$T_{eff} \equiv T_{\infty} + (0.24 \pm 0.02)(T_{source} - T_{\infty}).$$

Both will be used in the calculations that follow to evaluate the kinematic viscosity of the air.

As a worst-case estimate, one can assume that the velocity of the flow past the wire is U_{∞} (thus yielding an over-estimate of the wire Reynolds number). Using the heat transfer correlation proposed by Zukauskas (1972), the surface

temperature of the wire, and, therefore, the film temperature of the flow, can be estimated and the kinematic viscosity of the fluid determined. The resulting Reynolds number $Re_{source} = U_{\infty}d_s/\nu$ yields a value of 36 when using properties calculated using the film temperature (the corresponding value obtained using the effective temperature of Lecordier *et al.* (2000) is 52), which is on the order of the critical value of 40 for vortex shedding. Given that the flow exhibits none of the phenomena associated with vortex shedding (i.e. no spikes are present in the velocity spectra — see figure 3.2c), one may conclude that the effects of vortex shedding, if at all present, are small (especially when compared to the effects of the turbulence). Consequently, it can also be concluded that the presence of the mandoline has a negligible influence on the velocity field.

To further support the above conclusion, figure 3.2 also compares the velocity field statistics obtained from both the heated cylinder and mandoline experiments (akin to figure 3.1 above). Consequently, the PDFs of the velocity fluctuation (see figure 3.2a), the sixth-order velocity structure functions (see figure 3.2b) and the power spectra of the velocity fluctuations (see figure 3.2c) were computed when (i) only the cylinder was present in the wind tunnel and (ii) both the cylinder and mandoline were installed in the test section. Upon examining figure 3.2, one observes that the measured PDFs exhibit a collapse over a range of ± 4 standard deviations. In addition, both the high-order structure functions and the power spectra are experimentally indistinguishable (for the entire range of length scales presented herein). This result reinforces the conclusion that the presence of the mandoline has a negligible influence on the velocity field.

Kolmogorov theory applies to flows in which the scalar field is well-mixed (and not “externally intermittent”). Consequently, it is necessary to ensure that the scalar fields generated by the heated cylinder and mandoline are

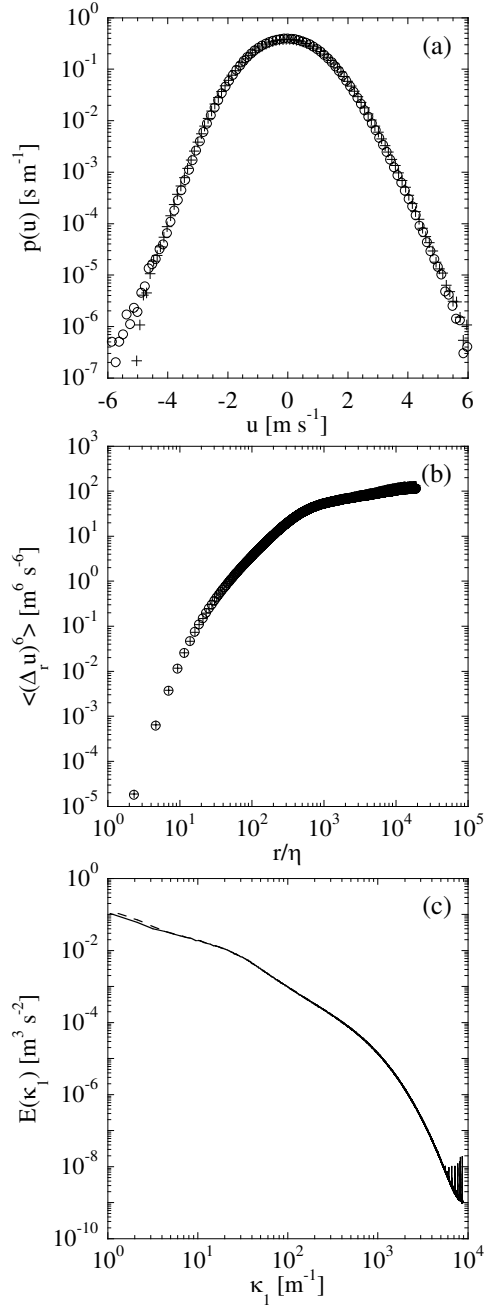


Figure 3.2: Comparison of the PDFs of the velocity fluctuation ($p(u)$), sixth-order velocity structure functions ($\langle\langle\Delta_r u\rangle\rangle^6$) and power spectra of the velocity fluctuations ($E(\kappa_1)$) for the different scalar field boundary conditions. Note that the data are presented dimensionally. (a): PDFs of the velocity fluctuation. (b): Sixth-order velocity structure functions. (c): Power spectra of the velocity fluctuation. \circ , Solid line: Heated cylinder experiment. $+$, Dashed line: Mandoline experiment.

thoroughly mixed. This is accomplished by examining a variety of statistics, including the power spectra of the scalar fluctuations (see figure 3.3a), in addition to the PDFs of the temperature fluctuation (θ) (see figure 3.3b). The measured temperature spectra demonstrate that the scalar fields differ at large scales (due to the different large-scale injection methods), thus also yielding different PDFs, as expected. In contrast to the PDFs of the velocity field, there is no reason to assume that the scalar PDFs will collapse. In fact, given the objectives of the present work, the PDFs of the scalar fields must be different. Furthermore, the measured temperature spectra exhibit a collapse in the inertial-convective- and dissipative-ranges (as predicted by KOC theory), with an inertial-convective scaling region at least one decade in extent. The PDFs of θ are smooth and unimodal, indicating that the wake is indeed well-mixed. (A poorly-mixed wake would exhibit a bimodal PDF, with a second sharp peak arising from unmixed fluid at the ambient temperature of the flow.) Consequently, the collapse of the scalar variance spectra at small scales, in addition to the smooth, unimodal PDFs, supports the conclusion that the thermal wakes of both the heated cylinder and the mandoline are well-mixed.

Computing the high-order moments of both the velocity and scalar fields requires measurement of the rare, intense fluctuations that occur within the flow. This information lies in the tails of the PDF, and thus requires sufficiently long data sets to accurately compute the high-order moments. Consequently, one must also verify that the high-order moments are indeed converged. This is accomplished by analyzing fractions of the data set and comparing the results to those obtained from the full record. In addition to verifying that the statistics are converged, one must also verify that the higher-order moments are indeed closed. Examining the PDFs of the scalar increments ($\Delta_r\theta$), and

noting that:

$$\langle (\Delta_r \theta)^n \rangle \equiv \int_{-\infty}^{\infty} (\Delta_r \theta)^n p(\Delta_r \theta) d(\Delta_r \theta),$$

the tails of the $(\Delta_r \theta)^n p(\Delta_r \theta)$ curve must go to zero as $\Delta_r \theta \rightarrow \pm\infty$ for the integral to close. Given the length of the data sets recorded herein, plots of $(\Delta_r \theta)^8 p(\Delta_r \theta) d(\Delta_r \theta)$ — see figure 3.4 — reveal that the statistics are converged up to order $n = 8$. Anselmet *et al.* (1984) employed a similar technique to determine whether the higher-order moments measured therein were closed. However, they extrapolated the tails of their PDFs to larger values of $\Delta_r u$ (by assuming an exponential form of the PDF of $\Delta_r u$), and therefore extrapolated the integrand, to “artificially” close the high-order moments. Anselmet *et al.* (1984) remarked that the measured value of $\langle (\Delta_r u)^{12} \rangle$ is 30% smaller than the extrapolated value. Moreover, the authors discussed the validity of using such an extrapolation — in particular, they examined whether the PDFs of $\Delta_r u$ will continue to decrease exponentially, or whether $\Delta_r u$ is bounded. Given these concerns, the present work does not employ any techniques that artificially close the higher-order moments.

3.2 Lateral Dispersion Measurements

The following subsection serves two purposes: (i) to characterize the flow field studied in the lateral dispersion experiments, and (ii) to discuss potential sources of error. To this end, it will first summarize issues discussed in the transverse dispersion experiments of Lavertu & Mydlarski (2005), followed by new ones posed by the current work.

To verify that the flow is indeed fully developed, Lavertu (2002) measured the mean and r.m.s. velocity profiles in the transverse direction for two different downstream positions ($x = 7.33$ m and $x = 7.67$ m downstream of the channel entrance) and showed that the profiles collapse (with a maximum difference of 1.7% in the mean and 3.2% in the r.m.s.). Given the objectives of the

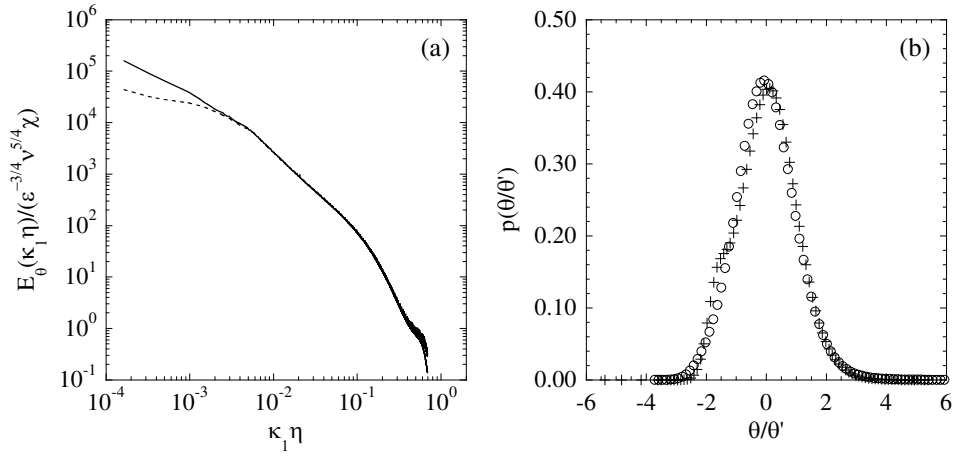


Figure 3.3: Comparison of the (a) power spectrum of the temperature fluctuations, normalized using Kolmogorov variables ($E_\theta(\kappa_1)$), and (b) PDFs of the temperature fluctuation, normalized using the root-mean-square temperature fluctuation ($p(\theta/\theta')$), computed from the heated cylinder and mandoline experiments, which demonstrate that the passive scalar field is indeed well-mixed. In (a): Solid line: Heated cylinder experiment. Dashed line: Mandoline experiment. In (b): \circ : Heated cylinder experiment. $+$: Mandoline experiment.

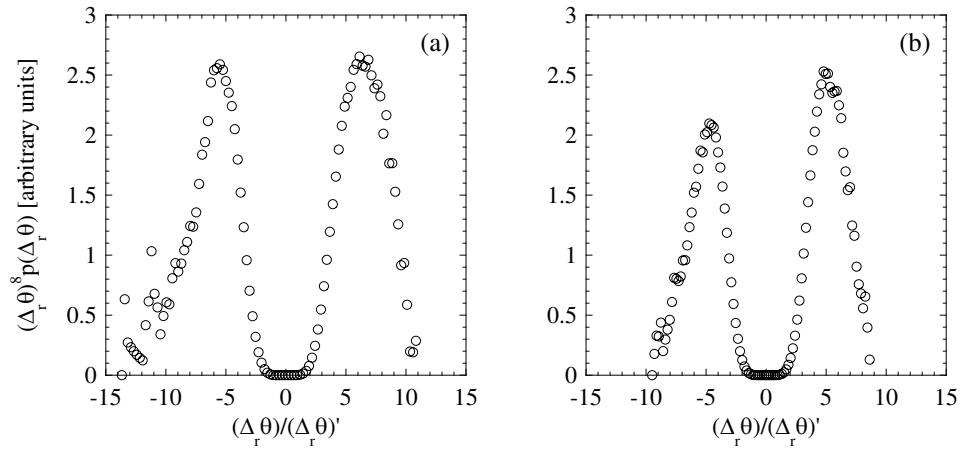


Figure 3.4: Probability density functions for the temperature increment, multiplied by the increment raised to the eighth power (to establish the convergence of the data set at the highest order). The separation corresponds to the midpoint of the inertial-convective range ($r \approx 100\eta$). (a) Heated cylinder experiment. (b) Mandoline experiment.

current work, the flow must be two-dimensional, in addition to being fully developed. Consequently, figure 3.5 presents the mean and r.m.s. velocity profiles obtained at three spanwise heights. One observes that (i) the profiles are symmetric about the channel centreline (i.e. $y/h = 1.0$) and (ii) the profiles for each of the spanwise positions collapse well with an average (maximum) difference of 0.7% (1.4%) in the mean and 1.7% (3.4%) in the r.m.s. Figure 3.6 presents typical one-dimensional velocity spectra (obtained for two wall-normal positions), non-dimensionalized by Kolmogorov variables. As expected, the two curves collapse well at small scales.

Furthermore, one must also verify whether the presence of the line source, as well as the thermal field generated by the source, adversely affects the flow field. As described in section 3.1, the Reynolds number of the flow over the line source is calculated (using fluid properties evaluated at both the film and effective temperature). Given that the source is oriented in the direction of the inhomogeneity of the velocity field, any velocity between zero and that at the centreline may be used in the calculation of the Reynolds number. As a worst-case estimate, one can employ the value at the channel centreline, yielding a source Reynolds number of $Re_{source} = 52$ ($Re_{source} = 66$) using T_{film} (T_{eff}) to estimate the kinematic viscosity of the fluid. Because this value is slightly larger than the critical value of 40, vortex shedding from the source may occur at some locations in the centre of the flow. However, given that the present data exhibit none of the mechanical effects associated with vortex shedding (e.g. no spikes in the spectra), it can be concluded that, if present, the effects of vortex shedding are small and masked by the turbulence.

To confirm the passive nature of the temperature field, (i) the ratio of the rate of production of turbulent kinetic energy by buoyancy to the dissipation rate of turbulent kinetic energy (i.e. $g \langle w\theta \rangle / [\langle T \rangle \epsilon]$) is calculated, as is (ii) the

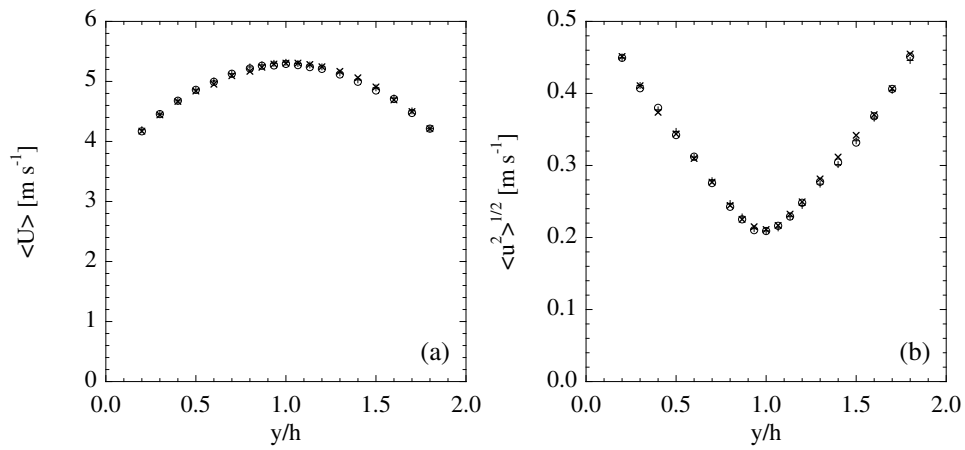


Figure 3.5: Transverse (y) profiles of the longitudinal velocity at three different spanwise positions. (a) Mean velocity profile. (b) Root-mean-square velocity profile. \times : $z/h = -2.0$, \circ : $z/h = 0.0$, $+$: $z/h = 2.0$.

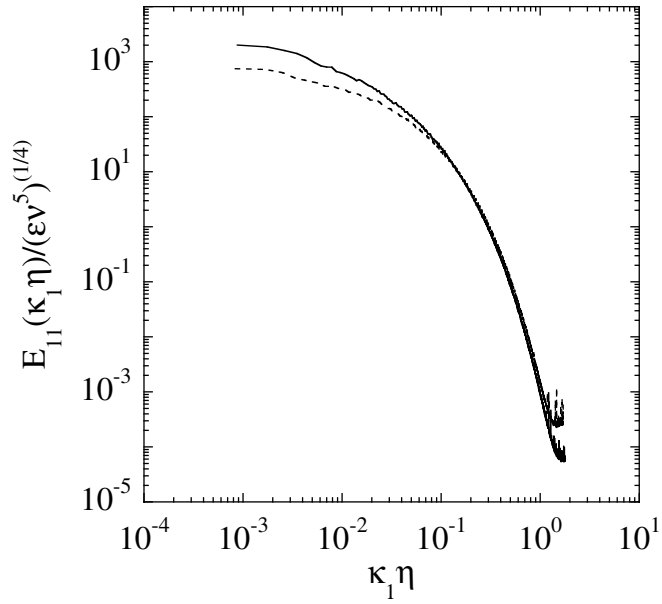


Figure 3.6: One-dimensional longitudinal spectra of the velocity fluctuations at two wall-normal elevations. Solid line: $y/h = 0.10$, Dashed line: $y/h = 1.0$.

ratio of the Grashof number to the Reynolds number squared, Gr/Re_{source}^2 , where the Grashof number is defined as $Gr \equiv g\beta(T_{source} - T_\infty)d_s^3/\nu^2$. Given that velocity–temperature correlations were not measured herein, the correlation coefficient ($\rho_{v\theta}$) measured by Lavertu & Mydlarski (2005) is used to estimate the lateral turbulent heat flux (to obtain an estimate of the production by buoyancy). Assuming that $\langle w\theta \rangle = \rho_{w\theta}w'\theta' \approx \rho_{v\theta}u'\theta'$, one obtains a ratio of roughly 1.3%, thereby confirming that the scalar field is passive since buoyancy effects are small. Moreover, the ratio of the Grashof number to the Reynolds number squared yields a value of $Gr/Re_{source}^2 = 45 \times 10^{-6}$ ($Gr/Re_{source}^2 = 52 \times 10^{-6}$) $\ll 1$ when using the film (effective) temperature to determine the fluid properties. This result further reinforces the previous conclusion that the temperature field is indeed passive. Finally, it was also demonstrated in Lavertu & Mydlarski (2005) that the channel walls could be approximated as being adiabatic.

The most significant experimental difference between the present work and that of Lavertu & Mydlarski (2005) is the orientation of the line source. Given that the source is oriented in the wall-normal direction, six ports were added to each of the two major channel walls to accommodate the line sources. During the course of an experiment, the ports could heat up and thus contaminate the temperature signal from the line source (by the effective superposition of a ground-level source — the inside surface of the port). Consequently, measures were undertaken to minimize this contamination. First, cooling fans were employed outside the channel to minimize any heating of the ports. Second, the line source was turned off between data acquisitions for each point and the background thermal noise was measured (i.e. a “cold” run). This permitted the noise to be subtracted from the signal, as follows. Denoting the temperature fluctuation measured by the cold-wire sensor as θ_M ,

and assuming that it is composed of the sum of the true signal and the noise (such that $\theta_M = \theta_T + \theta_N$), the mean-square temperature fluctuation becomes: $\langle \theta_M^2 \rangle = \langle (\theta_T + \theta_N)^2 \rangle = \langle \theta_T^2 \rangle + \langle \theta_N^2 \rangle + 2 \langle \theta_T \theta_N \rangle$. If the noise and the true temperature signal are uncorrelated (a reasonable assumption), then the final term on the right-hand-side is zero, and one obtains the following expression for the true mean-square temperature: $\langle \theta_T^2 \rangle = \langle \theta_M^2 \rangle - \langle \theta_N^2 \rangle$. The contribution of any heating of the ports to the measured temperature field was negligible, given that the typical difference between the measured and noise-compensated r.m.s. temperature fluctuation was roughly 0.5%. Furthermore, the cold run also permitted the measurement of the free-stream temperature (T_∞), which would be used to determine the mean temperature excess (see figures 4.9 and 4.10 in section 4.2.1).

Finally, errors in the probe positioning are small, owing to the precision of the stepper motor that controls the traversing mechanism. Consequently, relative displacements of the probe are accurate to within 0.01 mm. However, the more relevant source of error is the initial positioning of the probe, which may vary as much as 0.5 mm in the wall-normal and 1 mm in the spanwise direction. Downstream distances are accurate to within 1 mm.

CHAPTER 4

Results

The following chapter presents the data obtained from the (i) internal intermittency (see section 4.1) and (ii) lateral dispersion (see section 4.2) experiments described above in chapter 2. Whereas the former examines the effects of the scalar-field boundary conditions on the small-scale statistics of the passive scalar field, the latter presents data pertaining to the influence of the velocity-field boundary conditions on large-scale mixing phenomena.

4.1 Internal Intermittency Measurements

The following section, which presents the data obtained from the internal intermittency experiment, is divided into three subsections. The first examines different measures of internal intermittency, including results pertaining to the (i) high-order passive scalar structure functions (and their inertial-convective-range scaling exponents, as discussed in Lepore & Mydlarski, 2009), (ii) mixed, sixth-order velocity-temperature structure functions, and (iii) (non-centered) autocorrelations of the dissipation rate of scalar variance. The second discusses the sensitivity of the previous results to the scalar-field boundary conditions (or, more precisely, the finite-Péclet-numbers of the flows under consideration). In this context, the normalized high-order moments of passive scalar increments are of particular interest. The final subsection attempts to compensate the aforementioned normalized high-order moments to obtain further insight into the influence of the large scales of the scalar field. The relevant flow parameters are summarized in table 4.1. (Note that the spatial gradients used to calculate both the dissipation rates of turbulent kinetic energy and scalar variance are obtained by invoking Taylor’s “frozen flow” hypothesis and

Table 4.1: Flow parameters for the internal intermittency experiment. Fluid properties are evaluated at 298 K ($\nu = 15.7 \times 10^{-6} \text{ m}^2 \text{ s}^{-1}$, $\alpha = 22.2 \times 10^{-6} \text{ m}^2 \text{ s}^{-1}$). $D = 73.0 \text{ mm}$ is the cylinder diameter. Note that the experiments described herein were performed at a downstream location of $x/D = 30$ and a transverse position of $y/D = 0$. Please refer to the schematic presented in figure 2.1 for the location and orientation of the coordinate axes.

U_∞ [m s ⁻¹]	10.3	
$Re_D \{\equiv U_\infty D / \nu\}$	47900	
$Re_\lambda \{\equiv u' \lambda / \nu\}$	370	
$\langle U \rangle$ [m s ⁻¹]	8.42	
u' [m s ⁻¹]	1.01	
$\epsilon \{= 15\nu \langle (\partial u / \partial x)^2 \rangle\}$ [m ² s ⁻³]	6.85	
$\ell \{= \int_0^\infty \rho_{uu}(r) dr\}$ [mm]	280	
$\lambda \{= \sqrt{\langle u^2 \rangle / \langle (\partial u / \partial x)^2 \rangle}\}$ [mm]	5.95	
$\eta \{\equiv (\nu^3 / \epsilon)^{1/4}\}$ [mm]	0.154	
$Re \{= u' \ell / \nu\}$	18100	
	Heated Cylinder	Mandoline
θ' [K]	0.195	0.164
$K_\theta \{= \langle \theta^4 \rangle / \langle \theta^2 \rangle^2\}$	3.44	2.86
$SK_\theta \{= \langle \theta^6 \rangle / \langle \theta^2 \rangle^3\}$	26.1	14.1
$HK_\theta \{= \langle \theta^8 \rangle / \langle \theta^2 \rangle^4\}$	422	112
$\chi \{= 3\alpha \langle (\partial \theta / \partial x)^2 \rangle\}$ [K ² s ⁻¹]	0.115	0.119
$\ell_\theta \{= \int_0^\infty \rho_{\theta\theta}(r) dr\}$ [mm]	314	105
$\lambda_\theta \{= \sqrt{\langle \theta^2 \rangle / \langle (\partial \theta / \partial x)^2 \rangle}\}$ [mm]	4.68	3.88
$\eta_\theta \{\equiv (\alpha^3 / \epsilon)^{1/4}\}$ [mm]	0.199	0.199
$Pe \{= u' \ell_\theta / \alpha\}$	14700	4900

assuming local isotropy — see Tennekes & Lumley (1972), pp. 65–67, 95–97, 253.)

4.1.1 Measures of Internal Intermittency

Figure 4.1 plots the even-order structure functions (up to order $n = 8$) of the temperature field, non-dimensionalized using Kolmogorov variables. (To avoid the introduction of any artifices, the structure functions are computed using the raw difference — as opposed to using their absolute value. Hence, the odd-order moments are not presented.) One observes that, at second order, the structure functions obtained using the different heat injection mechanisms are indistinguishable in the inertial-convective and dissipative ranges, consistent with KOC theory. However, as the order increases, one observes that the structure functions begin to deviate at progressively smaller scales — the sixth-order structure functions begin to deviate in the inertial-convective range whereas the eighth-order structure functions are different for a large range of scales. The implication is that the effects of the scalar-field boundary conditions permeate to progressively smaller scales as the structure function order increases (Lepore & Mydlarski, 2009).

Since the current work examines the inertial-convective-range scaling exponents of the high-order passive scalar structure functions, one must objectively determine the extent of the inertial-convective range, so that its scaling can be systematically estimated. The former is accomplished using “Yaglom’s 4/3 law” (Yaglom, 1949), which states that, for large Reynolds and Péclet numbers:

$$\langle (\Delta u) (\Delta \theta)^2 \rangle = -\frac{4}{3} \chi r,$$

in the inertial-convective range. This is analogous to the procedure used in Anselmet *et al.* (1984). Therein, the authors employ Kolmogorov’s 4/5 law,

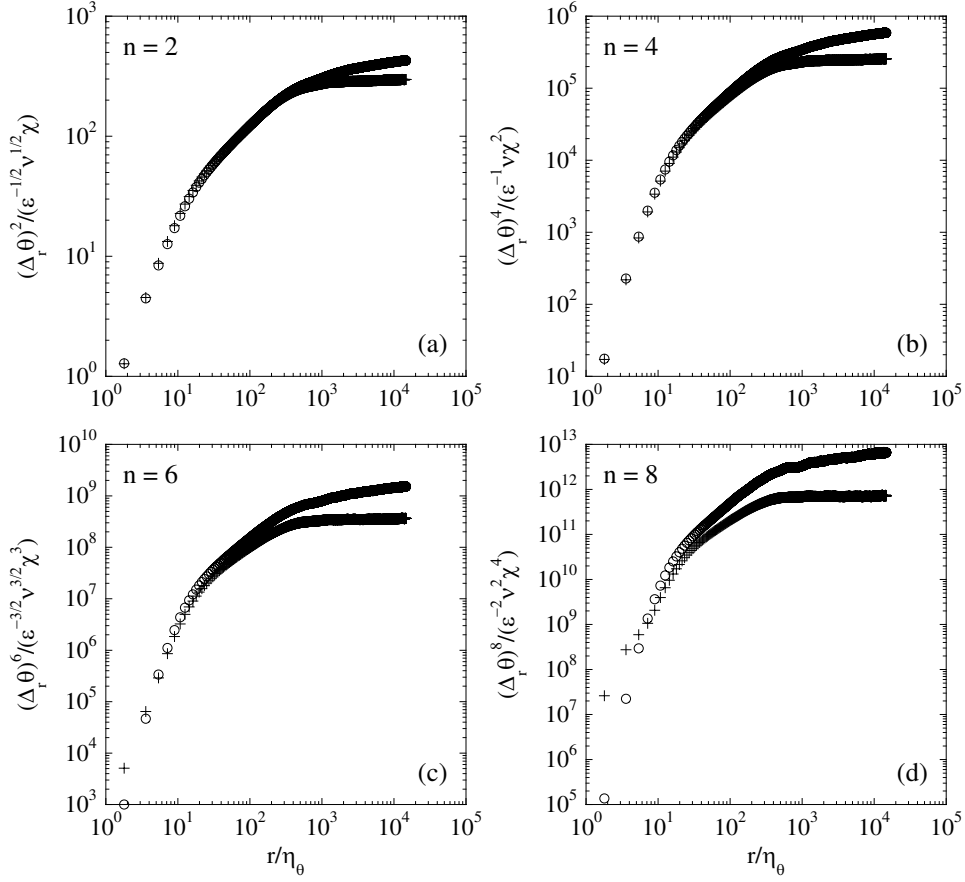


Figure 4.1: The n^{th} -order structure functions of the temperature increment, normalized using Kolmogorov variables. (a) $n = 2$. (b) $n = 4$. (c) $n = 6$. (d) $n = 8$. \circ : Heated cylinder. $+$: Mandoline. Note that the above data also appear in Lepore & Mydlarski (2009).

for which $\langle(\Delta_r u)^3\rangle = -\frac{4}{5}\epsilon r$ in the inertial-range. They argued in favour of using the third-order velocity structure function to determine the extent of the inertial range, given that it is the only structure function in which its inertial range is unaffected by internal intermittency. The same argument holds for the mixed third-order structure function examined herein. The extent of the inertial-convective range is established by determining the two separations at which the compensated mixed third-order structure function falls to 90% of its maximum value, in a manner analogous to that of Jayesh, Tong & Warhaft (1994). Figure 4.2 presents both the second-order structure function of the temperature fluctuations, as well as the mixed third-order structure function, generated using either the heated cylinder or the mandoline. In figure 4.2, the upper and lower bounds of the inertial-convective range, as defined above, are represented by the dashed lines. (Note that the different scalar injection methods yield different inertial-convective ranges.) One observes that this region corresponds to the power-law region exhibited in the second-order temperature structure functions (figures 4.2a and 4.2c), as expected. Consequently, the technique outlined above is employed herein as a consistent method for determining the limits of the inertial range.

Given the difficulties associated with identifying the extent of the inertial-range, Benzi *et al.* (1993) proposed an alternate technique for determining the velocity structure function scaling exponents — see also Benzi *et al.* (1995). By plotting the high-order structure functions versus the third-order structure function (as opposed to the separation, r), Benzi *et al.* (1993) discovered that the inertial-range scaling region was significantly extended, especially in low-Reynolds-number flows — a phenomenon they refer to as Extended Self-Similarity (ESS). However, ESS is not without its limitations. Firstly, ESS

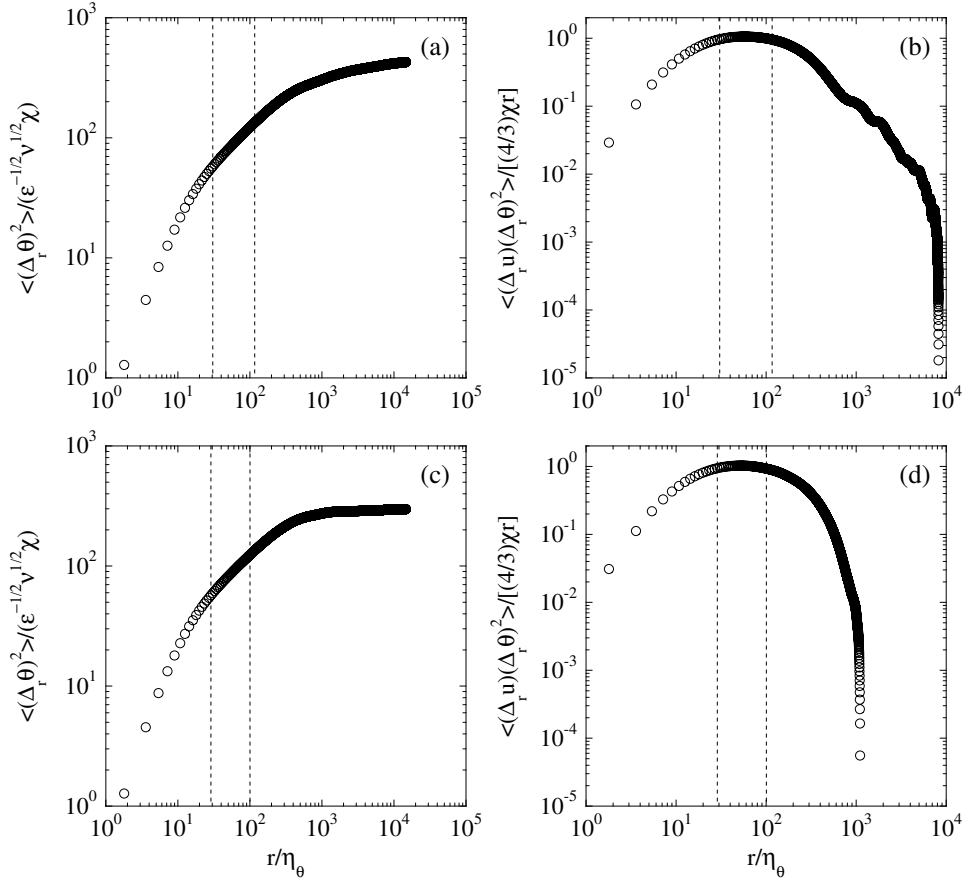


Figure 4.2: The second- and mixed third-order structure functions of the temperature fluctuation, subject to varying scalar-field boundary conditions. (a), (c): Second-order structure function (non-dimensionalized using Kolmogorov variables). (b), (d): Mixed third-order structure function (normalized according to the Yaglom 4/3 law to determine the extent of the inertial-convective range). (a), (b): Heated cylinder. (c), (d): Mandoline. In all figures, the dashed lines denote the upper and lower bounds of the inertial-convective-range scaling region (defined as the separations corresponding to the locations at which the compensated mixed third-order structure function falls to 90% of its maximum value).

yields *relative* scaling exponents, since the structure functions are plotted versus the third-order structure function, which only scales as r in the limit of infinite Reynolds numbers — see, for example, Mydlarski & Warhaft (1996) for the dependence of the third-order structure function on Reynolds number. Furthermore, Stolovitzky & Sreenivasan (1993) discovered that the extended scaling range is *not* observed in higher-order moments. More precisely, the eighth-order moments examined therein exhibited two distinct scaling regions for the dissipative and inertial ranges. Stolovitzky & Sreenivasan (1993) thus concluded that ESS is only valid for the low-order statistics. (Note that Benzi *et al.* (1993) only present structure functions up to the sixth-order.) A similar conclusion regarding ESS was also drawn by Anselmet, Antonia & Danaila (2001), who observed an “inflectional behaviour” in the ESS-compensated data with increasing structure function order, especially at high Reynolds numbers. In addition, Chen & Cao (1997) encountered some difficulty in estimating the errors bars for their ESS-calculated structure function scaling exponents, noting that: “[t]he error bar for the extracted scaling exponents in the inertial range seems bigger than the result using the original structure functions.”

Despite the aforementioned limitations, Ruiz Chavarria, Baudet & Ciliberto (1995) proposed an analogous ESS technique for the passive scalar field. Intuition would suggest plotting the scalar structure functions versus the mixed third-order structure function, $\langle(\Delta_r u)(\Delta_r \theta)^2\rangle$ (given the analogy between Kolmogorov’s 4/5 Law and Yaglom’s 4/3 Law, both of which are proportional to r in the inertial(-convective) range). However, Ruiz Chavarria *et al.* (1995) chose to use the second-order structure function instead. Consequently, one must also determine the second-order scaling exponent to determine higher-order scaling exponents. (Otherwise, one can only compute the relative scaling exponents, ξ_n/ξ_2 .) This complicates the analysis, since one cannot assume that

the second-order structure function will scale as $r^{2/3}$. (As demonstrated in the compilation presented in figure 1.1(b) in the present work, the experimentally-determined values of ξ_2 vary from 0.58–0.66.) That being said, neither can one assume that $\langle(\Delta_r u)(\Delta_r \theta)^2\rangle$ scales as r in the inertial-convective subrange for non-infinite Reynolds and Péclet numbers (Mydlarski & Warhaft, 1998). Furthermore, upon examination of figure 3 of Ruiz Chavarria *et al.* (1995), one clearly observes that this technique does not enhance the inertial-convective scaling region (this is especially true at higher-orders — see their figure 3b). Therefore, given the significant difficulties presented above, the present work does not make use of Extended Self-Similarity to compute the structure function scaling exponents.

The structure function scaling exponents were determined by fitting a least-squares power-law curve fit to the data in the inertial-convective range, defined using the previously-described method. The scaling exponents for the passive scalar field are plotted in figure 1.1(b) (as well as listed in table 4.2). When compared with the results of the other researchers in figure 1.1(b), one observes that they fall within the range of exponents in the published literature. Moreover, the current results for the scalar field generated using the mandoline agree well with the exponents presented in Ruiz-Chavarria *et al.* (1996) (albeit estimated by ESS), whose experimental configuration closely resembled the mandoline experiment studied herein. More importantly, one immediately notices that the passive scalar structure function scaling exponents for the two different scalar field boundary conditions (i) deviate substantially from the KOC $n/3$ theoretical prediction, and (ii) are significantly different from each other at high-orders, thus indicating a dependence of the high-order statistics on the scalar field boundary conditions. (Note that the velocity structure function scaling exponents were also computed using the different scalar-field

Table 4.2: Inertial-range scaling exponents of the structure functions of the velocity (ζ_n) and passive scalar (ξ_n) fields. Note that the values listed in the table below are the averages obtained from multiple experiments. The error bars represent the maximum deviation from the average value observed for the different experiments.

n	ζ_n	ξ_n Heated Cylinder	ξ_n Mandoline
2	0.74	0.63 ± 0.005	0.62 ± 0.005
4	1.35	0.96 ± 0.01	0.93 ± 0.01
6	1.83	1.19 ± 0.01	1.12 ± 0.02
8	2.23	1.39 ± 0.02	1.23 ± 0.03

boundary conditions. At eighth-order, the velocity scaling exponents differed by approximately 1%, which is considerably smaller than the 13% difference observed in the passive scalar exponents, thereby confirming that the observed discrepancy in the passive scalar exponents is not a spurious result of any differences in the velocity fields — see section 3.1.) Given the moderately-high Reynolds number of the flow examined herein, the present results imply a dependence of the small-scale passive scalar field on the large scales. However, Kolmogorov theory is only posed in the limit of infinite Reynolds (and Péclet) numbers. Therefore, the observed discrepancy in the scaling exponents could be an artifact of the non-infinite Reynolds number of the flow. Nevertheless, as concluded in Lepore & Mydlarski (2009), the present work reveals that all previous estimates of the passive scalar structure function scaling exponents (because they are all measured/calculated in finite-Reynolds-number flows) are subject to the scalar field boundary conditions. The question of Reynolds (or, more precisely, Péclet) number dependencies will be addressed in the next subsection.

In comparing the scaling exponents measured herein with the KOC $n/3$ prediction, one observes that the scalar field generated using the mandoline exhibits scaling exponents that are smaller than those measured in the temperature field generated by heating the cylinder. Since the deviation from Kolmogorov theory results from internal intermittency effects, the magnitude of this departure from KOC is frequently used as a measure of the intermittency. Consequently, the scaling exponents presented in table 4.2 imply that the scalar field generated by the mandoline is more intermittent than that generated by the heated cylinder. Furthermore, the current results demonstrate that the passive scalar structure function scaling exponents are sensitive to the large-scale features of the flow — i.e. the scalar-field boundary conditions.

It is therefore of interest to determine if alternate statistics can be used to provide insight into the small-scale structure of the passive scalar field.

To this end, the (i) sixth-order, mixed (velocity-temperature) structure functions, $\langle(\Delta_r u)^2(\Delta_r \theta)^4\rangle$, and (ii) (non-centered) autocorrelations of the dissipation rate of scalar variance, $\rho_{\chi\chi}(r) \equiv \langle\chi(x)\chi(x+r)\rangle / \langle\chi^2\rangle$, were also obtained for each of the two flows — see figures 4.3 and 4.4, respectively. In the inertial-convective scaling range, the former scales as $r^{2-\mu_\theta}$, whereas the latter scales as $r^{-\mu_\theta}$, where μ_θ is the scalar intermittency exponent and can be used to quantify the degree of internal intermittency – see for example Antonia *et al.* (1984) or Warhaft (2000). Consequently, these additional statistics can also be used to obtain quantitative estimates of the internal intermittency of the passive scalar fields examined herein.

Figure 4.3 reveals that the scalings of the sixth-order, mixed velocity-temperature structure functions for the scalar fields generated by the heated cylinder and the mandoline are quite similar — much more so than the analogous plots of the sixth-order passive-scalar structure function (see figure 4.1c). This similarity is quantitatively confirmed by the inertial-convective-range scaling exponents for these two figures (measured in the same manner as for the passive scalar structure functions), which are 1.638 and 1.644 for the heated cylinder and mandoline experiments, respectively.

To place these exponents in the context of previous research, note that Chambers & Antonia (1984) measured (by means of structure function compensation) the scaling exponents of $\langle(\Delta_r u)^2(\Delta_r \theta)^4\rangle$ to be 1.75 ± 0.05 in the atmospheric surface layer, whereas Schmitt *et al.* (1996) obtained 1.65 ± 0.05 (also in the atmospheric surface layer) using least-squares regression in the inertial range. In the wake of a heated cylinder, L  v  que *et al.* (1999) obtained

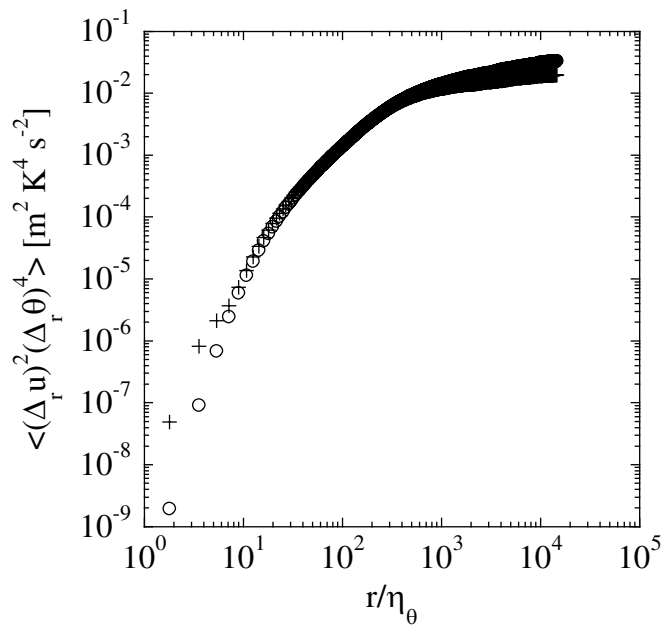


Figure 4.3: The mixed, sixth-order structure function, $\langle (\Delta_r u)^2 (\Delta_r \theta)^4 \rangle$, plotted as a function of the non-dimensional separation, obtained using the different scalar-field boundary conditions. \circ : Heated cylinder experiment. $+$: Mandoline experiment.

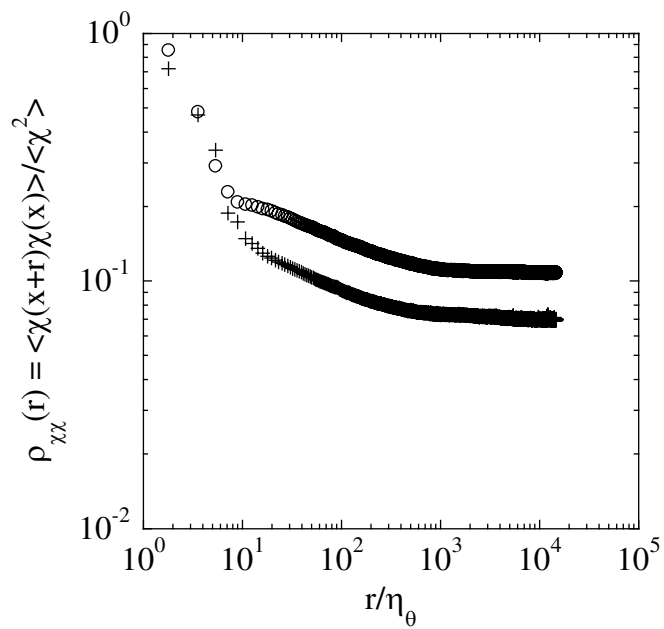


Figure 4.4: The non-centered autocorrelation of the dissipation rate of scalar variance, $\rho_{\chi\chi}(r)$, plotted as a function of the non-dimensional separation, obtained using the different scalar-field boundary conditions. \circ : Heated cylinder experiment. $+$: Mandoline experiment.

a scaling exponent of 1.608 ± 0.028 using Extended Self-Similarity. Xu, Antonia & Rajagopalan (2000) measured, by least-squares regression, the scaling exponent to be 1.83 in a turbulent round jet. At the highest Reynolds number in active-grid turbulence, Mydlarski (2003) measured the scaling exponent to be 1.52 ± 0.05 (by means of structure function compensation) and 1.58 (using ESS). Boratav & Pelz (1998) estimated the scaling exponents in their DNS of homogeneous, isotropic turbulence by means of ESS and found them to be 1.61 ± 0.04 . Consequently, the current results fall within the range of the values observed in the literature. Moreover, the current measurements imply that the estimates of μ_θ for both scalar fields are approximately 0.36. This result is especially consistent with the results of both Sreenivasan, Antonia & Danh (1977) and Prasad, Meneveau & Sreenivasan (1988), who estimate $\mu_\theta \approx 0.35$ and 0.38, respectively. Chambers & Antonia (1984) found $\mu_\theta = 0.25 \pm 0.05$, whereas Mydlarski & Warhaft (1998) found $0.19 \leq \mu_\theta \leq 0.28$ over a range of Reynolds numbers. In the context of the present work, the precise value of μ_θ is not as important as the fact that both estimates of μ_θ are effectively identical for the two different scalar fields. (It has been demonstrated that the different approaches used to calculate the intermittency exponents can result in different estimates – see Sreenivasan & Kailasnath (1993) and Mydlarski (2003).)

Alternately, μ_θ is found to be 0.172 and 0.176 for the scalar fields generated by the heated cylinder and mandoline, respectively, when calculated from the (non-centered) autocorrelations of the dissipation rates of scalar variance, $\rho_{\chi\chi}(r)$ — see figure 4.4.¹ Once again, both values are effectively identical, thus

¹ The reason that the two autocorrelations have different (non-zero), large-scale asymptotes is that these are non-centered autocorrelations (as opposed to centered ones), with different (scalar) dissipation statistics. As was shown in

implying that the passive scalar fields generated by both the heated cylinder and the mandoline exhibit similar levels of internal intermittency.

Lastly, it is noted that, by use of an intermittency model, μ_θ can also be inferred from the measured values of ξ_n . The model of Cao & Chen (1997) was used herein to estimate the intermittency exponents by applying a least-squares curve fit to the scaling exponent data presented in table 4.2. (Note that the model assumes that the intermittency exponent for the velocity field, μ , which is the same for both flows, is $\mu = 2/9 = 0.22$.) The resulting inferred scalar intermittency exponents were $\mu_\theta = 0.246$ and 0.288 for the heated cylinder and mandoline experiments, respectively. These estimates differ by 17% — at least one order of magnitude larger than the difference obtained when comparing the intermittency exponents computed from the mixed sixth-order structure functions and the autocorrelations of χ . Consequently, this result reinforces the significance of the perceived difference in internal intermittency when using higher-order passive scalar structure function exponents as a measure, given that the values of μ_θ (and therefore the degrees of passive scalar internal intermittency) determined from both the sixth-order, mixed velocity-temperature structure functions and the autocorrelations of χ can be considered to be experimentally indistinguishable.

4.1.2 Finite-Péclet-Number Effects

In addition to the statistics described above, it is useful to consider the higher-order moments of the passive scalar increments (as a function of the separation, r), normalized by the second-order structure function. Normalized

Mydlarski & Warhaft (1996) (p.363), an equation can be derived which gives the value of the asymptote as a function of the square of the mean dissipation and the variance of the dissipation.

fourth-, sixth- and eighth-order passive scalar structure functions are presented in figures 4.5(a)–(c). (These will be referred to herein as the kurtosis, super-kurtosis and hyper-kurtosis structure functions, respectively.) One observes that, at large scales, the curves roughly asymptote to their respective Gaussian values (3, 15 and 105). More precisely, the heated cylinder data appear to asymptote to a value that is slightly larger than the analogous value for the mandoline experiment. This result is not unreasonable since the kurtosis of the scalar fluctuations (i.e. K_θ) is larger for the heated cylinder experiment — see table 4.1. (One can easily demonstrate that, in the limit of $r \rightarrow \infty$, $K_{\Delta, \theta} \rightarrow K_\theta$.) At small scales, one notices significant departures from the Gaussian prediction, due to the effects of internal intermittency. Significantly, one also observes that, for all three subfigures, the mandoline data achieves its Gaussian value at smaller scales than do the heated cylinder data. For example, the mandoline data clearly attain their large-scale value (~ 15) for the super-kurtosis (i.e. figure 4.5b) at roughly $r/\eta_\theta \approx 10^3$, whereas the heated cylinder data only do so towards the end of the recorded data ($r/\eta_\theta \approx 10^4$), or even beyond that. This occurs because the thermal integral length scale for the mandoline experiment is smaller than the corresponding value for the heated cylinder experiment. (Table 4.1 indicates that $\ell_\theta = 105$ mm and 314 mm for the mandoline and heated cylinder experiments, respectively.) This effect spuriously steepens the inertial-convective-range slope of the mandoline super-kurtosis structure function (making it more negative, due to the smaller scalar integral length scale / smaller Péclet number) relative to that of the heated cylinder experiment because it must fall from its small-scale value (at $r \rightarrow 0$)

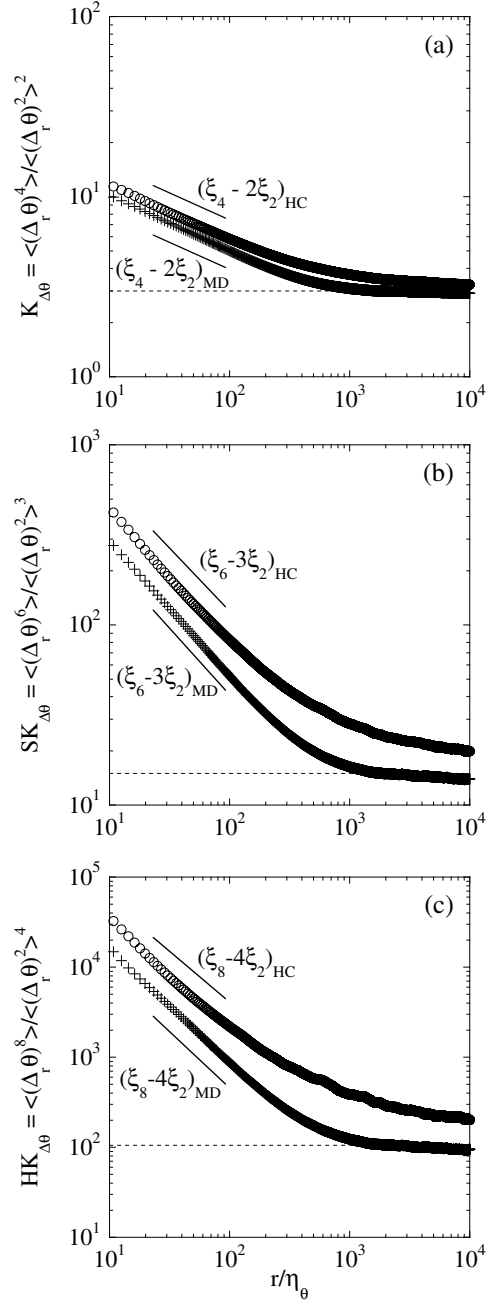


Figure 4.5: The high-order moments of the passive scalar increments, $\langle (\Delta_r \theta)^n \rangle / \langle (\Delta_r \theta)^2 \rangle^{n/2}$, plotted as a function of the separation (r/η_θ). (a) Kurtosis ($n = 4$). (b) Super-kurtosis ($n = 6$). (c) Hyper-kurtosis ($n = 8$). \circ : Heated cylinder experiment. $+$: Mandoline experiment. The dashed line corresponds to the Gaussian prediction.

to its large-scale value (at $r \approx \ell_\theta$) over a smaller range of scales.² Moreover, the inertial-convective-range scaling exponents of the normalized higher-order moments of the passive scalar increments (denoted by γ_n) can be related to the structure function scaling exponents (ξ_n) as follows:

$$\gamma_n \equiv \xi_n - \left(\frac{n}{2}\right) \xi_2,$$

because, in the inertial-convective range:

$$\langle (\Delta_r \theta)^n \rangle / \langle (\Delta_r \theta)^2 \rangle^{n/2} \propto r^{\gamma_n} = r^{\xi_n} / (r^{\xi_2})^{n/2} = r^{\xi_n - (n/2)\xi_2}.$$

As demonstrated in table 4.2, the second-order structure function scaling exponents are experimentally indistinguishable for the heated cylinder and mandoline experiments. Consequently, the slopes of the normalized high-order moments (γ_n) are directly related to the inertial-convective range scaling exponents of the passive scalar structure functions of the same order (ξ_n). Since it has already demonstrated that γ_n for the mandoline is smaller than that of the heated cylinder (due to the smaller thermal integral length scale/narrower inertial-convective range), one may therefore conclude that the structure function scaling exponents (ξ_n) for the scalar field generated by the mandoline are smaller than the corresponding values for the heated cylinder for the same

² Note that one might be tempted to extrapolate this argument to conclude that the scaling exponents, ξ_n , will tend to increase with Reynolds / Péclet number, and potentially asymptote to $n/3$. However, such an argument is incorrect because it neglects to include the fact that intermittency effects also increase with Reynolds number, as does the width of the inertial-convective range. For example, the kurtosis of $\partial u / \partial x$, or equivalently $\partial \theta / \partial x$, increases with Reynolds / Péclet number (e.g. Sreenivasan & Antonia, 1997). Such an argument is akin to stating that the (fourth-order) kurtosis structure functions asymptote to 3 at all scales as $Re \rightarrow \infty$. However, the tendency for this to occur (due to the increase in extent of the scaling range) is offset by the increase in $K_{\partial \theta / \partial x}$ with Reynolds number.

reason, and are not uniquely the result of a more intermittent passive scalar field.

The dependence of the scaling exponents (either ξ_n or γ_n) on ℓ_θ (and, therefore, on the width of the inertial-convective range, since the two scalar fields have identical Corrsin microscales of length, η_θ — see table 4.1) is, in effect, a Péclet number dependence. Recall that the Péclet number should be defined as $Pe = u'\ell_\theta/\alpha$, since the integral scale of the scalar field, ℓ_θ , is different from that of the velocity field, ℓ . Therefore, it is incorrect to simply write $Pe = Re \times Pr$, where Pr is the Prandtl number of the fluid, since such an (overly simple) expression for the Péclet number would yield the same value for both scalar fields, which is not the case herein, given that both scalar fields have different integral length scales.

To account for this Péclet-number dependence, one may normalize the data in figure 4.5 in a manner that compensates for this effect. More precisely, the spatial separation r is non-dimensionalized using the integral length scale of the passive scalar field: $[(r/2\pi) - \eta_\theta]/[\ell_\theta - \eta_\theta]$ (as opposed to the r/η_θ normalization employed in figure 4.5). Using this non-dimensionalization, the data of figure 4.5 are re-plotted in figure 4.6, where it should be noted that the abscissa asymptotes to 0 as $r \rightarrow 2\pi\eta_\theta$ and to 1 as $r \rightarrow 2\pi\ell_\theta$. One immediately observes that the collapse of the kurtosis structure function data measured using different scalar-field boundary conditions improves significantly. (This normalization does not collapse the large-scale statistics, which will be expounded upon shortly.) This result *may* suggest that, when appropriately compensated for their different Péclet numbers, the scaling exponents of the two scalar fields are significantly less different. That being said, such a renormalization renders the estimation of scaling exponents more difficult, since

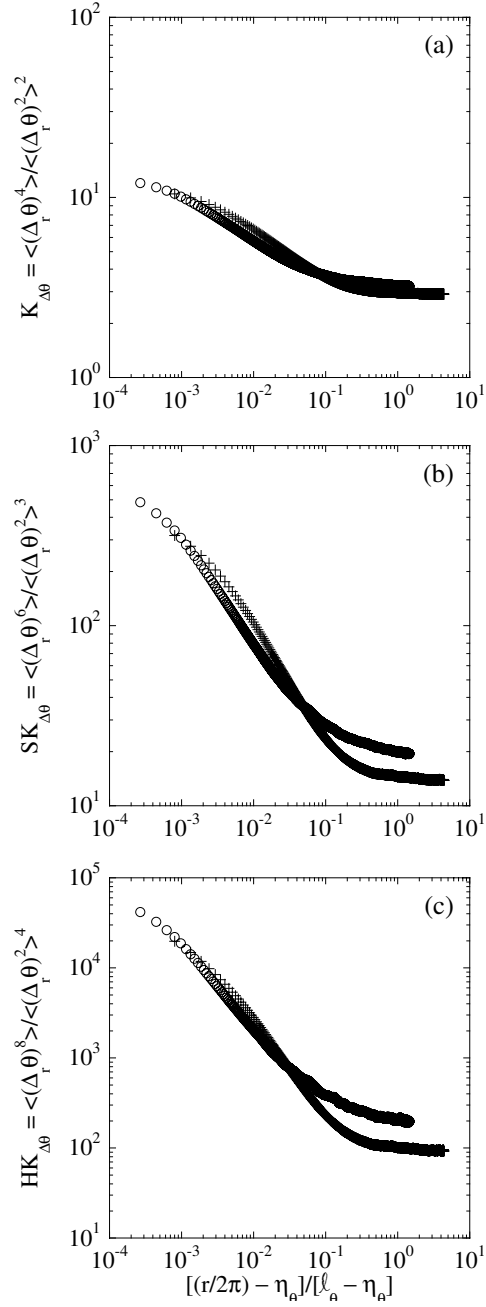


Figure 4.6: The kurtosis structure functions, $\langle (\Delta_r \theta)^n \rangle / \langle (\Delta_r \theta)^2 \rangle^{n/2}$, plotted as a function of the Péclet-number-compensated separation $[(r/2\pi) - \eta_\theta] / [\ell_\theta - \eta_\theta]$. (a) Kurtosis ($n = 4$). (b) Super-kurtosis ($n = 6$). (c) Hyper-kurtosis ($n = 8$). \circ : Heated cylinder experiment. $+$: Mandoline experiment.

well-defined power-law scaling regions are no longer observed. More importantly, however, this result supports the previous conclusion that the observed difference in the passive scalar structure function scaling exponents is related to the different Péclet numbers of the two scalar fields (i.e. the difference in their scalar integral length scales), and is not solely (if at all) a reflection of the relative levels of internal intermittency of the two passive scalar fields.

Like the passive scalar structure functions, the mixed, sixth-order structure functions presented in figure 4.3 can also be normalized using the variance of the fluctuating velocity and passive scalar fields as follows:

$$\langle (\Delta_r u)^2 (\Delta_r \theta)^4 \rangle / (\langle (\Delta_r u)^2 \rangle \langle (\Delta_r \theta)^2 \rangle^2).$$

They then become “mixed sixth-order super-kurtosis structure functions,” which are presented in figure 4.7. Plotted in this manner, the mixed super-kurtosis structure functions for the different scalar fields achieve their respective asymptotic large-scale values at similar separations (which, as demonstrated in figure 4.5, was clearly not the case for the analogous passive scalar kurtosis structure functions). The fact that such mixed velocity-temperature structure functions are less dependent on their respective values of ℓ_θ (which are different for both flows) is consistent with the (grid-turbulence) results of Mydlarski (2003), who noted that mixed velocity-passive scalar (co-spectra and) structure functions resembled more closely those of the velocity field than those of the scalar field. This suggests that the reason the scaling exponents determined from the mixed velocity-passive scalar structure functions are similar and, therefore, not as Péclet-number-dependent is because these statistics are dominated by the velocity field and, therefore, not as contaminated by the different large scales of the scalar field. (Recall that ℓ is the same for both flows.)

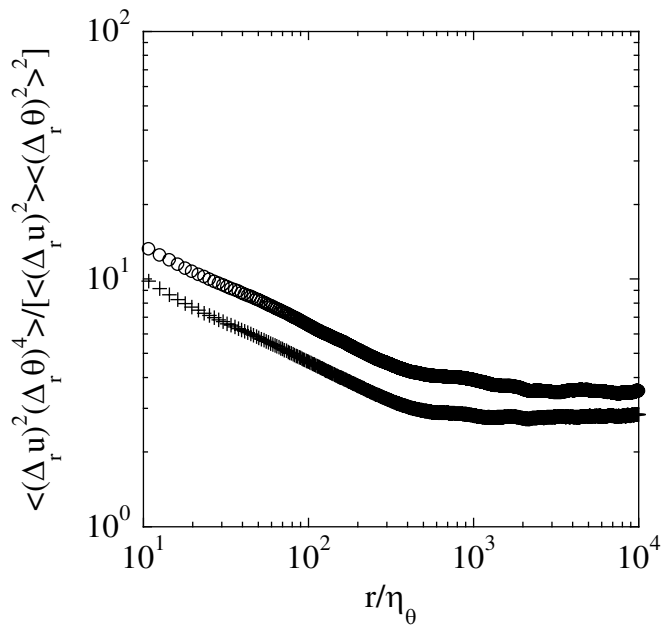


Figure 4.7: The mixed (i.e. velocity-temperature) “super-kurtosis” (i.e. sixth-order) structure function, $\langle (\Delta_r u)^2 (\Delta_r \theta)^4 \rangle / (\langle (\Delta_r u)^2 \rangle \langle (\Delta_r \theta)^2 \rangle^2)$, plotted as a function of the separation, for the scalar fields generated by the heated cylinder and mandoline. \circ : Heated cylinder experiment. $+$: Mandoline experiment.

The autocorrelations of the dissipation rate of scalar variance, $\rho_{\chi\chi}(r)$, presented in figure 4.4, also exhibit a similar independence of the scalar-field boundary conditions. Since this statistic is an autocorrelation of a small-scale quantity (i.e. the dissipation rate of scalar variance), it is reasonable to expect that such a quantity would be less sensitive to the large-scale anisotropies of the temperature field.

It has been shown that the most commonly measured estimators of (passive scalar) internal intermittency — i.e. the high-order passive scalar structure function exponents — are Péclet number dependent, whereas measures of intermittency derived from either (i) autocorrelations of the scalar dissipation rate, or (ii) the mixed sixth-order structure functions appear to be effectively independent of Péclet number. Consequently, the dependence of different measures of intermittency on the Péclet number / boundary conditions is (i) of particular interest to any future work on this subject, and especially pertinent to any conclusions drawn pertaining to the degree(s) of universality of passive scalar fields, and (ii) possibly indicative of further differences between the hydrodynamic and scalar fields — differences which remain intriguing and not fully explained. Lastly, the question of which, if any, of the measures of internal intermittency studied herein is best and/or correct, remains open.

4.1.3 Compensation of Kurtosis Structure Functions

We return to the previous observation that the large-scale heated cylinder statistics in figure 4.5 asymptote to constant values that are slightly larger than the analogous values for the mandoline statistics. Consequently, it is of interest to examine the effect of the large-scale asymptote of the kurtosis structure function (referred to as K_∞ herein) on the small-scale statistics (namely $K_{\Delta_r,\theta}$). To this end, the following two compensation techniques are proposed. Figure 4.8 plots the kurtosis structure functions, $K_{\Delta_r,\theta}$, both offset

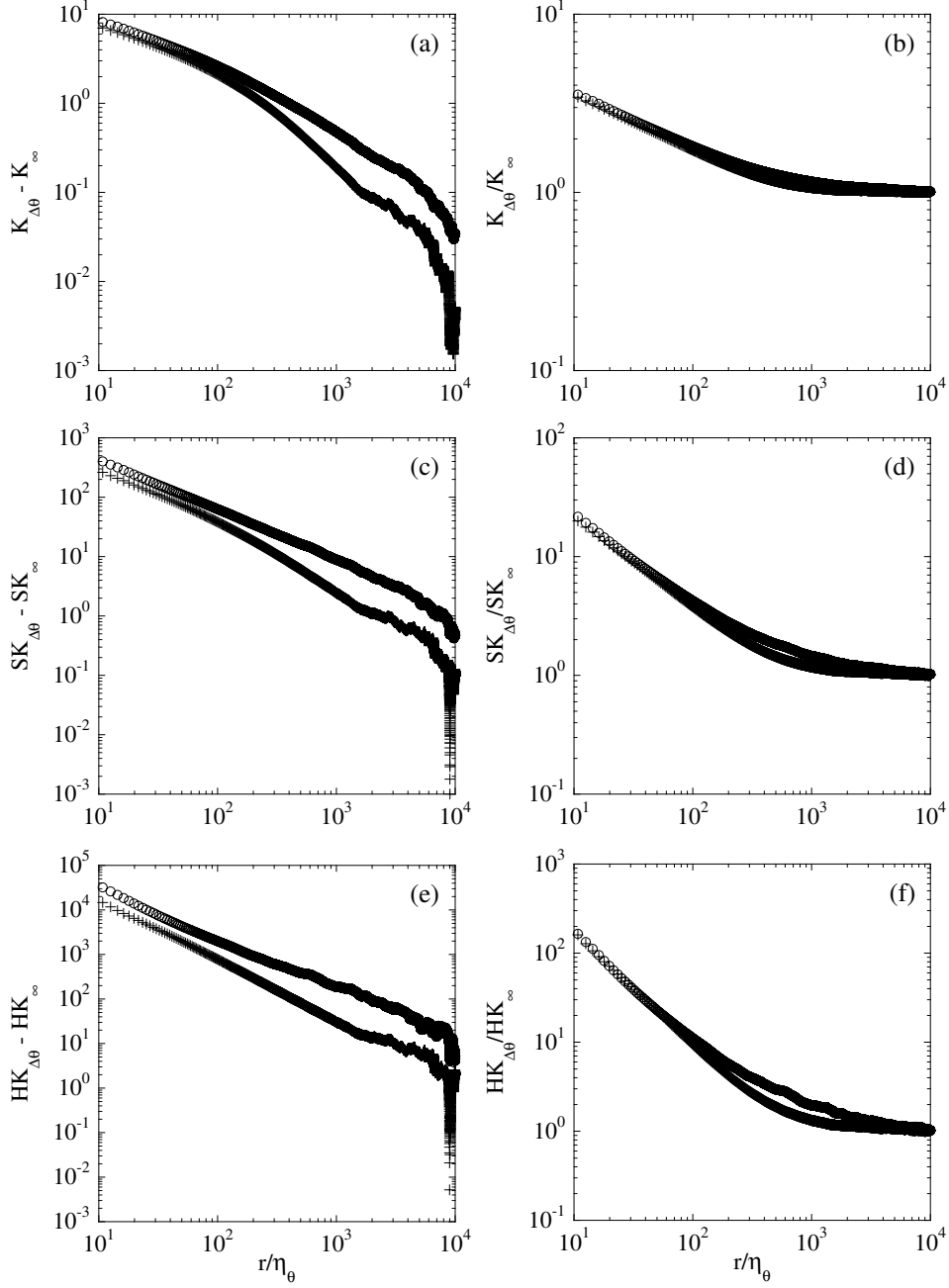


Figure 4.8: The offset and normalized kurtosis structure functions of the passive scalar increment ($K_{\Delta r, \theta} - K_\infty$ and $K_{\Delta r, \theta}/K_\infty$, respectively) plotted as a function of the separation (r/η_θ). (a), (c), (e): Offset kurtosis structure functions. (b), (d), (f): Normalized kurtosis structure functions. (a), (b): Kurtosis ($n = 4$). (c), (d): Super-kurtosis ($n = 6$). (e), (f): Hyper-kurtosis ($n = 8$). \circ : Heated cylinder experiment. $+$: Mandoline experiment.

(by subtraction), and normalized (by division) by their respective large-scale, asymptotic values (i.e. K_∞) — see figures 4.8(a)(c)(e) and 4.8(b)(d)(f), respectively. (As previously mentioned, $K_{\Delta,r,\theta}$ will approach K_θ , the kurtosis of the fluctuating scalar field, in the limit of $r \rightarrow \infty$. In the present work, ℓ_θ for the mandoline experiment is sufficiently small so that $K_\theta \approx K_\infty$, which is not the case for the heated cylinder experiment.) While there is no a priori reason to argue in favour of either technique, it must be noted that offsetting ($K_{\Delta,r,\theta} - K_\infty$) preserves the interpretation of the kurtosis (since it represents a shift in the ordinate), whereas normalization ($K_{\Delta,r,\theta}/K_\infty$) does not. (The interpretation of such a normalization is discussed below.) The offset kurtosis structure functions ($K_{\Delta,r,\theta} - K_\infty$) presented in figures 4.8(a)(c)(e) reveal that the data obtained from the heated cylinder experiment exhibit a larger deviation from their asymptotic values than the analogous results from the mandoline experiment. Unfortunately, no conclusions pertaining to the intensity of the internal intermittency can be drawn from these data, since the magnitude of the kurtosis structure alone may depend upon flow-dependent, large-scale parameters.

Regarding the normalized kurtosis structure functions (i.e. $K_{\Delta,r,\theta}/K_\infty$), one observes that, as required, the data asymptote to unity at large scales. Interestingly, one also observes a collapse of the data at small scales. However, the heated cylinder and mandoline statistics diverge at intermediate scales, with the magnitude of the divergence increasing with structure function order (and with the heated cylinder taking on larger values). While the current normalization successfully reconciles the small-scale statistics of the two different scalar fields, one must note that, as previously stated, the data normalized in this fashion are no longer physically representative of the kurtosis of the passive scalar field. Lastly, note that the data, when plotted as $K_{\Delta,r,\theta}/K_\theta$ (not

shown) collapse over a smaller extent, but nevertheless also exhibit increasing divergence as the structure function order increases.

The divergence of the data in figures 4.8(b)(d)(f) at intermediate scales merits further discussion. To this end, note that Schumacher, Sreenivasan & Yeung (2003) used nearby even-order moments to non-dimensionalize the odd-order statistics of the velocity gradient — e.g. $\langle x^5 \rangle / \langle x^4 \rangle^{5/4}$, $\langle x^5 \rangle / \langle x^6 \rangle^{5/6}$ and $\langle x^5 \rangle / [\langle x^4 \rangle \langle x^6 \rangle]^{1/2}$, where x is the velocity gradient, $\partial u / \partial y$ — since normalization using the variance may not be valid in intermittent (i.e. non-Gaussian) phenomena. Warhaft & Gylfason (2004) examined various high-order statistics of the passive scalar increments in homogenous, isotropic turbulence using the different non-dimensionalizations presented in Schumacher *et al.* (2003) to compensate for the effects of internal intermittency. Warhaft & Gylfason (2004) concluded that, while the normalizations proposed by Schumacher *et al.* (2003) were successful in compensating the low-order statistics, they simply delayed the effects of internal intermittency to higher-order statistics. Reasoning along these lines, combined with the observation that the magnitude of the difference between the heated cylinder and mandoline statistics at intermediate scales increases with the kurtosis structure function order, leads to the conclusion that this difference will eventually permeate to the small-scales at higher orders. Consequently, although the present normalization successfully collapses the small-scale data (particularly at low orders), the normalization employed in figures 4.8(b)(d)(f) delays the onset of the effects of internal intermittency to even-higher order statistics, consistent with the results of Warhaft & Gylfason (2004).

4.2 Lateral Dispersion Measurements

The results of the lateral dispersion experiment are subdivided into the following sections: measurements of the mean temperature field (section 4.2.1),

fluctuating temperature field (section 4.2.2) and temperature PDFs (section 4.2.3). Given that one objective of the present work is to compare and contrast the current lateral dispersion with the transverse dispersion studied in Lavertu & Mydlarski (2005), the flow parameters and measurement locations examined in the current study were selected to match those of Lavertu & Mydlarski (2005). Consequently, the experiments described herein were conducted at a Reynolds number of $Re = 10200$ ($Re_\tau = 502$) at six downstream locations (i.e. $x/h = 4.0, 7.4, 10.8, 15.2, 18.6$ and 22.0) and six wall-normal positions (i.e. $y/h = 0.10, 0.17, 0.33, 0.50, 0.67$ and 1.0) with a horizontal line source located at the mid-height of the channel. The relevant flow parameters are summarized in table 4.3. (Note that, as before, the spatial gradients used to calculate the dissipation rate of turbulent kinetic energy are obtained by invoking Taylor's hypothesis and assuming local isotropy.)

Table 4.3: Flow parameters for the lateral dispersion experiment. Fluid properties are evaluated at 295 K ($\rho = 1.18 \text{ kg m}^{-3}$, $c_P = 1007 \text{ J kg}^{-1} \text{ K}^{-1}$, $\nu = 15.5 \times 10^{-6} \text{ m}^2 \text{ s}^{-1}$). $h = 0.030 \text{ m}$ is the channel half-width. $d_s = 0.254 \text{ mm}$ is the source diameter. $P' = 76 \text{ W m}^{-1}$ is the power input to the source per unit length. $\rho_{uu}(r)$ is the autocorrelation function of the longitudinal velocity fluctuation, defined as $\rho_{uu}(r) \equiv \langle u(x+r)u(x) \rangle / \langle u^2 \rangle$.

	y/h					
	0.10	0.17	0.33	0.50	0.67	1.0
$u_* \text{ [m s}^{-1}\text{]}$	0.258					
$Re\{\langle U \rangle_{y/h=1.0} h/\nu\}$	10200					
$Re_\tau\{= u_* h/\nu\}$	502					
$\langle U \rangle \text{ [m s}^{-1}\text{]}$	3.73	4.05	4.52	4.83	5.04	5.24
$\langle u^2 \rangle^{1/2} \text{ [m s}^{-1}\text{]}$	0.536	0.463	0.397	0.340	0.284	0.208
$\Delta T_r\{= P'/\rho c_P d_s \langle U \rangle\} \text{ [K]}$	67.4	62.1	55.7	52.2	49.9	48.1
$\epsilon\{= 15\nu \langle (\partial u/\partial x)^2 \rangle\} \text{ [m}^2 \text{ s}^{-3}\text{]}$	7.66	5.20	2.52	1.46	0.912	0.548
$\ell\{= \int_0^\infty \rho_{uu}(r) dr\} \text{ [mm]}$	14.6	16.4	19.7	20.6	21.0	18.5
$\lambda\{= \sqrt{\langle u^2 \rangle / \langle (\partial u/\partial x)^2 \rangle}\} \text{ [mm]}$	2.95	3.09	3.80	4.29	4.53	4.27
$\eta\{= (\nu^3/\epsilon)^{1/4}\} \text{ [mm]}$	0.15	0.16	0.20	0.22	0.25	0.29
$Re_\lambda\{= \langle u^2 \rangle^{1/2} \lambda/\nu\}$	102	93	98	94	83	57
	50	84	167	251	335	502
	$y^+\{ \equiv yu_*/\nu \}$					

4.2.1 The mean temperature field

The downstream and transverse evolutions of the spanwise mean temperature excess ($\Delta T = \langle T \rangle - T_\infty$) profiles, non-dimensionalized by their peak (i.e. centreline) value (ΔT_c), are presented in figures 4.9 and 4.10, respectively. For all combinations of downstream positions and transverse distances examined herein, the profiles are described well by Gaussian distributions. Furthermore, the profiles remain symmetric with peaks that are located downstream of the source location. (Displacement of the peaks would not be expected, given the symmetry of the flow in the lateral direction.) Fackrell & Robins (1982) also measured lateral mean concentration profiles that were well approximated by Gaussian profiles in their turbulent boundary layer flow. This is to be contrasted with the transverse mean temperature profiles in fully developed turbulent channel flow (Lavertu & Mydlarski, 2005), which are approximated well by truncated Gaussian distributions due to the bounded nature of the flow in the transverse direction. (Given that the channel walls are adiabatic, a more accurate representation would be a Gaussian profile with a “mirror source” located at $-y_{source}/h$. However, given the objectives of their work, Lavertu & Mydlarski (2005) concluded the added complexity provided little additional insight.) Finally, the mean temperature profiles presented in Lavertu & Mydlarski (2005) show no discernable displacement of the peaks with downstream position (i.e. they remain fixed at the source location). In grid turbulence (Warhaft, 1984), the mean temperature profiles were Gaussian. The same is true in homogeneous turbulent shear flow (Karnik & Tavoularis, 1989) for downstream positions close to the source. Farther downstream, however, Karnik & Tavoularis (1989) observed that the mean temperature profiles became asymmetric and their peak drifted into the lower velocity region.

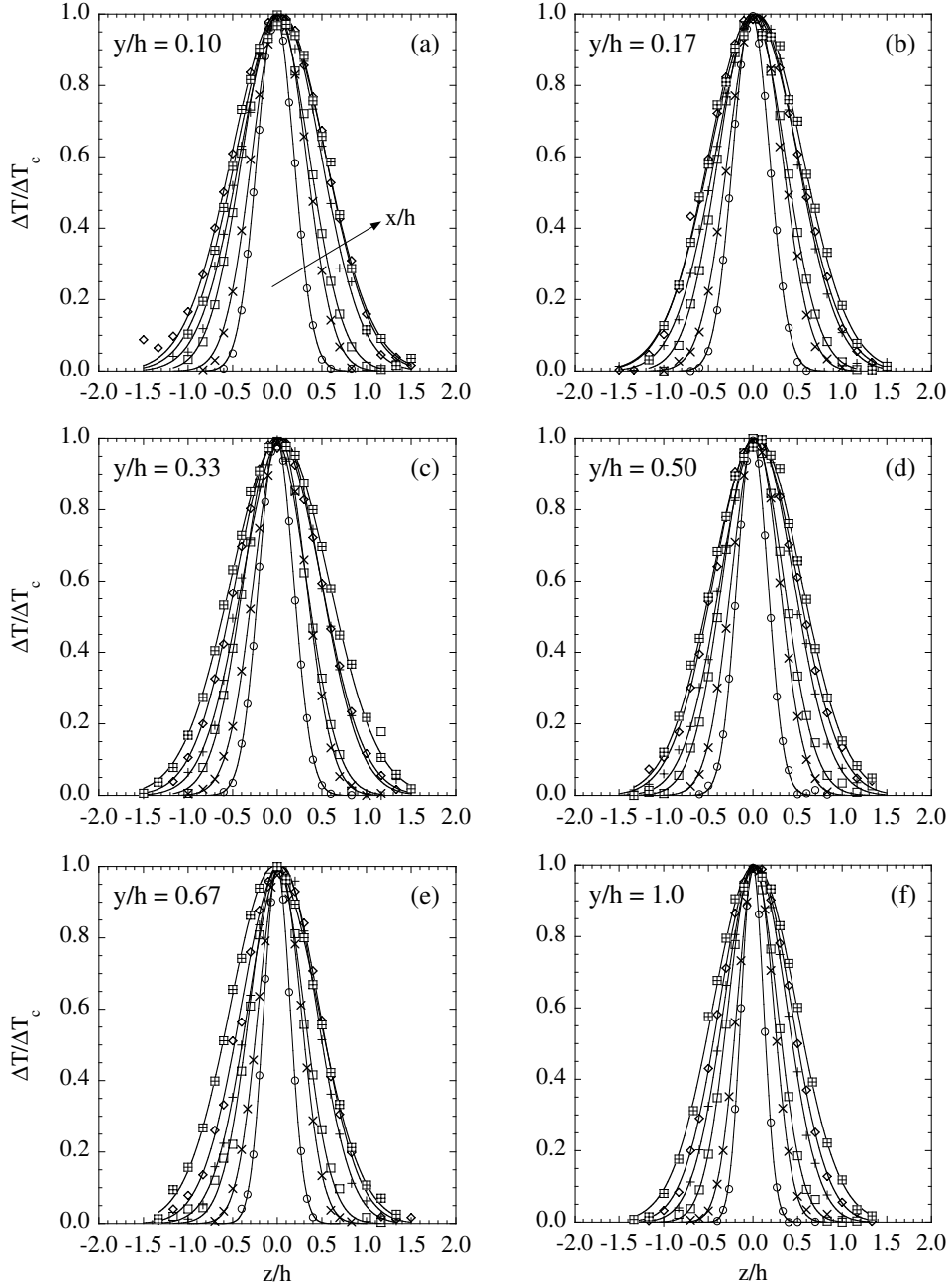


Figure 4.9: Downstream (x) evolution of the lateral (z) profiles of the mean temperature excess (ΔT), non-dimensionalized by their peak value (ΔT_c), for six wall-normal distances: (a) $y/h = 0.10$, (b) $y/h = 0.17$, (c) $y/h = 0.33$, (d) $y/h = 0.50$, (e) $y/h = 0.67$, (f) $y/h = 1.0$. Symbols denote different downstream positions: \circ : $x/h = 4.0$, \times : $x/h = 7.4$, \square : $x/h = 10.8$, $+$: $x/h = 15.2$, \diamond : $x/h = 18.6$, \boxplus : $x/h = 22.0$. The solid lines correspond to the best fit Gaussian profiles.

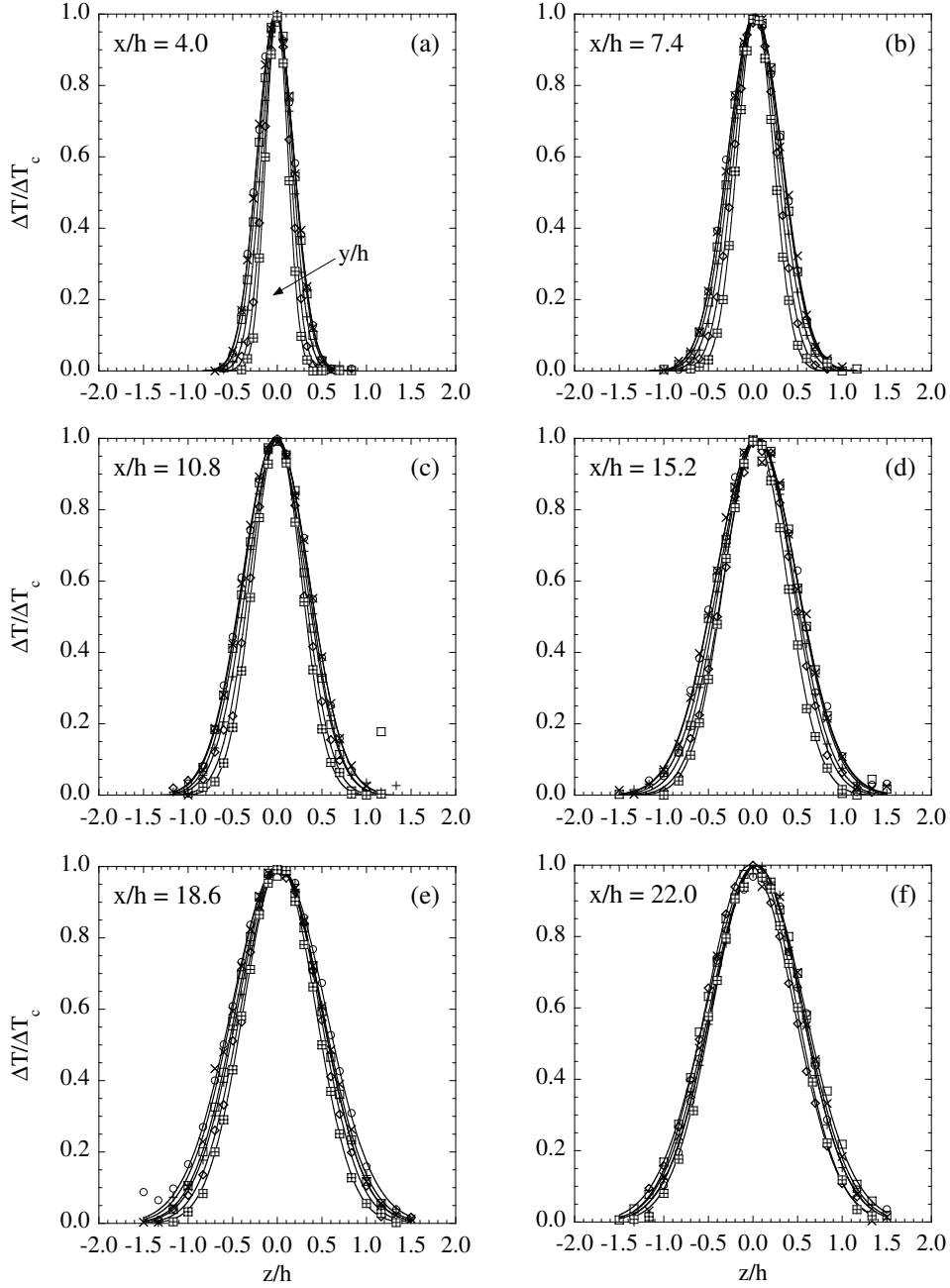


Figure 4.10: Transverse (y) evolution of the lateral (z) profiles of the mean temperature excess (ΔT), non-dimensionalized by their peak value (ΔT_c), for six downstream positions: (a) $x/h = 4.0$, (b) $x/h = 7.4$, (c) $x/h = 10.8$, (d) $x/h = 15.2$, (e) $x/h = 18.6$, (f) $x/h = 22.0$. Symbols denote different wall-normal distances: \circ : $y/h = 0.10$, \times : $y/h = 0.17$, \square : $y/h = 0.33$, $+$: $y/h = 0.50$, \diamond : $y/h = 0.67$, \boxtimes : $y/h = 1.0$. The solid lines correspond to the best fit Gaussian profiles.

The (downstream and transverse) evolutions of the centreline mean temperature excess (ΔT_c) are shown in figure 4.11. These are non-dimensionalized by the “reference temperature rise” (ΔT_r) proposed by Karnik & Tavoularis (1989)

$$\Delta T_r = \frac{P'}{\rho c_P d_s \langle U \rangle}, \quad (4.1)$$

where P' is the power injected into the source per unit length, d_s is the diameter of the source, and ρ and c_P are the density and specific heat capacity at constant pressure of the ambient air, respectively. Consistent with homogeneous turbulence (and in contrast with the results of Lavertu & Mydlarski (2005) for dispersion in the inhomogeneous (y) direction), the downstream decay of the centreline mean temperature excess (see figure 4.11a) is described well by a power law of the form

$$\frac{\Delta T_c}{\Delta T_r} = A \left(\frac{x}{h} \right)^m. \quad (4.2)$$

This result, and its consistency with results in purely homogeneous flow, is not unreasonable, given the unbounded and homogeneous nature of the flow in the spanwise direction. The parameters in the power law curve fit above are shown in table 4.4. The value of m falls in the range $-0.78 \leq m \leq -0.68$, and exhibits a non-monotonic trend in wall-normal distance exhibiting the slowest decay around $y/h \approx 0.5$. The present values are comparable to those obtained in homogeneous turbulence: Warhaft (1984) obtained a decay exponent on the order of $m \sim -0.7$ (over the entire range of downstream positions under consideration therein), whereas Karnik & Tavoularis (1989) quoted an exponent of $m \approx -1.0$ near the source and $m \approx -0.75$ farther downstream. In the fully developed channel flow experiments of Lavertu & Mydlarski (2005), the data were not well represented by a power-law, owing to the bounded nature of the flow. Nevertheless, the authors computed decay

exponents of $m \sim -0.7$ to -0.5 , solely for the sake of comparison with the above-mentioned homogeneous flows.

The non-monotonic trend of the power law scaling exponents with wall-normal distance observed herein merits further discussion. Table 4.4 reveals that the fastest decay rates occur at the near-wall and centreline locations. In the near-wall region, the higher turbulence intensity (and/or the increased advection time due to the lower mean velocity) serves to enhance the mixing of the thermal plume, yielding a rapid decay rate of the peak mean temperature. Consequently, the drop in turbulent kinetic energy associated with increasing wall-normal distance may result in the initial decay of m observed herein. However, as the distance from the wall increases, bulk “flapping” of the instantaneous thermal plume (by the large eddies in the flow) becomes more prominent (see the temperature PDFs in section 4.2.3), and accelerates the spreading of the mean plume. As the mean plume widens, the peak mean temperature decreases, to satisfy conservation of energy. Therefore, the observed faster decay at the channel centreline is presumably related to the increased flapping of the plume at that location.

Figure 4.11(b) plots the transverse evolution of the centreline mean temperature excess for the different downstream positions. When plotted using logarithmic coordinates (not shown), the data appear to be described well using a power law, though no theoretical justification exists for this behaviour. Given that the curves should be symmetric about $y/h = 1.0$, a power law in y is incompatible with the underlying symmetry of the experiment. The fact that a power law fits the data well is most probably coincidental, and presumably results from the relatively few (six) data points in the transverse (y) direction. Were more data points used — especially near the wall — a power law may very well cease to accurately fit the data over this wider range of

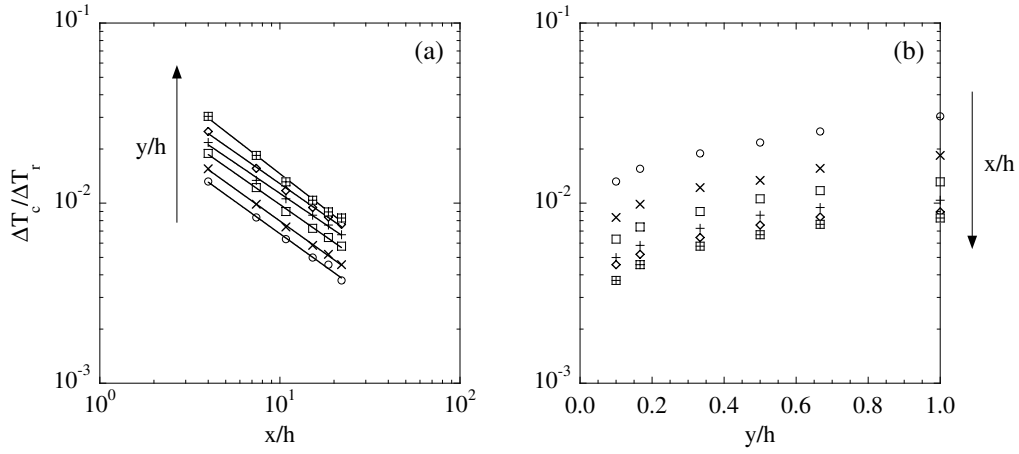


Figure 4.11: The (a) downstream and (b) transverse evolution of the centre-line mean temperature excess (ΔT_c) non-dimensionalized using the reference temperature rise (ΔT_r). In (a), symbols denote different wall-normal distances (see figure 4.10). In (b), symbols denote different downstream positions (see figure 4.9). The solid lines correspond to the best fit power law.

Table 4.4: Parameters corresponding to the power-law evolution of the normalized peaks and half-widths of the mean temperature excess (ΔT) profiles: $\Delta T_c/\Delta T_r = A(x/h)^m$ and $z_{1/2}^{mean}/h = B(x/h)^n$.

y/h	A	m	B	n
0.10	0.0355	-0.72	0.116	0.55
0.17	0.0415	-0.72	0.116	0.55
0.33	0.0491	-0.70	0.103	0.59
0.50	0.0540	-0.68	0.0887	0.62
0.67	0.0641	-0.70	0.0677	0.70
1.0	0.0869	-0.78	0.0522	0.76

scales. Nevertheless, a power law fit ($\Delta T_c/\Delta T_r = C(y/h)^p$) was applied to the transverse evolution data, for the sole purpose of obtaining a quantitative estimate of the transverse evolution to be compared with that in the downstream direction. One obtains exponents in the range of $0.31 \leq p \leq 0.35$ and the value of p decreases non-monotonically with increasing downstream position. The smaller variation of p suggests that the transverse growth of the peak mean temperature is less sensitive to the downstream position. One can infer that this “quasi-homogeneous” behaviour in the downstream direction arises from the weaker inhomogeneity of the scalar field in that direction. We also note that the centreline mean temperature excess decays at a much slower rate in the transverse direction (as compared to the downstream evolution). This is presumably due to the bounded nature of the flow in the transverse direction (which stifles the growth of the plume in the transverse direction, thus yielding a slower decay rate of the peak mean temperature). Given that all bounded flows are inherently inhomogeneous, there is no a priori reason to assume that the transverse plume should evolve in a manner similar to the lateral plume, as observed.

Figures 4.12(a) and 4.12(b) plot the development of the half-width of the mean temperature excess profiles ($z_{1/2}^{mean}$). Once again, power laws are fitted to the downstream evolution data such that:

$$\frac{z_{1/2}^{mean}}{h} = B \left(\frac{x}{h} \right)^n, \quad (4.3)$$

with the parameters B and n being summarized in table 4.4. We note that, near the wall, the profiles are wider than the corresponding profiles at the centreline. This may be attributed to one (or both) of two phenomena: (i) upon reaching a given downstream distance, the scalar contaminant has had more time to diffuse, given the lower mean velocity in the near-wall region, and/or

(ii) a larger turbulent kinetic energy near the wall enhances the spreading of the scalar field. This being said, it is worth noting that the power law exponent n increases monotonically from 0.55 to 0.76 as y/h increases from 0.10 to 1.0 — i.e. the growth rate of the width of the mean temperature profiles is smallest at the wall and largest at the channel centreline. In the turbulent boundary layer studies of Fackrell & Robins (1982), the half-widths of the lateral mean concentration profiles obey a power law distribution with exponent $n \approx 1/2$ (far downstream of the elevated source). This result agrees well with the near-wall observations ($n = 0.55$) herein, presumably due to the fact that the source locations studied in Fackrell & Robins (1982) are comparable to the near-wall source locations investigated herein. In grid turbulence, Warhaft (1984) examined the effect of the turbulence intensity at the source location by changing the downstream position of the source with respect to the grid (since grid turbulence decays with downstream position). Consistent with the present results, Warhaft (1984) obtained wider profiles with a line source located closer to the grid (i.e. higher turbulent kinetic energy at the source location). However, in contradiction with the present results, there was no discernable effect on the growth rate of the plume — the power law exponent had an approximate value of $n \sim 0.7$, regardless of the turbulence intensity at the source location. Warhaft (1984) states that, in homogeneous turbulence, the product of the peak mean temperature and the half-width of the mean temperature profile should remain constant (to satisfy conservation of energy). Therefore, the peak mean temperature decay exponent and the power law exponent describing the downstream evolution of the half-width of the mean temperature profile should be equal in magnitude and opposite in sign — as is the case in Warhaft (1984). In the present work, table 4.4 reveals that this does not hold, given that the flow is inhomogeneous. However, at

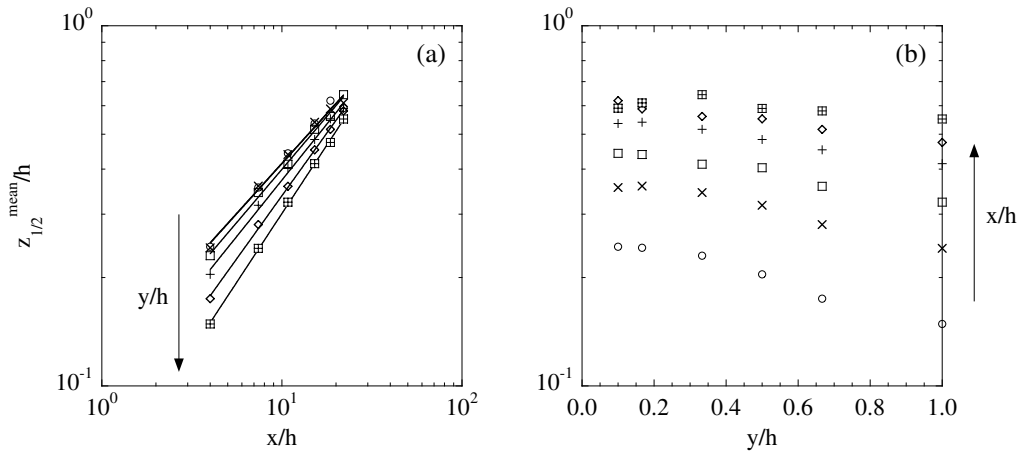


Figure 4.12: The (a) downstream and (b) transverse evolution of the half-width ($z_{1/2}^{mean}$) of the mean temperature excess profiles non-dimensionalized using the channel half-width (h). In (a), symbols denote different wall-normal distances (see figure 4.10). In (b), symbols denote different downstream positions (see figure 4.9). The solid lines correspond to the best fit power law.

$y/h = 1.0$, $m \approx -n$, which is not unreasonable, given that the symmetry at the centreline results in a “quasi-homogeneous flow” (since the gradients at this location are zero). The half-width data presented in Warhaft (1984) suggests that the observed evolution of n with y/h cannot be solely attributed to differences in the turbulent kinetic energy at the given wall-normal location. Nakamura *et al.* (1986) investigated the effect of (mean) shear on the mean concentration statistics of a dye emitted from a continuous point source in uniformly sheared, homogeneous turbulence. They determined that the growth rate of the half-width of the mean concentration profiles shows a dependence on the mean shear. More precisely, they observe an increase in the growth rate of the half-width of the mean concentration profiles (n) with decreasing shear parameter (Λ), which they define as: $\Lambda \equiv (\sqrt{3}/2)A_h^{-1/2}A_z^{-1/2}\Omega_z^{-1}U_{CL}^2$, where A_h and A_z are the turbulent scalar diffusivities in the directions normal and parallel to the velocity gradient, respectively (and assumed to be constant), Ω_z is the uniform mean shear rate and U_{CL} is the velocity at the mid-height of the channel. Consequently, the observed increase in the growth rate of the half-width of the mean temperature profile (n) with increasing wall-normal distance might be explained by the decreasing mean velocity gradient in that same direction.

A primary objective of the current work is to compare the lateral dispersion measured herein to the transverse dispersion studied in Lavertu & Mydlarski (2005). One observes that the half-widths of the mean temperature profiles presented in 4.12(a) are well represented by a power law distribution, whereas the data presented in Lavertu & Mydlarski (2005) — see their figure 7(c), for example — appears to plateau for large downstream distances. Consequently, one can infer that, far downstream of the source, the lateral half-width of the mean temperature field is larger than the transverse half-width. Fackrell

& Robins (1982) observed a similar behaviour of the mean-profile half-widths in their experiments (albeit for all of the downstream locations under consideration therein). This may be attributed to the unbounded nature of the lateral dispersion, whereas the presence of the wall stifles the growth of the transverse plume.

Turning our attention to the transverse evolution of the half-width of the mean plume (figure 4.12b), one observes that the width of the thermal plume becomes uniform across the entire channel half-width far downstream of the source location, consistent with the observations presented in Fackrell & Robins (1982). Such an observation may potentially arise due to the approach of a shear flow dispersion regime (Taylor, 1953, 1954), where, for large downstream distances, the randomly moving fluid particles have been able to explore the entire channel (in the flow’s inhomogeneous, y -direction).

Following Paranthoën *et al.* (1988), who successfully collapsed the peak mean temperature data from a variety of dispersion experiments (in boundary layers, plane jets and pipe flows) using the integral Lagrangian time scale of the transverse velocity fluctuation at the source location, plotted in figure 4.13 is the downstream evolution of both the peak (centreline) value and the half-width of the mean temperature excess profiles using a quasi-Lagrangian non-dimensionalization of the downstream coordinate. Instead of non-dimensionalizing the downstream position (x) by the channel half-width (h) — as done in figure 4.11(a) — the flight time from the source ($x/\langle U \rangle$) is non-dimensionalized by (an approximation of) the local Lagrangian time scale. The latter is estimated from the (local) longitudinal root-mean-square turbulent velocity fluctuation, u' ($= u'(y)$), and a turbulent length scale. In the present work, one of two length scales is used: (i) the channel half-width (yielding a local Lagrangian time scale of h/u'), or (ii) the integral length scale of

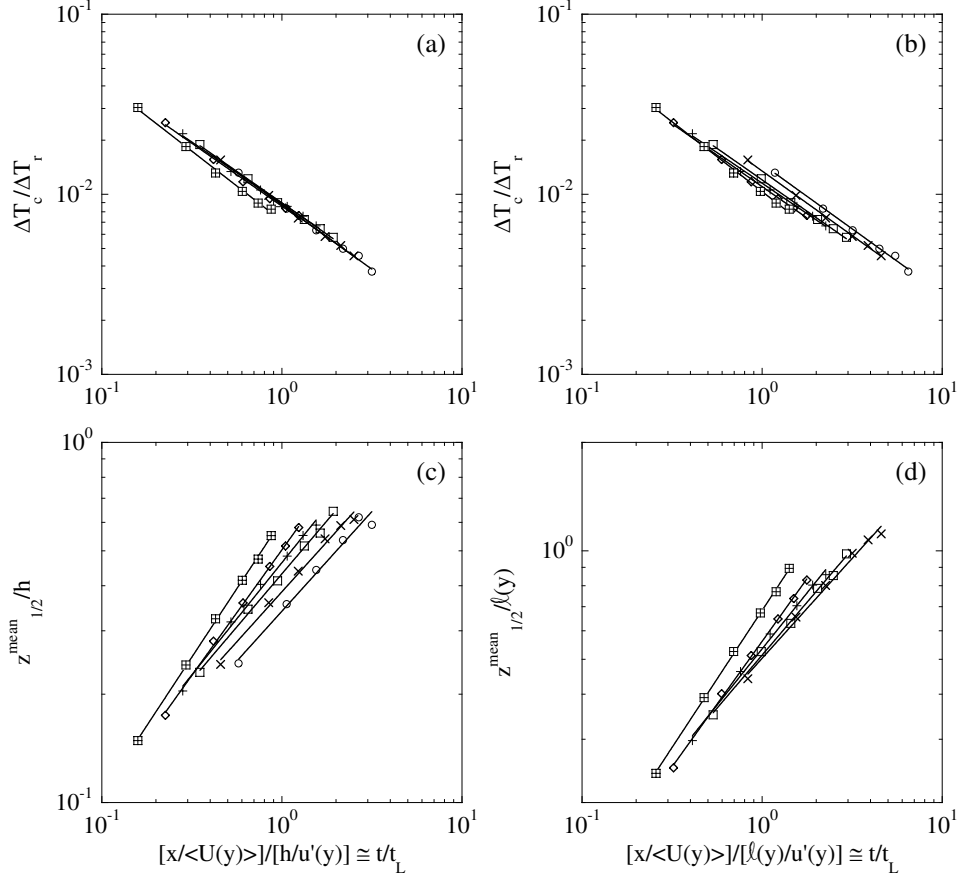


Figure 4.13: The downstream evolution of the centreline value (ΔT_c) and half-width ($z_{1/2}^{mean}$) of the mean temperature excess profiles, using a Lagrangian non-dimensionalization. (a), (b): ΔT_c . (c), (d): $z_{1/2}^{mean}$. (a), (c): non-dimensionalization using the channel half-width (h). (b), (d): non-dimensionalization using the integral length scale of the turbulence (ℓ). Symbols denote different wall-normal distances: \circ : $y/h = 0.10$, \times : $y/h = 0.17$, \square : $y/h = 0.33$, $+$: $y/h = 0.50$, \diamond : $y/h = 0.67$, \boxplus : $y/h = 1.0$. The solid lines correspond to the best fit power law.

the turbulence (ℓ/u'). (Note that $\ell = \ell(y)$ is a function of the transverse position, whereas h is constant.) One observes that both non-dimensionalizations collapse the peak mean excess temperature data — see figures 4.13(a) and (b). This result is consistent with that obtained by Paranthoën *et al.* (1988) in a turbulent boundary layer. However, the data non-dimensionalized using the constant length scale h does not collapse the half-width data (figure 4.13c), whereas figure 4.13(d) reveals that non-dimensionalizing using $\ell(y)$ significantly improves the collapse of $z_{1/2}^{mean}$. Figure 4.13(d) illustrates the importance of using local characteristic scales when non-dimensionalizing quantities of interest in the present inhomogeneous flow. Moreover, one observes a significant improvement in the collapse of the half-width ($z_{1/2}^{mean}$) data when using the local characteristic scales as opposed to the peak mean temperature data, which show a reasonable collapse of the data regardless of the normalization. This is presumably because both the half-width and the downstream distance are non-dimensionalized by $\ell(y)$, whereas only the latter is non-dimensionalized by $\ell(y)$ in the case of the peak mean excess temperature data.

4.2.2 The fluctuating temperature field

The spanwise profiles of the r.m.s. temperature fluctuations (θ'), normalized by the centreline value (θ'_c), are plotted in figures 4.14 (downstream evolution) and 4.15 (transverse evolution). Unlike the mean temperature profiles, the r.m.s. profiles are non-Gaussian. However, they remain symmetric about $z/h = 0$ — as required by the underlying symmetries. Furthermore, the r.m.s. profiles, which are initially single-peaked, evolve into double-peaked profiles (i) with increasing downstream position and (ii) as the wall is approached. Both Warhaft (1984) and Karnik & Tavoularis (1989) observed non-Gaussian r.m.s. profiles that were double-peaked very close to the source, then evolved into single-peaked profiles, only to become double-peaked once again farther

downstream. (We note that, while not observed herein, it remains extremely probable that the r.m.s. profiles are double-peaked for downstream positions that are very close to the source, i.e. for $x/h \ll 4.0$, which corresponds to the farthest upstream measurement location.) In Lavertu & Mydlarski (2005), the r.m.s. profiles were approximated well by truncated Gaussian profiles, though deviations began to appear for the largest downstream distances when the line source was located at the channel centreline. For the range of downstream positions considered therein, the profiles remained single-peaked.

The appearance, disappearance and re-emergence of the double-peaked r.m.s. profiles have been explained by Warhaft (1984) and Karnik & Tavoularis (1989) as follows. Temperature fluctuations arise predominantly from one (or both) of two mechanisms: (i) turbulent production in regions of non-zero temperature gradients, and (ii) turbulent transport of temperature by velocity fluctuations, both of which appear in the transport equation of scalar variance ($\langle \frac{1}{2}\theta^2 \rangle$), notably:

$$\frac{\partial \langle \frac{1}{2}\theta^2 \rangle}{\partial t} + \langle U_j \rangle \frac{\partial \langle \frac{1}{2}\theta^2 \rangle}{\partial x_j} = \frac{\partial}{\partial x_j} \left[\alpha \frac{\partial \langle \frac{1}{2}\theta^2 \rangle}{\partial x_j} \right] - \underbrace{\langle u_j \theta \rangle \frac{\partial \langle \Theta \rangle}{\partial x_j}}_A - \underbrace{\frac{\partial \langle \frac{1}{2}u_j \theta^2 \rangle}{\partial x_j}}_B - \chi,$$

and are respectively labeled as terms “A” and “B.” For downstream positions very close to the source, Warhaft (1984) argues that the thermal plume, having had little time to evolve, is very narrow and, therefore, much smaller than the typical size of the transporting eddies. Consequently, there is little turbulent structure within the plume and temperature fluctuations arise predominantly from “flapping” of the thermal plume (i.e. advection of the plume by the largest turbulent eddies that are larger than the plume itself). Therefore, one would expect the largest temperature fluctuations to occur off the centreline, along the edge of the plume. One can imagine that a cold-wire probe placed along this interface would frequently measure both the hot fluid heated

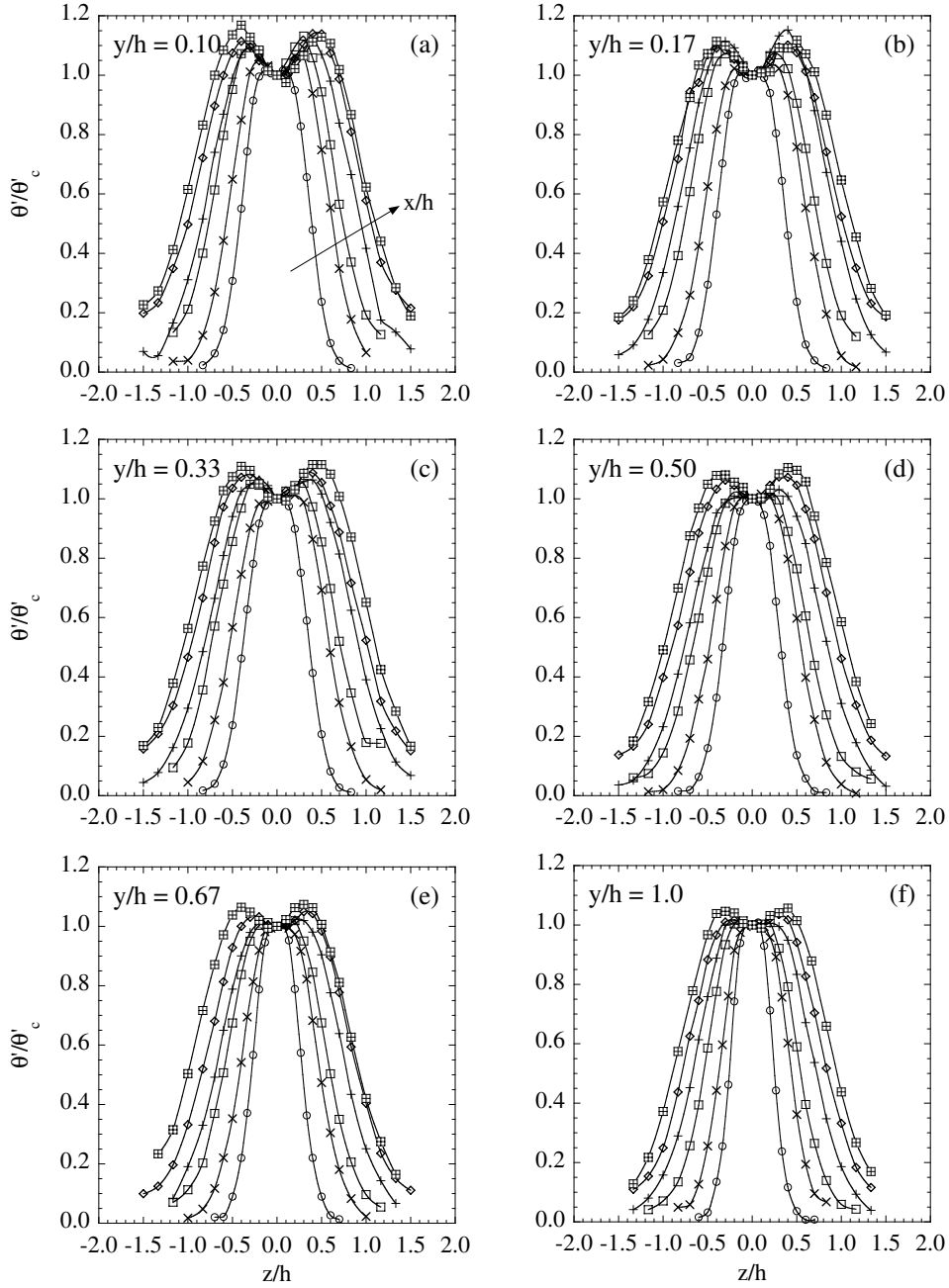


Figure 4.14: Downstream (x) evolution of the lateral (z) profiles of the non-dimensionalized root-mean-square temperature for six wall-normal elevations. (a) $y/h = 0.10$, (b) $y/h = 0.17$, (c) $y/h = 0.33$, (d) $y/h = 0.50$, (e) $y/h = 0.67$, (f) $y/h = 1.0$. Symbols denote different downstream positions: \circ : $x/h = 4.0$, \times : $x/h = 7.4$, \square : $x/h = 10.8$, $+$: $x/h = 15.2$, \diamond : $x/h = 18.6$, \boxplus : $x/h = 22.0$.

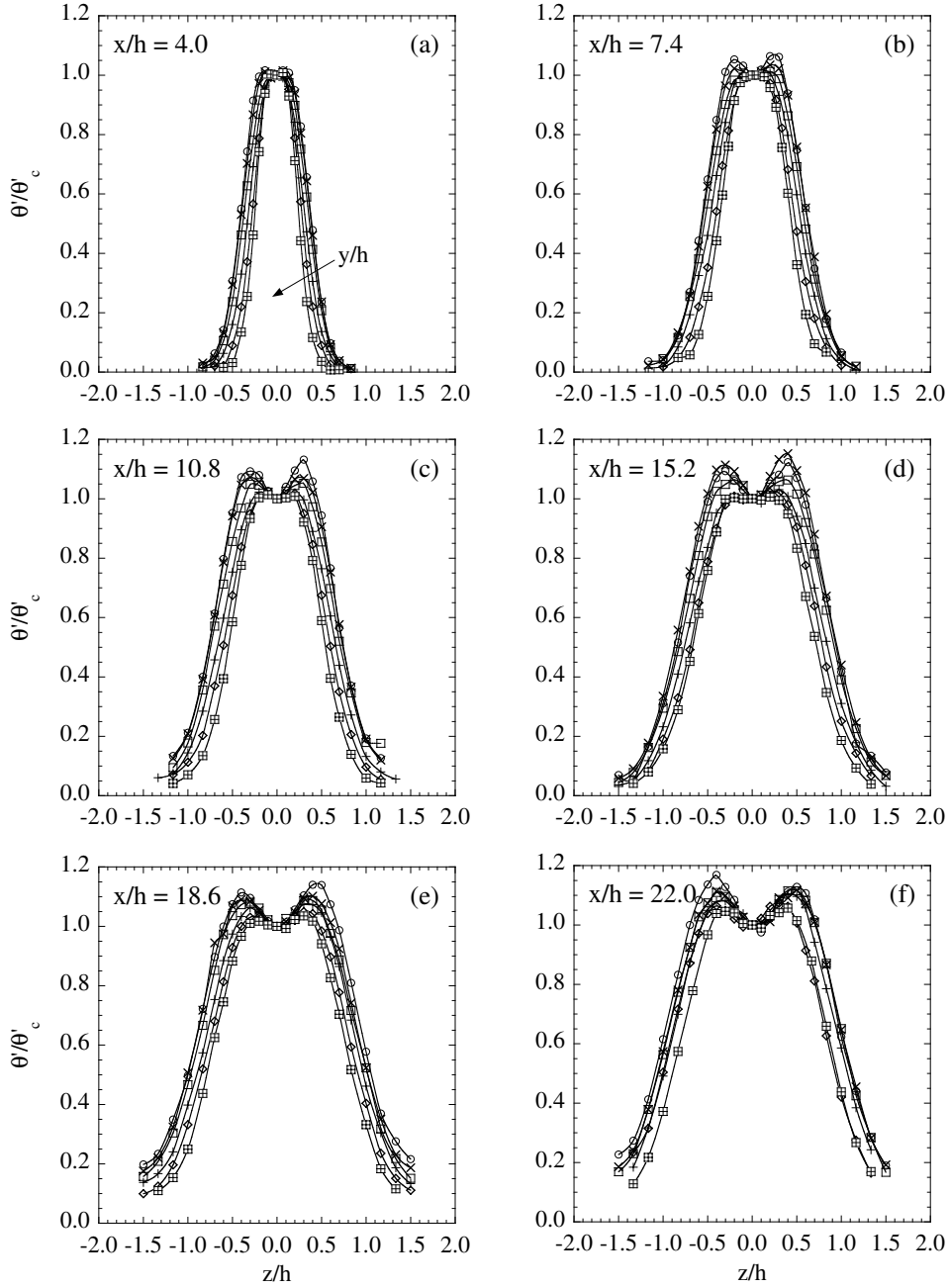


Figure 4.15: Transverse (y) evolution of the lateral (z) profiles of the non-dimensionalized root-mean-square temperature for six downstream positions. (a) $x/h = 4.0$, (b) $x/h = 7.4$, (c) $x/h = 10.8$, (d) $x/h = 15.2$, (e) $x/h = 18.6$, (f) $x/h = 22.0$. Symbols denote different wall-normal distances: \circ : $y/h = 0.10$, \times : $y/h = 0.17$, \square : $y/h = 0.33$, $+$: $y/h = 0.50$, \diamond : $y/h = 0.67$, \boxplus : $y/h = 1.0$.

by the line source and the surrounding cold fluid (compared to a probe placed on either side of the interface, which would predominantly measure either the hot or cold fluid). Far downstream of the line source, Karnik & Tavoularis (1989) proposed that the reappearance of double-peaked r.m.s. profiles occurs when the width of the thermal plume exceeds the typical size of the transporting eddies (i.e. the integral length scale of the turbulence). Consider, for example, a Gaussian mean temperature profile. In this scenario, the mean temperature gradients (and consequently, the turbulent production term in the scalar variance budget) are the largest away from the centreline (at the point of inflection of the mean profile). If the transporting eddies are small compared to the width of the thermal plume, then the contribution of turbulent transport to the temperature fluctuations will be small compared to their production. Therefore, one can expect the largest temperature fluctuations to coincide with the location of the maximum mean temperature gradient, resulting in the double-peaked r.m.s. profiles. (Furthermore, Karnik & Tavoularis (1989) demonstrated that, given a Gaussian mean temperature profile — and invoking a constant turbulent diffusivity assumption — the turbulent production term becomes double-peaked and that the peaks become more prominent with increasing downstream position.) However, between these two regimes, when the width of the plume is comparable to the integral length scale of the turbulence, both mechanisms create temperature fluctuations. In this case, the turbulent transport term smooths out the double peaks of the turbulent production term, resulting in single-peaked r.m.s. profiles.

The downstream development and transverse evolution of the centreline r.m.s. temperature fluctuation (θ'_c), non-dimensionalized by the reference temperature rise (ΔT_r), is plotted in figures 4.16(a) and 4.16(b), respectively. As was the case for the mean temperature profiles (and consistent with the

work in homogeneous turbulence), the downstream evolution of the centreline r.m.s. temperature fluctuation (see figure 4.16a) follows a power law (analogous to equation 4.2) with exponent $-1.22 \leq m \leq -1.06$. Table 4.5 presents the parameters in the power law curve fit for the six different transverse positions. One notices that for $y/h = 0.10$ to $y/h = 0.33$, the exponent remains approximately constant, and then decreases with increasing wall-normal position. In homogeneous flow, Warhaft (1984) observed a power law exponent of $m \sim -1$ (which held over the entire extent of downstream positions considered therein). This result is consistent with the observations herein at the channel centreline ($m = -1.06$ at $y/h = 1.0$), due to the quasi-homogeneous behaviour of the flow at the channel centreline. As the wall is approached, the mixing is enhanced due to the larger turbulence intensity and, consequently, the fluctuating temperature field decays more rapidly. Karnik & Tavoularis (1989) identified two distinct scaling regions with different scaling exponents: $m \approx -0.85$ near the source and $m \approx -1.6$ far downstream. This result is not without justification, given that the homogenous shear flow therein produces a turbulent velocity field that increases in turbulence intensity with downstream position (as opposed to the present experiment, in which the flow field is statistically homogeneous in the downstream direction). Therefore, one may attribute the increase in the decay rate with an increased level of turbulent kinetic energy. In fully developed turbulent channel flow, Lavertu & Mydlarski (2005) measured a decay exponent of $m \approx -1$, which, once again, is consistent with the present work. Moreover, Sakai *et al.* (1986) demonstrated that the decay exponent of the centreline r.m.s. fluctuation is sensitive to the mean-flow shear. In particular, they determined that the r.m.s temperature decays faster as the mean-flow shear increases. (This observation is consistent with the present work, given that the decay exponents presented herein increase

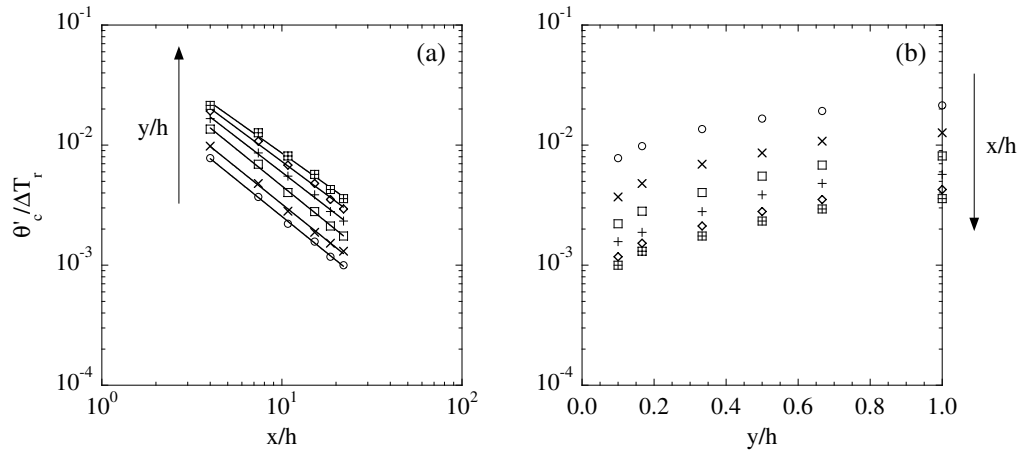


Figure 4.16: The (a) downstream and (b) transverse evolution of the centreline root-mean-square temperature fluctuation (θ'_c) non-dimensionalized using the reference temperature rise (ΔT_r). In (a), symbols denote different wall-normal distances (see figure 4.15). In (b), symbols denote different downstream positions (see figure 4.14). The solid lines correspond to the best fit power law.

Table 4.5: Parameters corresponding to the power-law evolution of the normalized centreline values and half-widths of the root-mean-square temperature (θ') profiles: $\theta'_c/\Delta T_r = A(x/h)^m$ and $z_{1/2}^{rms}/h = B(x/h)^n$.

y/h	A	m	B	n
0.10	0.0415	-1.21	0.182	0.59
0.17	0.0519	-1.21	0.179	0.59
0.33	0.0750	-1.22	0.161	0.62
0.50	0.0851	-1.16	0.133	0.67
0.67	0.0944	-1.11	0.109	0.71
1.0	0.0995	-1.06	0.0895	0.76

with decreasing wall-normal distance.) Consequently, the present results, as well as those available in the literature, would suggest that the decay rate of the centreline r.m.s. temperature fluctuation is influenced by both the turbulence intensity of the flow as well as the magnitude of the mean-flow shear. These parameters are summarized in table 4.6 for the different flows considered herein.

The transverse evolution of the centreline r.m.s. temperature fluctuation is presented in figure 4.16(b) for the six different downstream positions. In spite of the same lack of a theoretical justification (previously discussed in detail with respect to figure 4.11b), the data are described well using a power law distribution when plotted in logarithmic coordinates (not shown). The power law exponents fall in the range $0.45 \leq p \leq 0.59$ and their variation with downstream position is non-monotonic. The growth rate increases with downstream position (attaining a maximum value of $p = 0.59$ at $x/h \approx 15.2$) and decreases thereafter.

Figure 4.17(a) plots the downstream development of the half-width of the r.m.s. temperature profiles. Like the mean temperature profiles, the r.m.s. profiles are wider at the walls (compared to those at the centreline), while exhibiting a faster growth at the centreline. Fitting a power law distribution to the data (akin to equation 4.3), one obtains an exponent that increases monotonically from $n = 0.59$ at $y/h = 0.1$ to $n = 0.76$ at $y/h = 1.0$ (see table 4.5). Lavertu & Mydlarski (2005) obtained power law exponents in the range of $n = 0.37$ to $n = 0.68$. In Warhaft (1984), contrary to his results for the mean temperature field, the power law exponents describing the growth rates of the half-width of the r.m.s. profile exhibited a trend with turbulence intensity, increasing from $n \sim 0.4$ to $n \sim 0.6$ with decreasing turbulence intensity. Both the current research and that of Warhaft (1984) exhibit similar trends

Table 4.6: Comparison of previous and present flows in which scalar dispersion from a concentrated source has been studied.

	Nature of flow	Shear (S)	$S \langle u^2 \rangle / \epsilon$	$S(\nu/\epsilon)^{1/2}$	Evolution of $u' / \langle U \rangle$	$u' / \langle U \rangle$ at source [%]	Nature of source	Scalar field
Warhaft (1984)	Homogeneous & Isotropic	None	0	0	Decreasing in x (Const. in y & z)	2-11	Line (in z)	2-D (in x and y)
Nakamura <i>et al.</i> (1986), Sakai <i>et al.</i> (1986)	Homogeneous & Anisotropic	Constant in z (None in x and y)	Not Available	Not Available	Increasing in x (Const. in y & z)	Not Available	Point	3-D
Karnik & Tavoularis (1989)	Homogeneous & Anisotropic	Constant in y (None in x and z)	~ 9	~ 0.1	Increasing in x (Const. in y & z)	5	Line (in z)	2-D (in x and y)
Lavertu & Mydlarski (2005)	Inhomogeneous	Variable in y (None in x and z)	0-8	0-0.3	Variable in y (Const. in x & z)	4-14	Line (in z)	2-D (in x and y)
Present work	Inhomogeneous	Variable in y (None in x and z)	0-8	0-0.3	Variable in y (Const. in x & z)	4-14	Line (in y)	3-D (in x and y)

regarding the growth rates of the half-widths of the r.m.s. profiles (n), and their relationship to the turbulence intensity of the flow at the source location. (Note that in Warhaft (1984), the turbulence intensity at the source location is varied by changing the downstream position of the source relative to the grid that generates the turbulent velocity field, whereas the present work examines the influence of the turbulence intensity at the injection site by varying the wall-normal position.) While the magnitudes of the exponents in the current work are larger than those of Warhaft (1984), the turbulence intensities in Warhaft (1984) are smaller than those in the present experiment. This observation implies that while the turbulence intensity of the flow plays an important role in the growth rate of the r.m.s. plume, it is not solely responsible for the observed variation of n among the results quoted in the literature. Presumably, as was the case for the mean temperature field, the mean-flow shear also influences the growth rates of the r.m.s. profiles. Consequently, the current results — as well as those of Warhaft (1984) and Lavertu & Mydlarski (2005) — would suggest that while the turbulence intensity at the source location is inversely related to the growth rate of the r.m.s. profiles, the mean-flow shear may also enhance the spreading of the r.m.s. profiles (in a manner similar to the mean temperature profiles).

In examining the transverse evolution of the half-width of the r.m.s. profiles (figure 4.17b), one observes once again that, far downstream, the lateral width of the profiles becomes uniform across the width of the channel, at roughly the same rate as the half-widths of the mean temperature plume. Upon examination of tables 4.4 and 4.5, one also notices that the scaling exponents describing the power law growth of the plume half-widths (n) are roughly the same for both the mean and r.m.s. profiles, which is consistent with the behaviour described above.

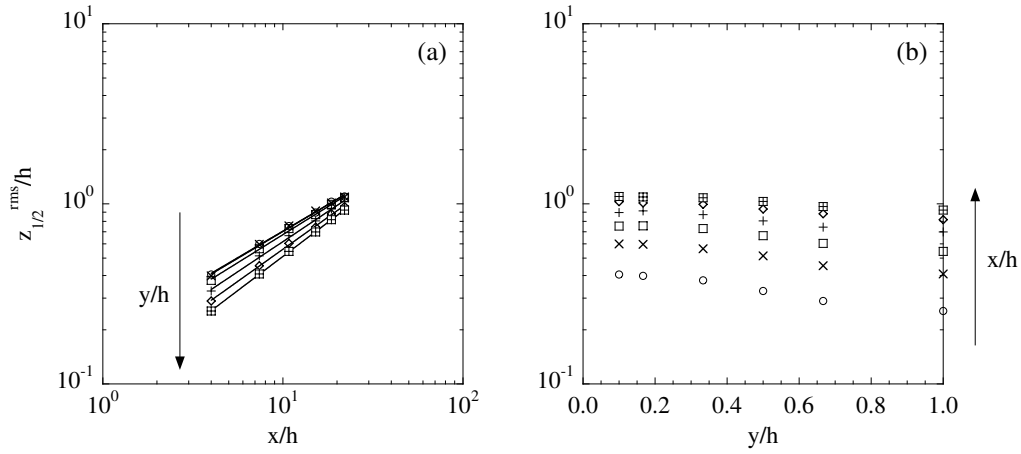


Figure 4.17: The (a) downstream and (b) transverse evolution of the half-width ($z_{1/2}^{rms}$) of the root-mean-square temperature profiles non-dimensionalized using the channel half-width (h). In (a), symbols denote different wall-normal distances (see figure 4.15). In (b), symbols denote different downstream positions (see figure 4.14). The solid lines correspond to the best fit power law.

Figure 4.18 presents the downstream evolution of the centreline r.m.s. temperature fluctuation and the half-width of the r.m.s. temperature profile, respectively, using the quasi-Lagrangian non-dimensionalizations introduced in section 4.2.1. Consistent with the results obtained for the mean temperature field, and in contrast with the boundary layer work of Paranthoën *et al.* (1988), the Lagrangian non-dimensionalization collapses the normalized centreline r.m.s. temperature fluctuation data onto a single curve (regardless of which length scale is employed in the normalization). Once again, the half-width data do not exhibit a similar collapse when non-dimensionalized by the channel half-width, whereas normalization using $\ell(y)$ improves the collapse.

To quantify the “mixedness” of the scalar field, the ratio of the centreline r.m.s. temperature fluctuation to the centreline mean temperature excess ($\theta'_c/\Delta T_c$) is plotted in figure 4.19. In a perfectly mixed flow, this ratio is zero, since the r.m.s. temperature fluctuation must be zero. (A perfectly mixed fluid will have the same concentration throughout its entirety.) When the downstream position (x) is non-dimensionalized using the channel half-width (h), as in figure 4.19(a), the data show the mixedness to increase (i.e. smaller $\theta'_c/\Delta T_c$) as the wall is approached and as one proceeds downstream. Replotting the data of figure 4.19(a) using the Lagrangian non-dimensionalizations introduced above collapses them onto a single curve — see figures 4.19(b) and 4.19(c). This is in contrast to the work of Paranthoën *et al.* (1988), who were unsuccessful in their attempt to collapse their plots of the intensity of the scalar fluctuations. Furthermore, the curve shows a monotonic decay from a value of 0.8 down to an asymptotic value of approximately 0.3. (Given the range of downstream distances examined herein, it is not possible to determine whether the curve exhibits a maximum in the range $0 \leq x/h \leq 4.0$.) In Warhaft (1984), this ratio peaked at a downstream position of $x'/M \approx 10$ (at the end of the

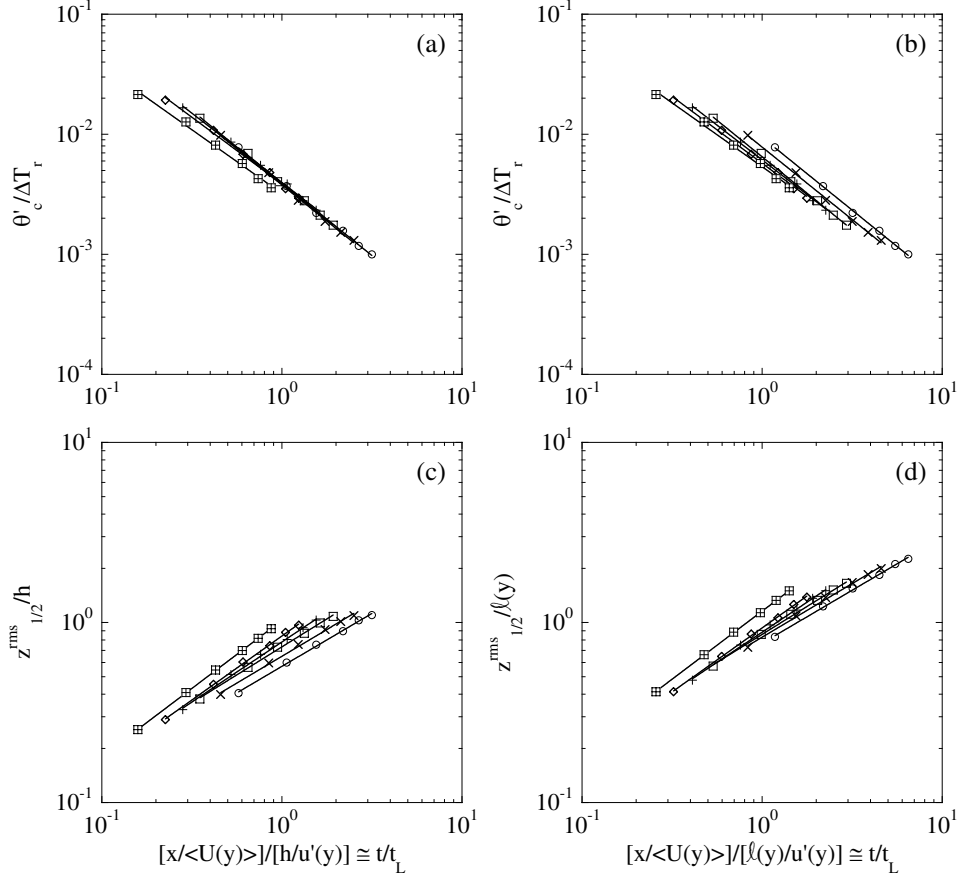


Figure 4.18: The downstream evolution of the centreline value (θ'_c) and half-width ($z_{1/2}^{rms}$) of the root-mean-square temperature profiles, using a Lagrangian non-dimensionalization. (a), (b): θ'_c . (c), (d): $z_{1/2}^{rms}$. (a), (c): non-dimensionalization using the channel half-width (h). (b), (d): non-dimensionalization using the integral length scale of the turbulence (ℓ). Symbols denote different wall-normal distances: \circ : $y/h = 0.10$, \times : $y/h = 0.17$, \square : $y/h = 0.33$, $+$: $y/h = 0.50$, \diamond : $y/h = 0.67$, \boxplus : $y/h = 1.0$. The solid lines correspond to the best fit power law.

turbulent convective regime) and asymptoted to a value of roughly 0.7. Karnik & Tavoularis (1989) observed similar trends — their data exhibited a peak at $x_\theta/M \sim 8$. However, they obtained much lower values than Warhaft (1984) — their curve appears to asymptote to a value of 0.15. Consistent with the present work, Lavertu & Mydlarski (2005) observed a monotonic decrease of the ratio $\theta'_c/\Delta T_c$ with no observable peak in their range of downstream measurement locations. However, in contrast to the current results, the magnitude of their ratio was 0.8 at $x/h = 18.6$, although the authors concluded that no inferences can be drawn concerning its asymptotic value. The intensity of the scalar fluctuations has also been examined in numerical simulations of fully developed turbulent channel flow (Vrieling & Nieuwstadt, 2003; Bakosi *et al.*, 2007). Although there is some variation between the asymptotic values of the scalar intensity (which fall in the range of $0.8 < \theta'_c/\Delta T_c < 1.0$), the data are consistent with the experimental results of Lavertu & Mydlarski (2005). Furthermore, the transverse dispersion data appear to asymptote to a value similar to (or slightly larger than) that measured in the homogeneous, isotropic turbulence of Warhaft (1984), which will be expounded upon shortly. Finally, Viswanathan & Pope (2008) performed numerical simulations of the thermal plume generated by means of a line source in grid turbulence (under conditions similar to those studied in Warhaft (1984)). Consistent with the current work, they determined that the intensity of scalar fluctuations asymptotes to a constant value of 0.4.

The difference in the asymptotic values between the three flows for which dispersion is occurring in an unbounded, homogeneous direction (i.e. (i) homogeneous isotropic turbulence, (ii) homogeneous turbulent shear flow, and (iii) lateral dispersion within a fully developed, high-aspect-ratio turbulent channel flow) reveals that the homogeneous turbulent shear flow of Karnik &

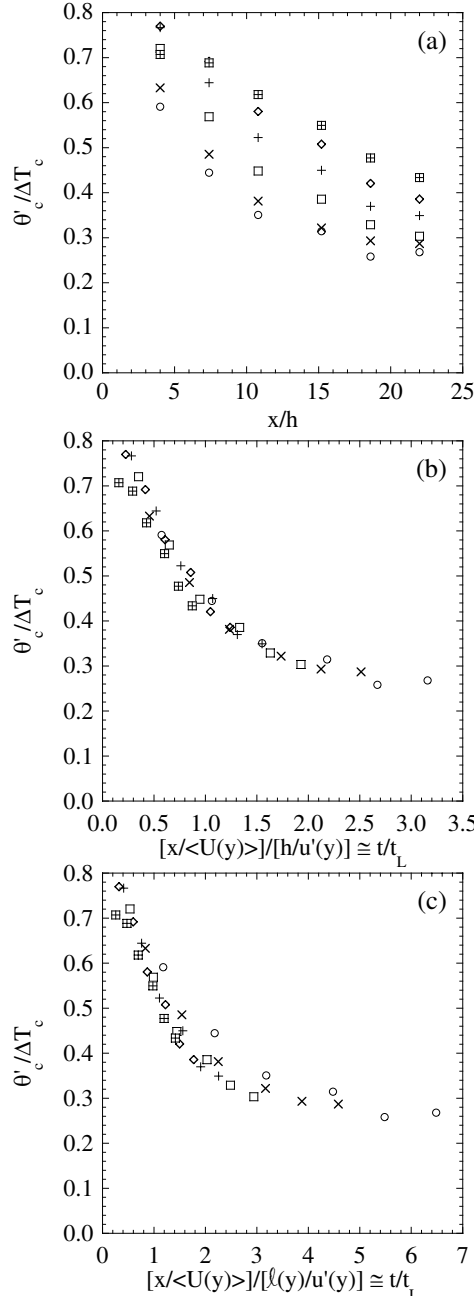


Figure 4.19: The downstream development of the ratio of the centreline root-mean-square temperature fluctuation to the peak (i.e. centreline) mean temperature excess for six different wall-normal positions. In (a), an Eulerian non-dimensionalization is used. In (b) and (c), a Lagrangian non-dimensionalization is employed. The symbols denote different wall-normal positions: \circ : $y/h = 0.10$, \times : $y/h = 0.17$, \square : $y/h = 0.33$, $+$: $y/h = 0.50$, \diamond : $y/h = 0.67$, \boxtimes : $y/h = 1.0$.

Tavoularis (1989) is the “best-mixed” of the three, followed by the present lateral dispersion in fully developed channel flow and then the grid turbulence studied by Warhaft (1984). In Karnik & Tavoularis (1989), the presence of the mean flow shear (which is aligned in the direction of the scalar dispersion) enhances the mixing of the temperature fluctuations. Moreover, due to the nature of homogeneous turbulent shear flow, both the magnitude of the velocity fluctuations *and* the turbulence intensity increase with downstream position. This serves to further mix the passive scalar. In contrast, the present channel flow has variable shear (albeit in the direction normal to the dispersion) and, given its fully developed nature, exhibits a turbulence intensity that remains constant in the downstream direction. Finally, the grid turbulence studied in Warhaft (1984) is shear-free. Consequently, there is no production of turbulent kinetic energy and the turbulence intensity decays with increasing downstream position. Given the nature of these three flows, there appears to be two cooperative effects that increase the mixedness of the scalar plume: (i) mean-flow shear and (ii) the level of turbulence intensity (which, it is worth noting, are not entirely unrelated, as mean-flow shear leads to production of turbulent kinetic energy). See table 4.6 for a summary of these properties.

A comparison of the mixedness estimates measured herein with those of transverse dispersion is difficult, for the following reason. As noted by Lavertu & Mydlarski (2005) (and others) in both channel flow and boundary layers, the peaks of the r.m.s. profiles (emitted from near-wall sources) drift away from the wall with increasing distance, whereas the peaks of the mean profiles remain relatively fixed downstream of the source. Consequently, calculation of $\theta'_c/\Delta T_c$ may not be sensible when the peaks of the mean and r.m.s. temperature profiles are not aligned. The one exception to this is the case of a source located at the channel centreline (Lavertu & Mydlarski, 2005). Here, due to the symmetry

of this geometry, both the mean and r.m.s. temperature profiles peak at the channel centreline, directly downstream of the line source. However, it has been found (Vrieling & Nieuwstadt, 2003; Lavertu & Mydlarski, 2005) that — due to the even symmetry of the flow at the channel centreline, and the weak variations (in the y -direction) of the statistics of the flow in the vicinity of the centreline — the flow in the centre of the channel, far from the walls, as well as the scalar mixing therein, resembles that in homogeneous flows. Therefore, the values of $\theta'_c/\Delta T_c$ measured for the transverse dispersion emitted from a centreline line source in fully developed channel flow are similar to those measured in a homogeneous, isotropic flow, like that of Warhaft (1984). Given the limitations on calculating $\theta'_c/\Delta T_c$ in flows undergoing transverse dispersion, one can only draw a qualified conclusion regarding the state of the mixedness in lateral and transverse dispersion phenomena because $\theta'_c/\Delta T_c$ can only be reliably calculated for one location in the case of transverse dispersion. At this location, for which the mean-flow shear is zero, the flow resembles homogeneous, isotropic turbulence over a limited region. Therefore, based on this one, limited comparison, it could be concluded that lateral dispersion results in increased mixing, given its lower values of $\theta'_c/\Delta T_c$ (0.5 at $x/h = 18.6$ for $y/h = 1.0$ – see figure 4.19a) versus the asymptotic value of 0.7 measured by Warhaft (1984).

To emphasize the differences between lateral and transverse dispersion, figure 4.20 presents a comparison of the one-dimensional power spectra of the temperature fluctuations measured herein to those observed in Lavertu & Mydlarski (2005). We note that for the data obtained at the channel centreline — i.e. $y/h = 1.0$, or figures 4.20(b) and 4.20(d) — the two spectra are only marginally different. This would suggest that the structure of both the lateral and transverse plumes are quite similar. On the other hand, this does not hold

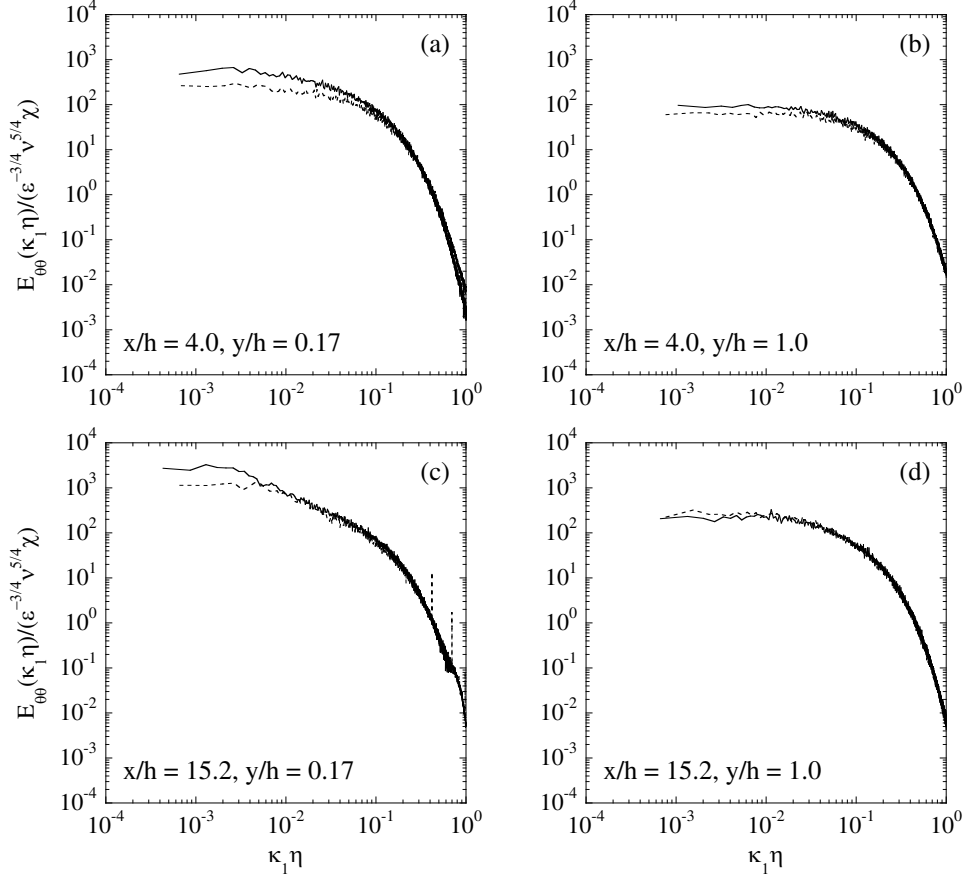


Figure 4.20: Comparison of the one-dimensional spectra of the temperature fluctuations measured herein to those obtained by Lavertu & Mydlarski (2005), non-dimensionalized using Kolmogorov variables. Note that for the data of Lavertu & Mydlarski (2005), the source is located at the transverse location under consideration (i.e. $y_s/h = y/h$). (a) $x/h = 4.0, y/h = 0.17$. (b) $x/h = 4.0, y/h = 1.0$. (c) $x/h = 15.2, y/h = 0.17$. (d) $x/h = 15.2, y/h = 1.0$. Solid line: Present work. Dashed line: Lavertu & Mydlarski (2005).

for the near-wall data — see figures 4.20(a) and 4.20(c) — given the discrepancies observed at large scales. (At small scales, the spectra invariably collapse, given the Kolmogorov normalization employed in these figures.) Furthermore, as one proceeds farther downstream (and approaches the wall), the spectra exhibit a κ_1^{-1} scaling region (see figure 4.20c, for example). Villiermaux, Innocenti & Duplat (2001) suggest that this scaling arises when the scalar is injected into a region of uniform strain (such as the inertial-convective range, or, in the current work, the logarithmic layer). The fact that this scaling range only appears farther downstream (for both the lateral and transverse dispersion) may be due to the requirements of a finite, non-zero development time — on the order of the time scale of the strain — to elapse.

4.2.3 Temperature PDFs

The temperature fluctuations are further studied by means of their PDFs. As alluded to in section 4.2.2, temperature fluctuations are generated by two principal mechanisms: (i) turbulent production due to interactions with the mean temperature gradients, and (ii) turbulent transport (or “flapping”) of the plume by the large eddies. The latter manifests itself as a spike in the PDF, observed at the temperature of the cold fluid outside of the plume.

The downstream evolution of the non-dimensional temperature PDFs is plotted in figure 4.21. Near the wall ($y/h = 0.1$), one observes that the thermal plume is well mixed, as evidenced by the quasi-Gaussian PDFs (present for all the downstream distances except for the $x/h = 4.0$ case, which exhibits a slight bump in the PDF). Moving away from the wall, one observes an increased prominence in the spike at the cold temperature of the fluid for the $x/h = 4.0$ downstream position. Furthermore, one also notices that a similar spike begins to appear for the $x/h = 10.8$ data as well. As mentioned above, this spike indicates that plume flapping is a significant mechanism in

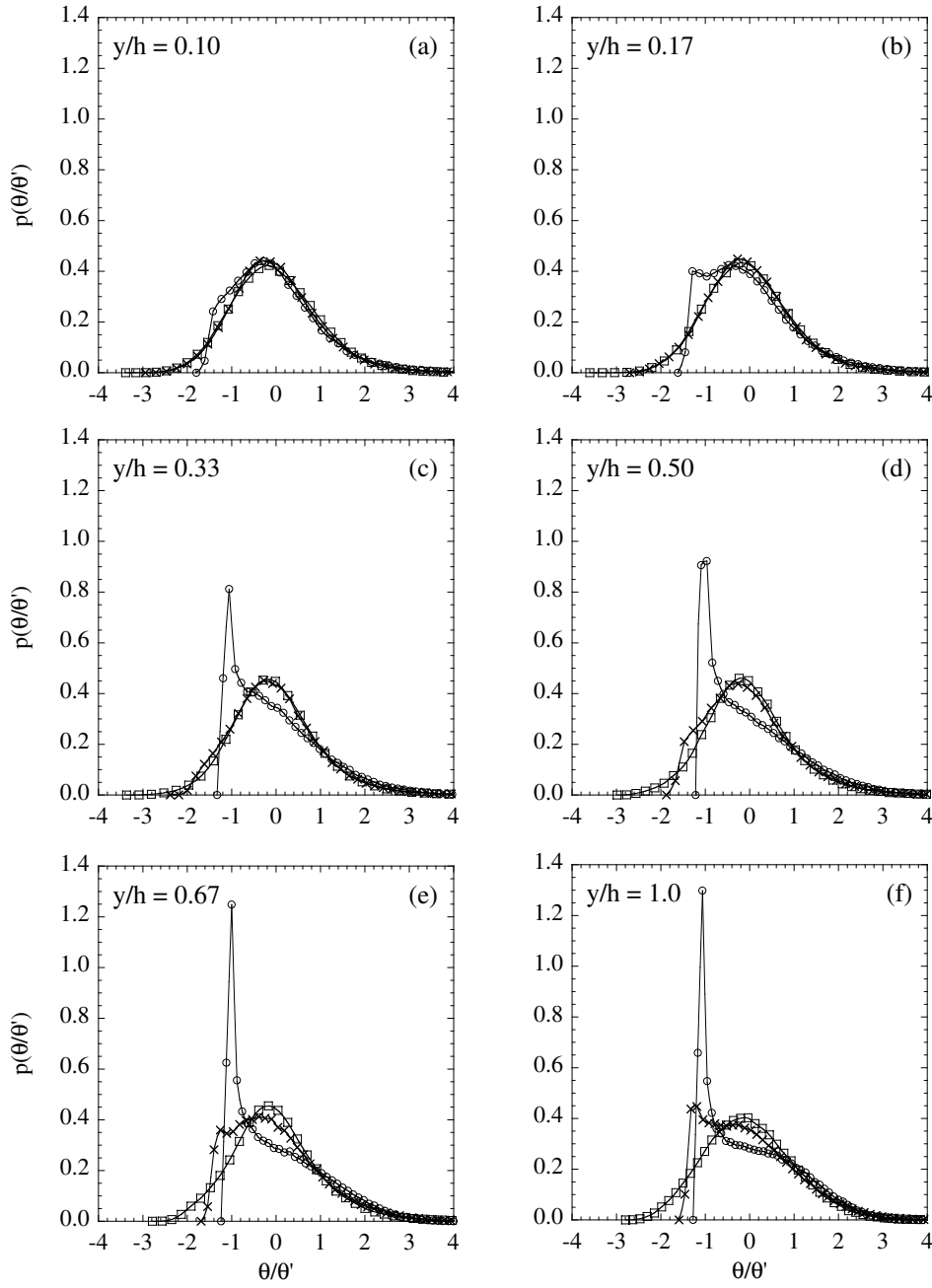


Figure 4.21: Non-dimensionalized probability density functions of the temperature fluctuations at different downstream positions for the six wall-normal elevations. The spanwise position in each figure is behind the source location (i.e. $z/h = 0$). (a) $y/h = 0.10$, (b) $y/h = 0.17$, (c) $y/h = 0.33$, (d) $y/h = 0.50$, (e) $y/h = 0.67$, (f) $y/h = 1.0$. Symbols denote different downstream positions: \circ : $x/h = 4.0$, \times : $x/h = 10.8$, \square : $x/h = 22.0$.

the production of turbulent fluctuations at these locations. Consequently, the plume is better mixed in the near-wall region, as opposed to near the channel centreline. This presumably arises due to the increased turbulence intensity at the wall.

The difference between lateral and transverse dispersion is further elucidated in figure 4.22. It compares the PDFs from a specific case of Lavertu & Mydlarski (2005) (data downstream of a source located at the channel centreline — $y/h = y_s/h = 1.0$) with the most similar case studied herein (i.e. $y/h = 1.0, z/h = 0$). The PDFs therein indicate that, close to the source location, the dispersion is not especially sensitive to the orientation of the line source. Consider, for example, figure 4.22(a), which plots the PDFs at a downstream location of $x/h = 4.0$. The two curves are quite similar, indicating that the statistical distribution of the temperature fluctuations is similar for both line source orientations. Far downstream of the source location (figure 4.22c), both curves appear to have a quasi-Gaussian shape, indicative of a well-mixed scalar field. (However, note that the data of Lavertu & Mydlarski (2005) appear to be more skewed, and therefore somewhat less well mixed, than the present data.) Consequently, the asymptotic behaviours of both the lateral and transverse plume dispersion appears to be similar in the limits of small and large x/h . For intermediate distances, the PDFs suggest that the plume emitted from a wall-normal line source is better mixed than the corresponding plume emitted from a spanwise line source. Thus, one could hypothesize that the lateral mixing may be more rapid than the transverse mixing, if one were considering the three-dimensional dispersion of a plume emanating from a point source (at least, at this centreline source location). This hypothesis is also validated by the lower values of $\theta'_c/\Delta T_c$ (i.e. increased mixedness) for

the lateral dispersion as compared to the transverse ones, as discussed earlier. Given the spikes present in both PDFs (see figure 4.22b), plume flapping remains a dominant mechanism for the generation of the scalar fluctuations. However, the bounded nature of the dispersion in Lavertu & Mydlarski (2005) inhibits plume flapping, and thus hinders the mixing in the transverse plume.

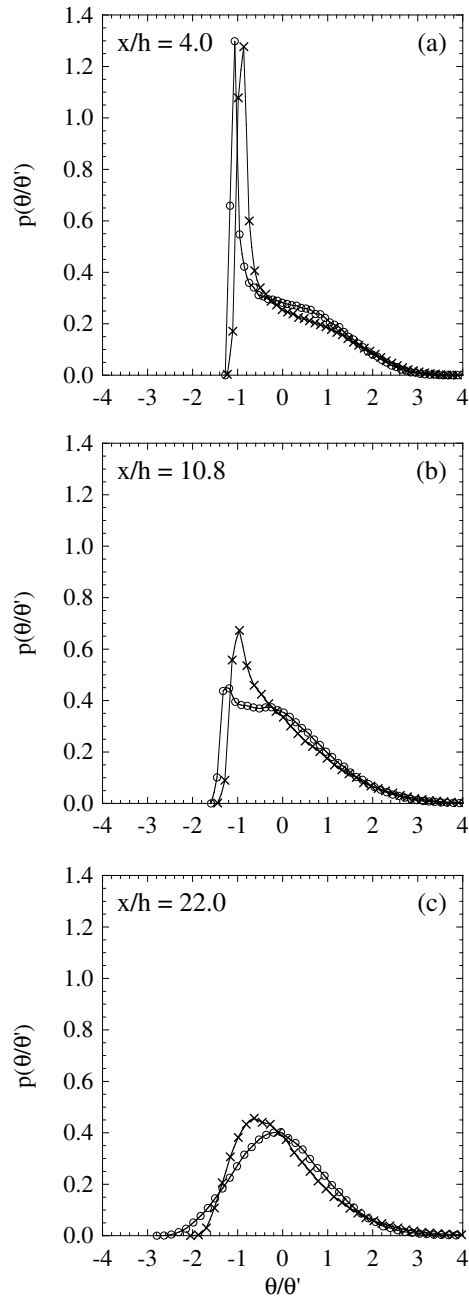


Figure 4.22: Comparison of the non-dimensional probability density functions measured herein with those obtained in Lavertu & Mydlarski (2005) for three of the downstream positions. (a) $x/h = 4.0$, (b) $x/h = 10.8$, (c) $x/h = 22.0$. Symbols denote different experiments: \circ : Present work, $y/h = 1.0$, $z/h = 0$. \times : Lavertu & Mydlarski (2005), $y_s/h = y/h = 1.0$.

CHAPTER 5

Conclusions

The following chapter is divided into four sections. The first section summarizes the results of the internal intermittency experiment, whereas the second presents the pertinent conclusions from the lateral dispersion measurements. The third section outlines the original contributions of the present study, whereas the fourth section proposes some extensions of the current research, and discusses the potential benefit of the proposed experiments.

5.1 Internal Intermittency Experiment

The influence of the scalar-field boundary conditions on the small-scale statistics of passive scalar increments were experimentally studied in the heated wake of a circular cylinder at a Taylor-microscale Reynolds number of 370. To explicitly isolate the influence of the scalar-field boundary conditions, two independent heat injection mechanisms were employed. However, the hydrodynamic field was identical for both cases. Results pertaining to the (i) high-order passive scalar structure functions (and their inertial-convective-range scaling exponents), (ii) mixed, velocity-temperature sixth-order structure functions, (iii) (non-centered) autocorrelations of the dissipation rate of scalar variance, and (iv) normalized high-order moments of the passive scalar increments were presented.

The second-order passive scalar structure functions obtained using the different scalar injection mechanisms were experimentally indistinguishable in the inertial-convective and dissipative ranges of scales. However, as the structure function order increased, the structure functions began to differ at progressively smaller scales. By eighth-order, the curves were different at almost all

scales. This result indicates that the effects of internal intermittency permeate to the small scales at the highest orders. An analysis of the (inertial-convective range) structure function scaling exponents showed that the structure function scaling exponents obtained using the different scalar-field boundary conditions (i) are significantly different from each other at high orders, and (ii) increasingly deviate from each other with increasing structure function order. This result is consistent with those obtained in the direct numerical simulation of Watanabe & Gotoh (2006), who also observed that different scalar sources yield different inertial-convective range scaling exponents.

It was observed that the effects of the scalar-field boundary conditions were small and confined to the largest scales for low-order structure functions. However, the differences in the two scalar fields became more pronounced with increasing structure function order, with the scalar field generated by the mandoline exhibiting smaller inertial-convective-range scaling exponents. To further study these effects, and, more precisely, determine whether this result was truly indicative of the relative levels of the internal intermittency of the passive scalar fields examined herein, other statistics were considered.

The inertial-convective range scaling exponents of both the mixed, sixth-order structure functions and the autocorrelations of the dissipation rate of scalar variance were employed to obtain estimates of the intermittency exponent of the flows under consideration herein. Contrary to the result obtained from the passive scalar structure function scaling exponents, these latter two measures indicated that the scalar fields generated by the mandoline and by heating the cylinder have experimentally indistinguishable degrees of internal intermittency. Furthermore, the inertial-convective scaling ranges of these two quantities also exhibited a lack of dependence/sensitivity to the large-scales of the flow. Whereas it has been shown that the (i) inertial-convective-range

structure function scaling exponents are clearly affected by the large-scale features of the passive scalar field at high orders, and (ii) autocorrelations of the dissipation rate of scalar variance and the mixed sixth-order structure functions are significantly less sensitive to the scalar-field boundary conditions, the question of which, if any, of these measures is the “correct” estimator of passive scalar intermittency remains open.

In addition to the statistics described above, the kurtosis structure functions of the passive scalar increment were examined. For large separations, the high-order moments asymptoted to their respective large-scale, quasi-Gaussian values. However, at small scales, the moments deviated significantly from the Gaussian prediction, due to internal intermittency. Moreover, it was noted that the high-order moments of the mandoline data reached their large-scale, quasi-Gaussian values at smaller values of r/η_θ than their heated cylinder counterparts, due to the smaller scalar integral length scale of the mandoline-generated temperature field. Consequently, the inertial-convective-range, power-law slopes of the kurtosis structure functions for the mandoline data are steeper (i.e. have smaller/more negative scaling exponents) than the heated cylinder data. Since the slopes of the high-order moment curves are directly proportional to the structure function scaling exponents, it can be concluded that the scaling exponents for the mandoline experiment are anomalously smaller than those obtained from the heated cylinder experiment because of the smaller inertial-convective range in the former experiment, and are therefore not solely a reflection of a more intermittent passive scalar field, but remain affected by the smaller Péclet number of the scalar field generated by the mandoline.

In light of this result, the mixed, sixth-order structure functions described above were also non-dimensionalized using the variances of differences of the

velocity and scalar fields to obtain a mixed “super-kurtosis” structure function (analogous to the normalized high-order moments discussed in the previous paragraph). Plotting the mixed super-kurtosis structure functions revealed that the data obtained using the different scalar-field boundary conditions achieve their respective, large-scale asymptotic values at roughly the same separation, unlike the passive scalar structure functions.

The current results suggest that a direct relationship between the internal intermittency of the turbulent passive scalar and the inertial-convective-range scaling exponents of the high-order passive scalar structure functions can only exist when the inertial-convective ranges of the scalar fields are of the same width (or, alternately, infinite). Such a result is also consistent with previous works that have shown that large-scale effects such as non-stationarity (Danaila *et al.*, 1999) or production (Danaila & Mydlarski, 2001) contaminate the inertial-convective-range statistics. While the two flows examined herein have the same Reynolds number, their Péclet numbers are different because of the different thermal integral length scales associated with the different heat injection mechanisms. Consequently, the flows examined herein have the same inertial ranges, but different inertial-convective ranges.

To isolate the influence of the different scalar integral length scales, the kurtosis structure functions were plotted versus a Péclet-number-compensated separation. In doing so, one observes that the collapse of the kurtosis structure functions obtained using the different scalar-field boundary conditions improves at small-scales.

Finally, the effects of large-scale anisotropy were examined by (i) offsetting, and (ii) normalizing the kurtosis structure functions by their respective, quasi-Gaussian, asymptotic values. (Note that the former preserves the interpretation of the kurtosis, whereas the latter does not.) Unfortunately,

no conclusions pertaining to the passive scalar internal intermittency can be drawn from the offset kurtosis structure functions, since the magnitude of these statistics alone may be dependent upon large-scale, flow-dependent features. The normalized kurtosis structure functions exhibited a reasonable collapse at both large and small scales, and diverge only at intermediate scales (with the magnitude of the divergence increasing with structure function order, and the heated cylinder flow taking on larger values). Since the observed difference in the kurtosis structure functions permeates to smaller scales with increasing structure function order, it is not unreasonable to assume that the data will no longer collapse at small scales at even higher orders.

5.2 Lateral Dispersion Experiment

The lateral dispersion of a passive scalar injected from a concentrated line source in fully developed, high-aspect-ratio turbulent channel flow was studied. Results pertaining to the mean and fluctuating temperature field were presented, including spectra and PDFs. Six wall-normal positions ($y/h = 0.10, 0.17, 0.33, 0.5, 0.67$ and 1.0) were considered at a Reynolds number of $Re = 10200$. The downstream evolution of the scalar statistics was presented for the range $4.0 \leq x/h \leq 22.0$.

The mean temperature excess profiles were well described by Gaussian distributions with peaks that occurred downstream of the source. Consistent with work in homogeneous turbulence (presumably due to the unbounded nature of the dispersion in the lateral direction), the downstream evolution of the centreline (peak) mean temperature excess was found to obey a power law with an exponent, m , falling in the range $-0.78 \leq m \leq -0.68$. Moreover, the exponents exhibited a non-monotonic trend with transverse position, with the slowest decay at $y/h \approx 0.5$. On the other hand, the transverse evolution of the

centreline mean temperature excess was less dependent on the downstream position. Moreover, the decay of the mean temperature excess was much slower in the transverse direction (when compared to the downstream development). The half-widths of the lateral profiles are shown to be larger in the near-wall region and narrower at the centreline. In contrast to the grid turbulence work of Warhaft (1984), the downstream evolution of the half-widths was shown to obey a power law evolution, with exponents in the range $0.55 \leq n \leq 0.76$ that increase monotonically with distance from the wall. This difference suggests that the evolution of n with y/h observed herein cannot be solely attributed to differences in the turbulence intensity at the source location. The transverse development of the half-width of the mean temperature profiles was found to become independent of the wall-normal position far downstream from the source. Finally, the use of a Lagrangian non-dimensionalization of the downstream coordinate collapsed the downstream evolution of the centreline (peak) mean temperature excess onto a single curve. However, the same does not hold for the half-width data. To collapse the half-width data, a second Lagrangian non-dimensionalization, which makes use of the local integral length scale of the turbulence (ℓ) instead of the channel half-width (h), was proposed. By making use of a variable length scale, i.e. $\ell(y)$, the new Lagrangian normalization successfully collapsed both the peak mean temperature excess as well as the half-width data.

In contrast to the mean temperature profiles, the r.m.s. temperature fluctuation profiles were non-Gaussian. Furthermore, the profiles evolved from single- to double-peaked profiles with increasing downstream distance (and as the wall is approached). The centreline r.m.s. temperature fluctuation was found to exhibit a power law decay with exponents $-1.22 \leq m \leq -1.06$ for the various wall-normal positions. The exponents were relatively constant for the

$y/h = 0.10, 0.17$ and 0.33 wall-normal positions and then decreased with increasing y/h . The downstream evolution of the half-width of the r.m.s. profiles was described by a power law evolution with exponents that increase monotonically from $n = 0.59$ near the wall ($y/h = 0.10$) to $n = 0.76$ at the channel centreline ($y/h = 1.0$). Akin to the mean temperature field, the transverse evolution of the half-width of the r.m.s. profiles also indicated that the width of the plume became independent of the wall-normal position at downstream positions far from the source. Once again, consistent with the observations of the mean temperature field, the downstream evolution data of the centreline r.m.s. temperature fluctuation (and the half-widths of the r.m.s. temperature profiles) could be described by a single curve if the downstream coordinate was non-dimensionalized using a quasi-Lagrangian non-dimensionalization (where ℓ/u' is used to estimate the local Lagrangian time scale).

The mixedness of the flow was studied by examining the ratio of the centreline r.m.s. temperature fluctuation to the centreline mean temperature excess. When the downstream coordinate was non-dimensionalized by the channel half-width (h), the data revealed that the mixedness of the flow improved with increasing downstream position and as the wall was approached. Furthermore, using a quasi-Lagrangian non-dimensionalization of the downstream distance, one obtained a collapse of the data from the six different wall-normal distances, revealing a monotonic decay of the ratio $\theta'_c/\Delta T_c$ from a value of 0.8 down to roughly 0.3 over the range of downstream distances explored in the current research. No local maxima were observed. The current results were compared to those obtained in grid turbulence by Warhaft (1984), as well as the homogeneous shear flow results of Karnik & Tavoularis (1989), revealing a difference in the asymptotic values of the ratio $\theta'_c/\Delta T_c$. The shear flow of Karnik & Tavoularis (1989) was the best mixed, followed

by the current channel flow, and finally, the homogeneous, isotropic turbulence described in Warhaft (1984). Moreover, the comparison suggested that there exist two cooperative effects that determine the mixedness of the plume: the mean-flow shear and the turbulence intensity, which are different, but not entirely independent, as higher shear results in larger turbulent intensities.

One-dimensional spectra of the temperature fluctuations were measured and compared to those obtained in the transverse dispersion study of Lavertu & Mydlarski (2005). The spectra revealed that, far from the walls, the structure of the lateral and transverse plumes is quite similar. Moreover, the near-wall spectra exhibited a κ_1^{-1} scaling region (at large downstream distances), consistent with a scalar field exposed to a constant strain rate (as described in Villermaux *et al.* (2001)).

The PDFs showed that mixing was enhanced (i) farther downstream and (ii) closer to the wall. The latter is presumably due to the increased turbulence intensity at the wall, while the former is due to the increased advection time. Plume flapping (as inferred from the presence of a spike in the PDFs corresponding to the cold fluid temperature) was the dominant mechanism in the production of temperature fluctuations for all transverse distances at the closest downstream position of $x/h = 4.0$. At $x/h = 10.8$, a transition from a flapping-dominated regime to a turbulent-mixing-dominated regime was observed at roughly $y/h \approx 0.5$. The present PDFs were compared to those obtained by Lavertu & Mydlarski (2005) to ascertain the differences between the mixing in the lateral and transverse directions. Close to the source, the PDFs of the temperature fluctuation presented with similar features. At the farthest downstream position, the PDFs in both experiments approached quasi-Gaussian profiles, suggesting the presence of a well-mixed asymptotic limit for both the lateral and transverse dispersion statistics in the limit of

large downstream distances. However, for the intermediate downstream positions, the PDFs corresponding to the lateral dispersion exhibited better mixing than the transverse dispersion, consistent with the measurements of $\theta'_c/\Delta T_c$. This presumably arises due to the bounded nature of the flow in the wall-normal direction, which stifles the plume growth by hindering the transverse flapping of the plume.

5.3 Contributions of the Present Study

The objective of the current research was to examine the influence of both the velocity- and scalar-field boundary conditions on the passive scalar mixing that occurs within turbulent flows. Consequently, the present study provides insight into both large- and small-scale mixing phenomena within inhomogeneous turbulent flow. The original contributions of the present work are summarized below.

1. The internal intermittency experiment was the first rigorous experimental study of the effect of the (large-scale) scalar-field boundary conditions on the small-scale structure of a turbulent passive scalar field. This was accomplished by means of a logical experiment in which the scalar field injection mechanism was independently varied while expressly maintaining an identical hydrodynamic field. The current research proved that the high-order passive scalar structure function scaling exponents were dependent upon the scalar field boundary conditions, or, more precisely, the Péclet number of the flow under consideration. This explained the results of previous investigations of the inertial-convective-range scaling exponents, which revealed a considerable scatter in their results. The

present work therefore demonstrates that none of the multitudes of previously measured high-order passive scalar structure function scaling exponents can be considered to be the “true,” universal values, as they were all measured/calculated in low- (i.e. finite-) Péclet-number flows.

2. To date, the only other similar work was the numerical simulation of Watanabe & Gotoh (2006). They examined the passive scalar structure function scaling exponents generated by means of a (i) Gaussian, white-in-time scalar source and (ii) uniform mean scalar gradient. Watanabe & Gotoh (2006) observed that the different scalar fields also yielded different scaling exponents. However, unlike the current research, Watanabe & Gotoh (2006) did not explain the cause of the observed difference in the inertial-convective-range scaling exponents. Consequently, not only does the present work validate the simulations of Watanabe & Gotoh (2006), but it also elucidated the critical influence of the Péclet number on the structure function scaling exponents.
3. Given that (i) the inertial-convective-range scaling exponents of the passive scalar structure functions are frequently employed measures of passive scalar internal intermittency, and (ii) the observed dependency of these scaling exponents on the scalar-field boundary conditions, the present work examined two additional measures of internal intermittency. In particular, it studied the mixed, velocity-temperature sixth-order structure functions and the non-centered autocorrelations of the dissipation rate of scalar variance, to verify whether these measures were similarly affected. Unlike the structure function scaling exponents, it was determined that the mixed structure functions and non-centered autocorrelations were less sensitive to the scalar-field boundary conditions, i.e. the resulting

intermittency exponents (μ_θ) were experimentally indistinguishable. Although it has been established in the literature that different values of the intermittency exponents could be obtained when using different procedures in their calculation, the present work also reveals for the first time that certain measures are much more sensitive to the scalar field boundary conditions than others.

4. The lateral dispersion experiment examined the mixing that occurs downstream of a concentrated line source. The present work targeted and systematically studied the details of the *lateral* dispersion of both the mean and fluctuating scalar fields in an inhomogeneous turbulent flow resulting from a three-dimensional thermal plume. Because almost all practical environmental and engineering dispersion problems involve three-dimensional mixing phenomena, quantification of the lateral dispersion is especially relevant. Moreover, since the present work was conducted in the same experimental facility as the transverse dispersion experiment of Lavertu & Mydlarski (2005), the current research enabled a comparison of the lateral and transverse dispersion for an inhomogeneous turbulent flow.
5. Distinct differences between the present work and the previous two-dimensional studies, conducted in both homogeneous and inhomogeneous turbulence, were observed. For example, the development of the mean and r.m.s. temperature fluctuations suggested that the lateral dispersion more closely resembled the transverse dispersion observed in the mixing studies conducted in homogeneous turbulence (as opposed to those results obtained from inhomogeneous flows). This observation was attributed to the unbounded nature of the lateral plume (whereas the transverse plume is bounded due to the presence of the channel walls).

6. Finally, the present work highlighted the importance of using a Lagrangian normalization to collapse the lateral dispersion data obtained for the different wall-normal positions. Unlike the previous transverse dispersion studies, the Lagrangian normalization collapsed both the mean and r.m.s. temperature data, as well as the intensity of the scalar fluctuations. Moreover, examining the intensity of the temperature fluctuations by means of a Lagrangian normalization revealed its asymptotic limit — a measure that is frequently employed to characterize the mixedness of the flow. Furthermore, by comparing the asymptotic value observed herein to those available in the literature, the present work elucidated the influence of the mean-flow shear and the turbulence intensity in determining the mixedness of the passive scalar field.

5.4 Extensions of the Present Work

One of the primary conclusions of the internal intermittency experiment was that the observed discrepancy in the passive scalar structure function scaling exponents exhibited a marked dependency on the large-scale features of the scalar field, or, alternately, the Péclet numbers of the flows under consideration. However, in the present work, the scalar fields were injected such that the scalar integral length scales of the flow, and thus their Péclet numbers, were notably different. It would be of interest to repeat the current experiment using two distinct scalar sources with the same scalar integral length scale. For example, changing the downstream position of the mandoline relative to the cylinder would yield different scalar integral length scales — see Beaulac & Mydlarski (2004). Unfortunately, given the constraints of the experimental facility employed herein, the scalar integral length scales could not be matched using the current apparatus. Nevertheless, an experiment with two distinct scalar injection methods resulting in the same values of the scalar

integral length scale could provide additional insight into the passive scalar structure function scaling exponents, as well as the internal intermittency of the passive scalar field. Such an experiment would provide further insight into how the inertial-convective-range scaling exponents are contaminated by the large-scale boundary conditions and whether they are indeed representative of the internal intermittency of the turbulent passive scalar.

Additional insight into the structure of the passive scalar field can also be achieved through the use of multi-point statistics. Three-points statistics have been obtained in homogeneous, isotropic turbulence (Mydlarski *et al.*, 1998), which examined the turbulent passive scalar using three-point autocorrelations of the temperature fluctuation. Such measurements reveal the structure of the scalar fronts that are responsible for passive scalar anisotropies (as opposed to two-point statistics, which only provide information about their scaling). Consequently, such correlations could highlight differences in the structures of the small-scale passive scalar fields obtained using the different boundary conditions, and therefore provide a quantitative measure of the internal intermittency of the passive scalar field.

The lateral dispersion measurements described herein revealed that the effects of the mean-flow shear and the turbulence intensity played a significant role in passive scalar mixing. However, all of the data presented in the present work was obtained at wall-source positions located within the turbulent (outer) core of the flow. It would be of interest to examine the lateral dispersion that occurs in the near-wall region of the flow, since the dynamics of the near-wall flow region are different from the core region. Moreover, the effects of the mean-flow shear dominate the fluid dynamics in this region. Consequently, such measurements could provide further insight into the influence of the mean-flow shear on the mixing of the turbulent passive scalar.

In addition, the mixing downstream of multiple sources is also of interest to many investigators. While such experiments have already been conducted in both homogeneous and inhomogeneous flows, it would be of interest to determine whether the observed similarities and differences between the present work and the results obtained in homogeneous flows can be extended to the mixing of multiple sources. Given the inherent three-dimensionality of the current experimental configuration, there is no *a priori* reason to assume that the proposed experiments will resemble the two-dimensional mixing experiments presented in the literature. Such results would therefore (i) highlight the influence of the inhomogeneity of the velocity field on the mixing that occurs downstream of multiple scalar sources, and (ii) provide insight as to how to accelerate (or delay) the mixing of multiple scalars that are transported by an inhomogeneous flow.

APPENDIX A

Error and Uncertainty Analysis

The current appendix examines the uncertainty of the various velocity and temperature statistics presented in the current research. Tavoularis (2005) argues that the total measurement uncertainty can be divided into two distinct classes: (i) bias error and (ii) precision error. Bias error, denoted herein using b , is typically assumed to be systematic, and is, consequently, representative of the accuracy of the measurement. Precision error (denoted using p), as its name implies, is a measure of the precision, or repeatability of the measurement. Given the difficulty associated with determining the bias error, the present analysis assumes that the bias error is equal to the manufacturer-specified accuracy (if available). The precision error, on the other hand, can be estimated in one of two ways.

For the purposes of the following analysis, it is assumed that each source of precision error can be classified in one of two manners.

1. Given a series of N measurements, with a mean μ and a standard deviation of σ , Tavoularis (2005) argues that the appropriate expression for the precision error of a given measurement is:

$$p = \frac{2\sigma}{\sqrt{N}}.$$

Such measurements will be referred to herein as “Type 1” measurements.

2. Given a single measurement, obtained using an instrument with a precision of σ , it is assumed that the error is uniformly distributed¹ between the endpoints $\pm\sigma$, such that:

$$p = \frac{\sigma}{\sqrt{3}}.$$

This type of measurement will be denoted as a “Type 2” measurement. Once the precision and bias errors have been estimated from each source of uncertainty, the total measurement uncertainty, u , can be calculated using the expression presented in Tavoularis (2005), namely:

$$u = \sqrt{\sum_i b_i^2 + \sum_i p_i^2}.$$

In the following sections, the uncertainties arising from both the temperature and velocity measurements presented herein will be analyzed individually, followed by a discussion of the uncertainty of the various turbulent statistics presented herein.

A.1 Uncertainty of the Temperature Measurements

Since the calibration employed herein for the hot-wire sensor (U) relies upon the temperature measurement (T) from the cold-wire sensor, the present analysis begins by examining the uncertainty in the temperature measurements presented herein. The cold-wire sensor is calibrated in a heated, isothermal, laminar jet at a constant velocity (typical of the velocity encountered during the experiment). The jet temperature is measured using an unshielded, type E thermocouple, connected to a digital display (accurate to 0.1 K). As described in Section 2.3.2, the relationship between the cold-wire thermometer output

¹ See, for example, the NIST/SEMATECH e-Handbook of Statistical Methods, <http://www.itl.nist.gov/div898/handbook/>.

voltage (E) and the flow temperature is linear over small temperature increments, such as those encountered in this work. The output of the cold-wire thermometer is digitized using a 16-bit analog-to-digital (A-D) converter (with a maximum voltage span of ± 5 V), and both the average and root-mean-square (RMS) voltage are calculated (using 256 samples). In addition, the error associated with the linear curve fit is estimated by comparing the temperature values predicted using the curve fit to the measured temperature values. Finally, note that the error analysis below applies strictly to the absolute temperature measurements (and not the temperature differences, which will be expounded upon below). Table A.1 below summarizes the various sources of error for the temperature measurements.

Using the first two lines of table A.1, the total uncertainty of the voltage measurements is :

$$u_E = 3.614 \text{ mV}.$$

Clearly, the accuracy of the A-D board is the dominant factor in this calculation. However, one must incorporate the error of the voltage measurement into the total error for the temperature measurement, such that:

$$u_T = \sqrt{\sum_i b_i^2 + \sum_i p_i^2 + \left(\frac{\partial T}{\partial E} u_E\right)^2}.$$

Using the values listed in table A.1, the total uncertainty of the absolute temperature measurement is:

$$u_T = 1.71 \text{ K}.$$

Once again, the accuracy of the thermocouple plays a significant role in determining the total uncertainty of the total, absolute temperature.

Table A.1: Summary of the various sources of error for the absolute temperature measurements.

Error	Description	Type	σ	b_i or p_i
Bias	Accuracy of the A-D converter	N/A	N/A	± 3.613 mV
Precision	Precision of the A-D converter	Type 2	0.153 mV	± 0.0881 mV
Bias	Accuracy of the Type E thermocouple	N/A	N/A	± 1.7 K
Bias	Error in temperature calibration curve	N/A	N/A	± 0.142 K

A.2 Uncertainty of the Velocity Measurements

The calibration of the hot-wire sensor is also conducted in an isothermal, laminar jet. However, the calibration is repeated for a number of different flow temperatures, to obtain the temperature-dependent coefficients described in Section 2.3.1. Consequently, the uncertainty of the temperature measurement displayed above must be taken into account. Moreover, unlike the temperature calibration, in which the temperature was measured directly, the jet velocity must be inferred from a differential pressure measurement (as well as taking into account the measurement of the ambient pressure and flow temperature). The ambient pressure is measured using a mercury barometer, which features a Vernier scale accurate to 0.1 mm Hg, whereas the flow temperature is once again measured using the type E thermocouple and digital display configuration described above. Table A.2 summarizes the various sources of error in the instruments used to calculate the flow velocity.

Once again, the total uncertainty of the voltage and cold-wire temperature measurements are $u_E = 3.614$ mV and $u_T = 1.71$ K, respectively. To determine the uncertainty of the velocity measured during the calibration procedure, one must determine the uncertainty of the differential pressure measurement, as well as the ambient pressure and flow temperature measurements, all of which can be obtained from the data in table A.2.

The differential pressure transducer produces an output voltage of 0–10 V for a given input pressure difference of 0 – 100 mm Hg. Assuming that the voltage response is linear, the total uncertainty in the differential pressure measurement can be estimated using that of the voltage measurement, namely:

$$u_{\Delta P} = \sqrt{\left(\frac{\partial(\Delta P)}{\partial E}u_E\right)^2},$$

Table A.2: Summary of the various sources of error for the absolute velocity measurements.

Error	Description	Type	σ	b_i or p_i
Bias	Accuracy of the A-D converter	N/A	N/A	± 3.613 mV
Precision	Precision of the A-D converter	Type 2	0.153 mV	± 0.0881 mV
Bias	Accuracy of the Type E thermocouple	N/A	N/A	± 1.7 K
Precision	Precision of thermocouple reading	Type 2	0.1 K	± 0.06 K
Precision	Error in ambient pressure measurement	Type 2	0.1 mm Hg	± 0.06 mm Hg
Bias	Error in velocity calibration curve	N/A	N/A	± 0.0917 m s ⁻¹

which yields a value of 0.03614 mm Hg. Meanwhile, the total error associated with the ambient pressure measurement arises strictly from the precision error, such that $u_P = 0.06$ mm Hg. Finally, the uncertainty of the flow temperature is determined by both the accuracy and precision of the thermocouple. Consequently, the total uncertainty in the flow temperature is $u_T = 1.70$ K.

Given the three measurements listed above, namely the differential pressure, ambient pressure and flow temperature, the flow velocity can be calculated using the isentropic relations for compressible flow. Using these equations, the partial derivatives $\partial U/\partial(\Delta P)$, $\partial U/\partial P$, and $\partial U/\partial T$ can be computed, and the uncertainty of the calculated velocity obtained. Using the expression:

$$u_U = \sqrt{\left(\frac{\partial U}{\partial(\Delta P)}u_{\Delta P}\right)^2 + \left(\frac{\partial U}{\partial P}u_P\right)^2 + \left(\frac{\partial U}{\partial T}u_T\right)^2},$$

the total uncertainty is $u_U = 0.0752$ m s⁻¹. Finally, one must also take into account the uncertainty of the cold-wire temperature measurement (as described above), along with error associated with the velocity calibration curve fit — see table A.2 — and the measured output voltage of the hot-wire. Consequently, the total uncertainty in the absolute velocity becomes:

$$u_U = 0.28 \text{ m s}^{-1}.$$

Note that it is the uncertainty of the measured temperature that dominates the uncertainty of the velocity measurement. Therefore, improving the accuracy of the cold-wire thermometer would yield a reduced error estimate for the velocity field.

A.3 Uncertainty of the Turbulent Statistics

While the previous two sections provide error estimates of the absolute temperature and velocity measurements, one must discuss how the uncertainty

estimates outlined above apply to the various turbulent statistics examined in the present work. One important distinction is that the majority of the statistics presented herein are computed using velocity and/or temperature *differences*. Tavoularis (2005) argues that when differences are measured using the same instrument, one may assume that the bias error will be canceled out by the subtraction. Therefore, the exercise outlined above is repeated, this time setting all of the sources of bias error to zero. In doing so, one obtains the following uncertainty estimates for the measured velocity and temperature differences: $u_{\Delta U} = 0.0042 \text{ m s}^{-1}$ and $u_{\Delta T} = 0.058 \text{ K}$.

Note that the previous estimate of the uncertainty in the temperature difference is in fact smaller. Given the linear relationship between the cold-wire thermometer output voltage and the flow temperature, the temperature difference is simply the voltage difference multiplied by a constant value, which cancels out when appropriately non-dimensionalized. Therefore, the uncertainty of the temperature difference is given by the minimum voltage resolution of the A-D converter (i.e. 0.0881 mV), multiplied by that same constant value. This yields an uncertainty value of

$$u_{\Delta T} = 0.00016 \text{ K}$$

for the temperature differences only. When compared to the root-mean-square temperatures observed herein — particularly, those of the internal intermittency experiment, see table 4.1 — the temperature difference measurements presented herein are accurate to approximately 1%. Although the error associated with the n^{th} -order moments of the temperature difference (for a given separation) will therefore be equal to 1.01^n , it is not clear how to theoretically estimate the uncertainty in the inertial-convective-range slopes of the n^{th} -order structure functions (which consist of the high-order moments of the

temperature difference plotted as a function of their separation). However, the precision error of the slopes was estimated in table 4.2, by making repeated measurements of the slopes in multiple, distinct experiments.

A.4 Probe Spatial and Temporal Resolution Errors

One of the final sources of error to examine in the present work are those associated with the spatial and temporal resolution of the sensors. Both the hot- and cold-wire sensors are etched to reveal a sensing element roughly 0.5 mm in length. Therefore, both sensors will have roughly the same spatial resolution. However, while the temporal resolution of the hot-wire is determined principally by the electronics of the hot-wire anemometer, the diameter of the cold-wire plays a crucial role in determining its temporal resolution. In the present work, the -3 dB point of the frequency response of the cold-wire is typically 7 kHz.

Of the two experiments conducted herein, the spatial and temporal resolution of the cold-wire sensor is of greater importance to the internal intermittency experiment, since both the large- and small-scale passive scalar fields are examined. (By contrast, the lateral dispersion experiment examines only the large-scale features of the temperature field.) Of critical importance in the internal intermittency experiment is the inertial-convective-range scaling of a variety of turbulent statistics. Consequently, one must establish whether the cold-wires employed herein can sufficiently resolve the inertial scaling region. In the present work, it was determined that the lower limit of the inertial-convective range occurs at $r/\eta_\theta = 30$, or $r = 5.7$ mm. The frequency associated with an eddy of this size can be estimated as $f = \langle U \rangle / (2\pi r)$, which yields a value of roughly 200 Hz. Therefore, given these values, the spatial and temporal resolution of the cold-wire sensor are more than sufficient for resolving the entire inertial-convective range of scales.

REFERENCES

- ANAND, M. S. & POPE, S. B. 1985 Diffusion behind a line source in grid turbulence. In *Turbulent Shear Flows* (ed. L. J. S. Bradbury, F. Durst, B. E. Launder, F. W. Schmidt & J. H. Whitelaw), *Turbulent Shear Flows*, vol. 4, pp. 46–61. Springer.
- ANSELMET, F., ANTONIA, R. A. & DANAILA, L. 2001 Turbulent flows and intermittency in laboratory experiments. *Planet. Space Sci.* **49**, 1177–1191.
- ANSELMET, F., GAGNE, Y., HOPFINGER, E. J. & ANTONIA, R. A. 1984 High-order velocity structure functions in turbulent shear flows. *J. Fluid Mech.* **140**, 63–89.
- ANTONIA, R. A., CHAMBERS, A. J., BRITZ, D. & BROWNE, L. W. B. 1986 Organized structures in a turbulent plane jet: topology and contribution to momentum and heat transport. *J. Fluid Mech.* **172**, 211–229.
- ANTONIA, R. A., HOPFINGER, E. J., GAGNE, Y. & ANSELMET, F. 1984 Temperature structure functions in turbulent shear flows. *Phys. Rev. A* **30**, 2704–2707.
- ANTONIA, R. A., SATYAPRAKASH, B. R. & CHAMBERS, A. J. 1982 Reynolds number dependence of velocity structure functions in turbulent shear flows. *Phys. Fluids* **25**, 29–37.
- ANTONIA, R. A. & VAN ATTA, C. W. 1978 Structure functions of temperature fluctuations in turbulent shear flows. *J. Fluid Mech.* **84**, 561–580.
- ARNEODO, A., BAUDET, C., BELIN, F., BENZI, R., CASTAING, B., CHABAUD, B., CHAVARRIA, R., CILIBERTO, S., CAMUSSI, R., CHILLÀ,

- F., DUBRULLE, B., GAGNE, Y., HEBRAL, B., HERWEIJER, J., MARC-HAND, M., MAURER, J., MUZY, J. F., NAERT, A., NOULLEZ, A., PEINKE, J., ROUX, F., TABELING, P., VAN DE WATER, W. & WILLAIME, H. 1996 Structure functions in turbulence, in various flow configurations, at reynolds number between 30 and 5000, using extended self-similarity. *Europhys. Lett.* **34**, 411.
- BAKOSI, J., FRANZESE, P. & BOYBEYI, Z. 2007 Probability density function modeling of scalar mixing from concentrated sources in turbulent channel flow. *Phys. Fluids* **19**, 115106.
- BEAULAC, S. & MYDLARSKI, L. 2004 Dependence on the initial conditions of scalar mixing in the turbulent wake of a circular cylinder. *Phys. Fluids* **16**, 3161–3172.
- BELIN, F., TABELING, P. & WILLAIME, H. 1996 Exponents of the structure functions in a low temperature helium experiment. *Physica D* **93**, 52–63.
- BENZI, R., CILIBERTO, S., BAUDET, C. & RUIZ CHAVARRIA, G. 1995 On the scaling of three-dimensional homogeneous and isotropic turbulence. *Physica D* **80**, 385–398.
- BENZI, R., CILIBERTO, S., TRIPICCIONE, R., BAUDET, C., MASSAIOLI, F. & SUCCI, S. 1993 Extended self-similarity in turbulent flows. *Phys. Rev. E* **48**, R29–R32.
- BERAJEKLIAN, A. & MYDLARSKI, L. 2011 Simultaneous velocity-temperature measurements in the heated wake of a cylinder with implications for the modeling of turbulent passive scalars. *Phys. Fluids* **23**, 055107.
- BOPPANA, V. B. L., XIE, Z-T. & CASTRO, I. P. 2012 Large-eddy simulation of dispersion from line sources in a turbulent channel flow. *Flow Turbul. Combust.* **88**, 311–342.
- BORATAV, O. N. & PELZ, R. B. 1997 Structures and structure functions in

- the inertial range of turbulence. *Phys. Fluids* **9**, 1400–1415.
- BORATAV, O. N. & PELZ, R. B. 1998 Coupling between anomalous velocity and passive scalar increments in turbulence. *Phys. Fluids* **10**, 2122–2124.
- BRETHOUWER, G., BOERSMA, B. J., POURQUIÉ, M. B. J. M. & NIEUWSTADT, F. T. M. 1999 Direct numerical simulation of turbulent mixing of a passive scalar in pipe flow. *Eur. J. Mech. B/Fluids* **18**, 739–756.
- BROWNE, L. W. B. & ANTONIA, R. A. 1987 The effect of wire length on temperature statistics in a turbulent wake. *Exp. Fluids* **5**, 426–428.
- BRUUN, H. H. 1995 *Hot Wire Anemometry: Principles and Signal Analysis*. Oxford University Press.
- CAMUSSI, R. & VERZICCO, R. 2000 Anomalous scaling exponents and coherent structures in high Re fluid turbulence. *Phys. Fluids* **12**, 676–687.
- CAO, N. Z. & CHEN, S. Y. 1997 An intermittency model for passive-scalar turbulence. *Phys. Fluids* **9**, 1203–1205.
- CHAMBERS, A. J. & ANTONIA, R. A. 1984 Atmospheric estimates of power-law exponents μ and μ_θ . *Boundary Layer Meteorol.* **28** (3-4), 343–352.
- CHEN, S. & CAO, N. 1997 Anomalous scaling and structure instability in three-dimensional passive scalar turbulence. *Phys. Rev. Lett.* **78**, 3459–3462.
- CHEN, S. & KRAICHNAN, R. H. 1998 Simulations of a randomly advected passive scalar field. *Phys. Fluids* **10**, 2867–2884.
- CHEN, S. Y. & CAO, N. Z. 1995 Inertial range scaling in turbulence. *Phys. Rev. E* **52**, R5757–R5759.
- CORRSIN, S. 1951 On the spectrum of isotropic temperature fluctuations in an isotropic turbulence. *J. Appl. Phys.* **22**, 469–473.
- COSTA-PATRY, E. & MYDLARSKI, L. 2008 Mixing of two thermal fields emitted from line sources in turbulent channel flow. *J. Fluid Mech.* **609**, 349–375.

- DANAILA, L., ANSELMET, F., ZHOU, T. & ANTONIA, R. A. 1999 A generalization of Yaglom's equation which accounts for the large-scale forcing in heated decaying turbulence. *J. Fluid Mech.* **391**, 359–372.
- DANAILA, L. & MYDLARSKI, L. 2001 Effect of gradient production on scalar fluctuations in decaying grid turbulence. *Phys. Rev. E* **64**, 016316.
- DIMOTAKIS, P. E. 2005 Turbulent mixing. *Annu. Rev. Fluid Mech.* **37**, 329–356.
- DUPONT, A., EL KABIRI, M. & PARANTHOËN, P. 1985 Dispersion from elevated line source in a turbulent boundary layer. *Intl J. Heat Mass Transfer* **28**, 892–894.
- DURBIN, P. A. 1980 A stochastic model of two-particle dispersion and concentration fluctuations in homogeneous turbulence. *J. Fluid Mech.* **100**, 279–302.
- FACKRELL, J. E. & ROBINS, A. G. 1982 Concentration fluctuations and fluxes in plumes from point sources in a turbulent boundary layer. *J. Fluid Mech.* **117**, 1–26.
- FRENKIEL, F. N. & KLEBANOFF, P. S. 1967 Higher-order correlations in a turbulent field. *Phys. Fluids* **10**, 507–520.
- FREYMUTH, P. 1976 Skewness of temperature derivative in turbulent shear flows. *Phys. Fluids* **19**, 1820–1821.
- FRISCH, U. 1995 *Turbulence: The Legacy of A.N. Kolmogorov*. Cambridge University Press.
- FRISCH, U., SULEM, P-L. & NELKIN, M. 1978 A simple dynamical model of intermittent fully developed turbulence. *J. Fluid Mech.* **87**, 719–736.
- GIBSON, M. M. 1963 Spectra of turbulence in a round jet. *J. Fluid Mech.* **15**, 161–173.
- GIFFORD, F. 1959 Statistical properties of a fluctuating plume dispersion

- model. In *Atmospheric Diffusion and Air Pollution* (ed. F. N. Frenkiel & P. A. Sheppard), pp. 117 – 139. Academic Press, New York.
- GIFFORD, F.A. 1961 Use of routine meteorological observations for estimating atmospheric dispersion. *Nucl. Safety* **2**, 47–51.
- GOTOH, T., FUKAYAMA, D. & NAKANO, T. 2002 Velocity field statistics in homogeneous steady turbulence obtained using a high-resolution direct numerical simulation. *Phys. Fluids* **14**, 1065–1081.
- GRANT, H. L., STEWART, R. W. & MOILLIET, A. 1962 Turbulence spectra from a tidal channel. *J. Fluid Mech.* **12**, 241–268.
- GYLFASON, A. & WARHAFT, Z. 2004 On higher order passive scalar structure functions in grid turbulence. *Phys. Fluids* **16**, 4012–4019.
- HOLZER, M. & SIGGIA, E. D. 1994 Turbulent mixing of a passive scalar. *Phys. Fluids* **6**, 1820–1837.
- ILIOPOULOS, I. & HANRATTY, T. J. 1999 Turbulent dispersion in a non-homogeneous field. *J. Fluid Mech.* **392**, 45–71.
- JAYESH, TONG, C. & WARHAFT, Z. 1994 On temperature spectra in grid turbulence. *Phys. Fluids* **6**, 306–312.
- KARNIK, U. & TAVOULARIS, S. 1989 Measurements of heat diffusion from a continuous line source in a uniformly sheared turbulent flow. *J. Fluid Mech.* **202**, 233–261.
- KISTLER, A. L. & VREBALOVICH, T. 1966 Grid turbulence at large Reynolds numbers. *J. Fluid Mech.* **26**, 37–47.
- KOLMOGOROV, A. N. 1941*a* Dissipation of energy in the locally isotropic turbulence. *Dokl. Akad. Nauk. SSSR* **32**, 16–18.
- KOLMOGOROV, A. N. 1941*b* The local structure of turbulence in incompressible viscous fluid for very large Reynolds numbers. *Dokl. Akad. Nauk. SSSR* **30**, 301–305.

- KOLMOGOROV, A. N. 1941c On degeneration of isotropic turbulence in an incompressible viscous liquid. *Dokl. Akad. Nauk. SSSR* **31**, 538–540.
- KOLMOGOROV, A. N. 1962 A refinement of previous hypotheses concerning the local structure of turbulence in a viscous incompressible fluid at high Reynolds number. *J. Fluid Mech.* **13**, 82–85.
- KONTOMARIS, K. & HANRATTY, T. J. 1994 Effect of molecular diffusivity on point source diffusion in the center of a numerically simulated turbulent channel flow. *Intl J. Heat Mass Transfer* **37**, 1817 – 1828.
- KORCHASHKIN, N. N. 1970 The effect of fluctuations of energy dissipation and temperature dissipation on locally isotropic turbulent fields. *Izv. Akad. Nauk SSSR, Fiz. Atmos. Okeana* **6**, 947–949.
- KRAICHNAN, R. H. 1994 Anomalous scaling of a randomly advected passive scalar. *Phys. Rev. Lett.* **72**, 1016–1019.
- LANDAU, L. D. & LIFSHITZ, E. M. 1987 *Fluid Mechanics*, 2nd edn. Pergamon Press, Oxford.
- LARUE, J. C., DEATON, T. & GIBSON, C. H. 1975 Measurement of high-frequency turbulent temperature. *Rev. Sci. Instrum.* **46**, 757–764.
- LAUFER, J. 1952 The structure of turbulence in fully developed pipe flow. *Tech. Rep.* 1174. National Advisory Committee for Aeronautics.
- LAVERTU, R. A. 2002 Scalar dispersion in turbulent channel flow. Master’s thesis, McGill University.
- LAVERTU, R. A. & MYDLARSKI, L. 2005 Scalar mixing from a concentrated source in turbulent channel flow. *J. Fluid Mech.* **528**, 135–172.
- LECORDIER, J. C., BROWNE, L. W. B., MASSON, S. LE, DUMOUCHEL, F. & PARANTHON, P. 2000 Control of vortex shedding by thermal effect at low Reynolds numbers. *Exp. Therm. Fluid Sci.* **21**, 227 – 237.
- LEMAY, J. & BENAÏSSA, A. 2001 Improvement of cold-wire response for

- measurement of temperature dissipation. *Exp. Fluids* **31**, 347–356.
- LEPORE, J. & MYDLARSKI, L. 2009 Effect of the scalar injection mechanism on passive scalar structure functions in a turbulent flow. *Phys. Rev. Lett.* **103**, 034501.
- LÉVÊQUE, E., RUIZ-CHAVARRIA, G., BAUDET, C. & CILIBERTO, S. 1999 Scaling laws for the turbulent mixing of a passive scalar in the wake of a cylinder. *Phys. Fluids* **11**, 1869–1879.
- LIENHARD, J. H. & HELLAND, K. N. 1989 An experimental analysis of fluctuating temperature measurements using hot-wires at different overheats. *Exp. Fluids* **7**, 265–270.
- LYONS, S.L., HANRATTY, T.J. & MC-LAUGHLIN, J.B. 1991 Direct numerical simulation of passive heat transfer in a turbulent channel flow. *Intl J. Heat Mass Transfer* **34**, 1149 – 1161.
- MAURER, J., TABELING, P. & ZOCCHI, G. 1994 Statistics of turbulence between two counterrotating disks in low-temperature helium gas. *Europhys. Lett.* **26**, 31–36.
- MCLEOD, M. S. 2000 On the design and testing of a high-aspect-ratio channel for turbulent flow measurements. Master’s thesis, McGill University.
- MENEVEAU, C., SREENIVASAN, K. R., KAILASNATH, P. & FAN, M. S. 1990 Joint multifractal measures: Theory and applications to turbulence. *Phys. Rev. A* **41**, 894–913.
- MONIN, A. S. & YAGLOM, A. M. 1971 *Statistical Fluid Mechanics: Mechanics of Turbulence*. The MIT Press.
- MYDLARSKI, L. 2003 Mixed velocity-passive scalar statistics in high-reynolds-number turbulence. *J. Fluid Mech.* **475**, 173–203.
- MYDLARSKI, L., PUMIR, A., SHRAIMAN, B. I., SIGGIA, E. D. &

- WARHAFT, Z. 1998 Structures and multipoint correlators for turbulent advection: Predictions and experiments. *Phys. Rev. Lett.* **81**, 4373–4376.
- MYDLARSKI, L. & WARHAFT, Z. 1996 On the onset of high-Reynolds-number grid-generated wind tunnel turbulence. *J. Fluid Mech.* **320**, 331–368.
- MYDLARSKI, L. & WARHAFT, Z. 1998 Passive scalar statistics in high-Péclet-number grid turbulence. *J. Fluid Mech.* **358**, 135–175.
- NA, Y. & HANRATTY, T. J. 2000 Limiting behavior of turbulent scalar transport close to a wall. *Intl J. Heat Mass Transfer* **43**, 1749 – 1758.
- NAKAMURA, I., SAKAI, Y., MIYATA, M. & TSUNODA, H. 1986 Diffusion of matter from a continuous point source in uniform mean shear flows (1st report, characteristics of the mean concentration field). *Bull. JSME* **29**, 1141–1148.
- NOVIKOV, E. A. 1994 Infinitely divisible distributions in turbulence. *Phys. Rev. E* **50**, R3303–R3305.
- OBOUKHOV, A. M. 1949 Structure of the temperature field in turbulent flows. *Izv. Akad. Nauk. SSSR, Geogr. Geofiz.* **13**, 58–69.
- OBOUKHOV, A. M. 1962 Some specific features of atmospheric turbulence. *J. Fluid Mech.* **13**, 77–81.
- PAPAVASSILIOU, D. V. & HANRATTY, T. J. 1997 Transport of a passive scalar in a turbulent channel flow. *Intl J. Heat Mass Transfer* **40**, 1303 – 1311.
- PARANTHOËN, P., FOUARI, A., DUPONT, A. & LECORDIER, J. C. 1988 Dispersion measurements in turbulent flows (boundary layer and plane jet). *Intl J. Heat Mass Transfer* **31**, 153–165.
- PASQUILL, F. 1961 The estimation of the dispersion of windborne material. *Meteorol. Mag.* **90**, 33–49.
- POPE, S. B. 2000 *Turbulent Flows*. Cambridge University Press.

- PRASAD, R. R., MENEVEAU, C. & SREENIVASAN, K. R. 1988 Multifractal nature of the dissipation field of passive scalars in fully turbulent flows. *Phys. Rev. Lett.* **61** (1), 74–77.
- RICHARDSON, L. F. 1922 *Weather Prediction by Numerical Process*. Cambridge University Press.
- RUIZ CHAVARRIA, G., BAUDET, C. & CILIBERTO, S. 1995 Extended self-similarity of passive scalars in fully developed turbulence. *Europhys. Lett.* **32**, 319.
- RUIZ-CHAVARRIA, G., BAUDET, C. & CILIBERTO, S. 1996 Scaling laws and dissipation scale of a passive scalar in fully developed turbulence. *Physica D* **99**, 369–380.
- SAKAI, Y., NAKAMURA, I., MIYATA, M. & TSUNODA, H. 1986 Diffusion of matter from a continuous point source in uniform mean shear flows (2nd report, characteristics of concentration fluctuation intensity). *Bull. JSME* **29**, 1149–1155.
- SAWFORD, B. L. & HUNT, J. C. R. 1986 Effects of turbulence structure, molecular diffusion and source size on scalar fluctuations in homogeneous turbulence. *J. Fluid Mech.* **165**, 373–400.
- SCHMITT, F., SCHERTZER, D., LOVEJOY, S. & BRUNET, Y. 1996 Multifractal temperature and flux of temperature variance in fully developed turbulence. *Europhys. Lett.* **34** (3), 195–200.
- SCHUMACHER, J., SREENIVASAN, K. R. & YEUNG, P. K. 2003 Derivative moments in turbulent shear flows. *Phys. Fluids* **15**, 84–90.
- SHE, Z-S. & LEVEQUE, E. 1994 Universal scaling laws in fully developed turbulence. *Phys. Rev. Lett.* **72**, 336–339.
- SHLIEN, D. J. & CORRSIN, S. 1976 Dispersion measurements in a turbulent boundary layer. *Intl J. Heat Mass Transfer* **19**, 285–295.

- SHRAIMAN, B. I. & SIGGIA, E. D. 2000 Scalar turbulence. *Nature* **405**, 639–646.
- SREENIVASAN, K. R. 1991 On local isotropy of passive scalars in turbulent shear flows. *Proc. R. Soc. Lond. A* **434**, 165–182.
- SREENIVASAN, K. R. & ANTONIA, R. A. 1977 Skewness of temperature derivatives in turbulent sheat flows. *Phys. Fluids* **20**, 1986–1988.
- SREENIVASAN, K. R. & ANTONIA, R. A. 1997 The phenomenology of small-scale turbulence. *Annu. Rev. Fluid Mech.* **29**, 435–472.
- SREENIVASAN, K. R., ANTONIA, R. A. & DANH, H. Q. 1977 Temperature dissipation fluctuations in a turbulent boundary-layer. *Phys. Fluids* **20** (8), 1238–1249.
- SREENIVASAN, K. R. & KAILASNATH, P. 1993 An update on the intermittency exponent in turbulence. *Phys. Fluids* **5**, 512–514.
- STAPOUNTZIS, H., SAWFORD, B. L., HUNT, J. C. R. & BRITTER, R. E. 1986 Structure of the temperature field downwind of a line source in grid turbulence. *J. Fluid Mech.* **165**, 401–424.
- STOLOVITZKY, G. & SREENIVASAN, K. R. 1993 Scaling of structure functions. *Phys. Rev. E* **48**, R33–R36.
- TAVOULARIS, S. 2005 *Measurement in Fluid Mechanics*. Cambridge University Press.
- TAYLOR, G. I. 1921 Diffusion by continuous movements. *Proc. Lond. Math. Soc.* **20**, 196–212.
- TAYLOR, G. I. 1935 Statistical theory of turbulence IV - Diffusion in a turbulent air stream. *Proc. R. Soc. Lond. A* **151**, 465–478.
- TAYLOR, G. I. 1953 Dispersion of soluble matter in solvent flowing slowly through a tube. *Proc. R. Soc. Lond. A* **219**, 186–203.
- TAYLOR, G. I. 1954 The dispersion of matter in turbulent flow through a

- pipe. *Proc. R. Soc. Lond. A* **223**, 446–468.
- TENNEKES, H. & LUMLEY, J. L. 1972 *A First Course in Turbulence*. The MIT Press.
- THORODDSEN, S. T. & VAN ATTA, C. W. 1992 Exponential tails and skewness of density-gradient probability density functions in stably stratified turbulence. *J. Fluid Mech.* **244**, 547–566.
- TONG, C. N. & WARHAFT, Z. 1994 On passive scalar derivative statistics in grid turbulence. *Phys. Fluids* **6**, 2165–2176.
- TOWNSEND, A. A. 1954 The diffusion behind a line source in homogeneous turbulence. *Proc. R. Soc. Lond. A* **224**, 487–512.
- UBEROI, M. S. & CORRSIN, S. 1953 Diffusion of heat from a line source in isotropic turbulence. *Tech. Rep.* 1142. National Advisory Committee for Aeronautics.
- VAN ATTA, C. W. 1971 Influence of fluctuations in local dissipation rates on turbulent scalar characteristics in the inertial subrange. *Phys. Fluids* **14**, 1803–1804.
- VAN ATTA, C. W. & CHEN, W. Y. 1970 Structure functions of turbulence in the atmospheric boundary layer over the ocean. *J. Fluid Mech.* **44**, 145–159.
- VAN ATTA, C. W. & PARK, J. 1972 Statistical self-similarity and inertial subrange turbulence. In *Statistical Models and Turbulence* (ed. M. Rosenblatt & C. W. Van Atta), *Lecture Notes in Physics*, vol. 12, pp. 402–426. Springer.
- VILLERMAUX, E., INNOCENTI, C. & DUPLAT, J. 2001 Short circuits in the Corrsin–Obukhov cascade. *Phys. Fluids* **13** (1), 284–289.
- VINCENT, A. & MENEGUZZI, M. 1991 The spatial structure and statistical properties of homogeneous turbulence. *J. Fluid Mech.* **225**, 1–20.
- VISWANATHAN, S. & POPE, S. B. 2008 Turbulent dispersion from line sources

- in grid turbulence. *Phys. Fluids* **20**, 101514.
- VRIELING, A. J. & NIEUWSTADT, F. T. M. 2003 Turbulent dispersion from nearby point sources—interference of the concentration statistics. *Atmos. Environ.* **37**, 4493–4506.
- WARHAFT, Z. 1984 The interference of thermal fields from line sources in grid turbulence. *J. Fluid Mech.* **144**, 363–387.
- WARHAFT, Z. 2000 Passive scalars in turbulent flows. *Annu. Rev. Fluid Mech.* **32**, 203–240.
- WARHAFT, Z. & GYLFASSON, A. 2004 Passive scalar fine scale structure: recent results and implications for the velocity field. In *Advances in Turbulence X* (ed. H. I. Andersson & P-A. Krogstad), pp. 801–1–801–7. CIMNE.
- WARHAFT, Z. & LUMLEY, J. L. 1978 An experimental study of the decay of temperature fluctuations in grid-generated turbulence. *J. Fluid Mech.* **88**, 659–684.
- WATANABE, T. & GOTOH, T. 2006 Intermittency in passive scalar turbulence under the uniform mean scalar gradient. *Phys. Fluids* **18**, 058105.
- WYNGAARD, J. C. 1969 Spatial resolution of vorticity meter and other hot-wire arrays. *J. Sci. Instrum.* **2**, 983–987.
- WYNGAARD, J. C. 1971 Spatial resolution of a resistance wire temperature sensor. *Phys. Fluids* **14**, 2052–2054.
- XU, G, ANTONIA, R. A. & RAJAGOPALAN, S 2000 Scaling of mixed longitudinal velocity-temperature structure functions. *Europhys. Lett.* **49** (4), 452–458.
- YAGLOM, A. M. 1949 On the local structure of a temperature field in a turbulent flow. *Dokl. Akad. Nauk. SSSR* **69**, 743–746.
- ZUKAUSKAS, A. 1972 Heat transfer from tubes in crossflow. In *Advances in Heat Transfer* (ed. J. P. Hartnett & T. F. Irvine Jr.), *Advances in Heat*

Transfer, vol. 8, pp. 93 – 160. Elsevier.